DOCTORAL THESIS

# Molecular Modeling at High X-ray Intensity: Developments, Applications and Challenges

*Dissertation zur Erlangung des Doktorgrades*
*des Fachbereiches Chemie*
*der Universität Hamburg*

vorgelegt von

**Julia M. Schäfer**

aus

Marbach am Neckar

Hamburg

2021

**Gutachter der Dissertation:**

Prof. Dr. Robin Santra

Prof. Dr. Gabriel Bester

**Gutachter der Disputation:**

Prof. Dr. Robin Santra

Prof. Dr. Gabriel Bester

Prof. Dr. Carmen Herrmann

Prof. Dr. Till Jahnke

Dr. Holger Lange

**Datum der Disputation:**

17.12.2021

*“The enchanting charms of this sublime science reveal only to those who have the courage to go deeply into it.”*

Carl Friedrich Gauss

# Zusammenfassung

Röntgen-Freie-Elektronen-Laser (XFELs) stellen hochintensive und ultrakurze Femtosekunden-Röntgenpulse bereit. Mit dem Aufkommen solcher Großforschungsanlagen während der letzten Dekade bieten sich z.B. vollkommen neuartige Möglichkeiten für die Untersuchung der Struktur von Molekülen. Inzwischen etablierte Methoden beruhen meist auf der Messung von Beugungsmustern nach der Bestrahlung einer kristallinen Probe mit Röntgenstrahlen. Für diese Ansätze ist es essentiell, dass Strahlungsschäden sowohl an den Elektronen als auch an den Atomkernen des untersuchten Moleküls vermieden werden, um die höchstmögliche Auflösung zu erreichen. Meine Ergebnisse aus *Ab-initio*-Rechnungen lassen erkennen, dass der induzierte elektronische Strahlungsschaden bei weichen XFEL-Pulsen sich deutlich von jenem bei harten XFEL-Pulsen unterscheidet. XFEL-Pulse können allerdings auch dazu verwendet werden, die atomaren Bausteine der Moleküle selbst abzubilden. Dabei werden die Impulse der atomaren Ionen nach der Coulombexplosion gemessen, welche durch den XFEL-Puls ausgelöst wurde. Diese Coulomb Explosion Imaging (CEI) genannte Messmethode steckt allerdings noch in den Anfängen und eine der Haupthürden, welche in Zukunft noch zu nehmen sind, ist die Inversion der gemessenen Impulsraumdaten in den Ortsraum. Die Resultate meiner Rechnungen, in welchen ich einen hybriden quantenmechanisch-klassischen Ansatz benutzt habe, sind in guter Übereinstimmung mit kürzlich erhaltenen experimentellen Ergebnissen. Dies macht den verwendeten Code auf lange Sicht vielversprechend für die oben genannte Strukturinversion von XFEL-induzierten Coulombexplosionsdaten. Im letzten Teil dieser Doktorarbeit leite ich ein Ladungstransferschema her, welches auf quantenmechanischen Prinzipien basiert. Dieses Modell füllt eine Lücke, da in anderen Modellen die Zeitabhängigkeit des Elektronentransfers häufig nicht auf mikroskopischer Ebene modelliert ist.

# Abstract

The advent of X-ray free-electron lasers (XFELs) over the past decade, providing ultraintense femtosecond X-ray pulses, offers novel opportunities for molecular structure investigations. By now, most of the established approaches revolve around diffractive imaging schemes with crystalline samples, where electronic and nuclear radiation damage, caused by the X-rays, must be avoided to achieve the highest possible spatial resolution. My results from *ab initio* calculations reveal that the induced electronic radiation damage is fundamentally different for soft as compared to hard XFEL pulses. XFEL pulses, however, can also be used to image the atomic building blocks of molecules themselves, by measuring the momenta of atomic ions after the Coulomb explosion triggered by the XFEL pulse. This method called Coulomb Explosion Imaging (CEI) is still in a premature state and a main challenge that remains nowadays, is the inversion of the measured momentum space information into position space. My calculations employing a hybrid quantum-classical approach are in good agreement with recently obtained experimental results, which renders the used toolkit in the long term promising for structural inversions of XFEL-induced Coulomb explosion imaging data. In the last part of this Ph.D. thesis, I derive a charge transfer scheme which is based on quantum mechanical principles. This framework fills a gap, as in other models the time-dependence of electron transfer is often not modeled on a microscopic level.

# List of Publications

1. "Electron and fluorescence spectra of a water molecule irradiated by an x-ray free-electron laser pulse",

   J. M. Schäfer, L. Inhester, S.-K. Son, R. F. Fink, and R. Santra *Physical Review A* **2018**, *97(5)*, 053415.

   I performed the calculations, analyzed them and wrote the manuscript together with L. Inhester and the other authors.

2. "X-ray multiphoton-induced Coulomb explosion images complex single molecules",

   R. Boll*, J. M. Schäfer*, B. Richard, K. Fehre, G. Kastirke, Z. Jurek, M. S. Schöffler, M. M. Abdullah, N. Anders, T. M. Baumann, S. Eckart, B. Erk, A. De Fanis, R. Dörner, S. Grundmann, P. Grychtol, A. Hartung, M. Hofmann, M. Ilchen, L. Inhester, C. Janke, R. Jin., M. Kircher, K. Kubicek, M. Kunitski, X. Li, T. Mazza, S. Meister, N. Melzer, J. Montano, V. Music, G. Nalin, Y. Ovcharenko, C. Passow, A. Pier, N. Rennhack, J. Rist, D. E. Rivas, D. Rolles, I. Schlichting, L. Ph. H. Schmidt, P. Schmidt, J. Siebert, N. Strenger, D. Trabert, F. Trinter, I. Vela-Perez, R. Wagner, P. Walter, M. Weller, P. Ziolkowski, S.-K. Son, A. Rudenko, M. Meyer, R. Santra, T. Jahnke *Nature Physics* **2022**, *18(4)*, DOI 10.1038/s41567-022-01507-0.

   * These authors contributed equally to this work

   I carried out the calculations, analyzed them and wrote the manuscript together with R. Boll, R. Santra and T. Jahnke, and with input from all authors.

3. "Statistical analysis of correlations in the x-ray induced Coulomb explosion of iodopyridine",

   B. Richard, J. M. Schäfer, Z. Jurek, R. Santra, L. Inhester *Journal of Physics B: Atomic, Molecular and Optical Physics* **2021**, *54(19)*, 194001.

   I provided the simulated Coulomb explosion data and contributed to the manuscript.

# List of Abbreviations

| | |
|---|---|
| **2D** | two-dimensional |
| **3D** | three-dimensional |
| **CEI** | Coulomb explosion imaging |
| **COLTRIMS** | cold target recoil ion momentum spectroscopy |
| **CREXIM** | charge-rearrangement-enhanced X-ray ionization of molecules |
| **DFT** | density functional theory |
| **FWHM** | full-width at half-maximum |
| **HF** | Hartree-Fock |
| **HFS** | Hartree-Fock-Slater |
| **IAM** | independent-atom model |
| **LCAO** | linear combination of atomic orbitals |
| **LCLS** | Linac Coherent Light Source |
| **LDA** | local density approximation |
| **MD** | molecular dynamics |
| **MOM** | maximum overlap method |
| **RHF** | restricted Hartree-Fock |
| **SASE** | self-amplification of spontaneous emission |
| **SCF** | self-consistent field |
| **SFX** | serial femtosecond crystallography |
| **SQS** | Small Quantum Systems |
| **XFEL** | X-ray free-electron laser |
| **XFELs** | X-ray free-electron lasers |

# List of Figures

# List of Tables

# Contents

# Chapter 1

# Introduction

X-ray free-electron lasers (XFELs) [1, 2] are novel X-ray radiation sources that offer ultrashort pulses in the femtosecond ($10^{-15}$ s) and subfemtosecond timescale with unprecedentedly high brilliances. [3–6] In 2009, the first hard X-ray FEL, the Linac Coherent Light Source (LCLS) in the USA, started operation. [7] Today, further hard XFELs in Japan (SACLA [8]), Korea (PAL-XFEL [9]), Switzerland (SwissFEL [10]) and Germany (European XFEL [11]) provide access to XFEL experiments for a growing number of scientists. Soft XFELs are presently located in Italy (FERMI [12]), Germany (FLASH [13]) and China (SXFEL [14]).

An important application of XFEL pulses lies in the field of X-ray crystallography, i.e., in resolving the atomic arrangement in crystals via X-ray diffraction. While X-ray crystallography is at present the primary technique for structure determination of proteins, there exist also many biological systems such as membrane proteins, from which it is difficult to obtain large, well-diffracting crystals. [15–17] Aside from crystal quality and crystal size, X-ray crystallography is also challenged by radiation damage. [15] X-rays damage the sample because, e.g., at a wavelength of 1 Å , the photoelectric cross section of carbon is about 10 times higher than its elastic-scattering cross section. [18] Thus, diffraction experiments using the highly intense pulses provided by XFELs are inevitably accompanied by high degrees of ionization. The high charges created via X-ray multiphoton ionization lead to electrostatic repulsion of the charged nuclei and ultimately to Coulomb explosion of the molecules. Since X-rays are scattered by the electron density, both the electronic damage and the distortion of atomic positions limit the resolution of diffraction experiments at XFELs. Nonetheless, already in the year 2000, Neutze *et al.* [18] predicted that pulses from XFELs could be realized sufficiently short and intense that the structural information can be retrieved with tolerable radiation damage. The background is that there is an inertial delay in the conversion of potential energy into kinetic energy, thus retarding the Coulomb explosion of the nuclei. Consequently, for sub-10-fs pulses the nuclei predominantly move when the pulse is already over. This principle of "diffraction before destruction" [18] is applied in the recently introduced method of serial femtosecond crystallography (SFX), which uses XFEL pulses. [17] The technique opens up new opportunities for structure determination of difficult-to-crystallize molecules, as the examined crystals can be smaller than in conventional X-ray crystallography. [15, 18]

For example, SFX has been successfully applied in resolving the structures of lysozyme from microcrystals [15], and of photosystem I from nanocrystals [17]. One of the main obstacles on the road to structure determination of smaller crystals, and eventually single molecules with SFX, remains radiation damage, as it is still not well understood.
In this Ph.D. thesis I investigate computationally the electronic radiation damage induced in different regioisomers of iodopyridine by intense soft X-ray FEL pulses. The interest in iodine-containing compounds arises from methods introducing heavy atoms such as iodine in molecules to solve the phase problem in X-ray crystallography. [19, 20] It has recently been found that on and in the vicinity of these heavy atoms extremely strong electronic radiation damage is induced. [21] More precisely, the joint computational and experimental study in the hard X-ray regime has revealed that iodomethane $CH_3I$ reaches at ultrahigh X-ray intensities significantly higher charge states compared to what is found for the sum of independent iodine, carbon and hydrogen atoms. This constitutes a paradigm shift because previously it had been thought the charge of atoms in polyatomic molecules can be deduced from the charge of an isolated atom under the same irradiation conditions. [21]

The molecular ionization enhancement occurs due to ultrafast molecular electron rearrangement towards the iodine atom, making more electrons available for ionization on the iodine atom, which has a much higher photoionization cross section than the methyl group. This effect has been called charge-rearrangement-enhanced X-ray ionization of molecules (CREXIM) and is crucial for our understanding of experiments at XFELs. A computational study on the ionization of iodobenzene by intense femtosecond pulses in the hard X-ray regime has shown that the carbon atoms at the far end from the iodine site end up more highly charged than the ones closer to iodine. [22] In order to verify this trend, an experiment was designed where, at different positions in the aromatic ring of iodobenzene, a carbon atom is replaced by a nitrogen atom. The nitrogen is thus intended to serve as a marker atom for the charge transfer.
In *Chapter 3* I present corresponding computational investigations on the regioisomers 2-, 3- and 4-iodopyridine. The calculations were performed using the X-ray molecular physics toolkit XMOLECULE [23] and the X-ray atomic physics toolkit XATOM [24], which are described in detail in *Chapter 2*.
At high X-ray intensities atoms and molecules typically become highly ionized. In order to optimize the electronic structure for every emerging multiple-hole configuration, the toolkits thus employ the computationally cheap Hartree-Fock-Slater electronic structure model [25], and the molecular calculations are performed with fixed geometry. My results in *Chapter 3* extend the investigations of radiation damage towards the soft X-ray regime as well as my previous work [26], in which I investigated how the X-ray ionization dynamics manifests itself in electron and fluorescence spectra of a single water molecule, likewise employing XMOLECULE. The remaining CREXIM studies using XMOLECULE were conducted in the hard X-ray regime, at 8.3 keV [21, 22] and 12 keV [27], because for higher photon energies the ratio of elastic-scattering events to damaging events becomes more favorable [18, 28, 29]

for diffractive imaging experiments such as SFX. Besides, atomic resolution requires photon energies of 12 keV and higher (12 keV $\hat{=}$ 1 Å wavelength). SFX also works for longer wavelengths, just with lower resolution that is diffraction-limited. [30] In an SFX experiment at 2 keV, which is a photon energy I used in my calculations, a resolution of 8 Å could thus be achieved. [31] Previous experiments with intense soft X-rays [32–35] suggest that the charge of atoms in a polyatomic molecule can be inferred from the charge induced in an isolated atom. In contrast, my XMOLECULE results predict a molecular ionization enhancement also in the soft X-ray regime.

A different approach to structural investigations with XFELs, complementary to SFX, is to analyze the asymptotic momenta of the fragments after the Coulomb explosion. Consequently, in this method termed Coulomb explosion imaging (CEI), the nuclear radiation damage is not unwelcome. On the contrary, it underlies the working principle of the approach and is required to analyze the structure of single gas-phase molecules. As is the case with other methods for structure determination, in most cases theory is required for converting the measured signal, here the asymptotic momenta, into the initial atomic positions prior to the explosion. Such a geometry reconstruction is challenging, and most CEI research articles do not perform an actual geometry reconstruction, but instead extract information from the momentum vectors themselves. [36] The few cases, in which CEI could be used to determine molecular structures with a certain degree of accuracy, concern not more than triatomic molecules [37] ($H_3^+$ [38], Efimov state of the $^4$He trimer [39], $D_2O$ and $SO_2$ [40]). Key to the success of CEI is a fast charge-up of all atoms, such that the molecule fragments completely into atomic ions without structural rearrangements or formation of long-lived intermediate molecular fragment ions, which would complicate the mapping from asymptotic fragment momenta to the initial atomic positions. [41] Reaching high degrees of ionization is crucial to obtain a strong Coulomb repulsion that overcomes any chemical binding energies. High charge states are particularly important if the goal is a geometry reconstruction, as CEI simulations typically employ a simple model, in which Coulomb repulsion is the only force incorporated, disregarding chemical bonding forces. [41–45]

In the beginnings of CEI [38, 46], the rapid charge-up was realized by sending molecular ion beams from a storage ring through a thin metal foil. Thus, valence electrons are stripped off on a subfemtosecond timescale, and the explosion evolves quasi-instantaneously. Also collisions with highly charged ions have been used to trigger the explosion. [47–49] In more recent approaches, the Coulomb explosion is often induced by intense femtosecond laser pulses, paving the way for time-resolved pump-probe experiments to image photo-induced structural dynamics. [50] This method creates the charges via multiphoton ionization or strong-field ionization, or a combination of the two [51]. As a tabletop solution, it requires less effort than the approach employing stripping foils, and especially neutral molecules can easily be examined, whereas in foil-induced CEI sophisticated experimental setups are

required to study neutral molecules. [37, 46] Laser-induced Coulomb explosion has been applied to study the structure of molecules consisting of five atoms. [37, 52] For example, the absolute configuration of the prototypical chiral molecule bromochlorofluoromethane (CHBrClF) could be determined without exact geometric reconstruction, confirmed by molecular dynamics simulations. [52] Laser-induced CEI is limited by the currently available laser intensities, which make it difficult to reach very high molecular charge states. [52, 53]
The Coulomb explosion can also be induced by inner-shell absorption of one or multiple X-ray photons and subsequent Auger decays. For example, ionization with a single X-ray photon from a synchrotron light source was used to determine the absolute configuration of a chiral molecule. [53] Also the ultraintense pulses from XFELs are considered promising for CEI, as they charge systems highly on femtosecond timescales via X-ray multiphoton ionization. [54, 55] In fact, the feasibility of XFEL-induced CEI has been proven in an experiment on the planar 12-atom molecule 5-iodouracil ($C_4H_3IN_2O_2$) at the SACLA XFEL facility [8] in Japan. [45, 56]

In *Chapter 4* of this thesis I report on a joint experimental and theoretical XFEL-CEI study on the planar molecules 2-iodopyridine ($C_5H_4IN$) and iodopyrazine ($C_4H_3IN_2$). The experiment was conducted employing a cold target recoil ion momentum spectroscopy (COLTRIMS) reaction microscope [57], which is part of the Small Quantum Systems (SQS) scientific instrument at the European XFEL [11]. The results of our collaboration demonstrate that soft XFEL pulses facilitate imaging complex ring molecules completely as atomic ions. In comparison with the study at SACLA [45, 56], the higher repetition rate of the European XFEL [11] led to higher-quality, i.e., clearer, momentum images as well as to the detection of higher-order coincidences with sufficient statistics (up to eight-fold coincidences vs. triple coincidences). Moreover, we were able to obtain detailed information on the ultrafast intramolecular electron rearrangement from the ring atoms towards the iodine. In order to simulate the XFEL-induced CEI, I employed the XMDYN [58] theoretical toolkit which combines atomic *ab initio* X-ray physics with molecular dynamics. It includes charge transfer between atom pairs based on a classical over-the-barrier model [59–61], and Coulomb forces between charged particles are the only acting forces. My results are in good agreement with experiment, thus allowing me to supplement the study with insight into the ionization dynamics as well as into the geometry evolution of the fragments. I also discuss in *Chapter 4* which improvements to the model were necessary to obtain the presented results, and which further steps are required on the route towards geometric reconstructions of complex molecules using XFEL-CEI data.

Both toolkits I applied, XMDYN and XMOLECULE, lack a continuous modeling of intramolecular electron transfer on a microscopic level. In other models, the details of electron transfer dynamics are often only taken into account via fitting procedures. [45, 56] Hence, in *Chapter 5* I develop an alternative scheme for electron transfer in the XMDYN framework, based on quantum mechanics, that provides information on the time-dependence of electron transfer. A minimal model is employed, in which molecular orbitals are constructed by linear combinations of two atomic orbitals located on two different atoms. The expansion coefficients obtained for the molecular orbitals are then used to construct and propagate a wave packet to thus describe charge transfer dynamics between the atomic orbitals.

*Chapter 6* comprises the conclusions of the work presented in this thesis as well as an outlook on future work.

# Chapter 2

# Computational Methods

The simulation results presented in this Ph.D. thesis were generated with a computational toolbox developed in the CFEL-DESY Theory Division to model high-intensity X-ray induced dynamics of matter. In this chapter, first the common features of the three toolkits are presented. Next, the individual simulation tools are introduced, starting with the X-ray atomic physics toolkit XATOM [24], because the X-ray molecular physics toolkit XMOLECULE [23] as well as the X-ray molecular dynamics toolkit XMDYN [58] utilize atomic data computed by XATOM.

## 2.1 Common features of XATOM, XMOLECULE and XMDYN

### 2.1.1 Electronic structure model

The three packages have in common that they are designed to be computationally efficient. This feature is a prerequisite in the simulation of high-intensity X-ray studies because – with a photon energy chosen above all ionization edges – in the course of the multiple ionization dynamics any electronic configuration from the neutral to the fully ionized system may emerge. In order to optimize the electronic structure for each occurring multiple-hole configuration the toolkits are based on the Hartree-Fock-Slater (HFS) model[1] [25]. This approach represents a simplification of the Hartree-Fock (HF) method to reduce the computational complexity [62, 63] by introducing a local density approximation to the otherwise nonlocal and exact exchange potential in HF theory. Within this approximation exchange interaction is modeled by the potential

$$V_x(\vec{r}) = -\alpha \frac{3}{2} \left[ \frac{3}{\pi} \rho(\vec{r}) \right]^{\frac{1}{3}} . \tag{2.1}$$

Here, $\rho(\vec{r})$ denotes the electron density and $\alpha$ is called Slater's exchange parameter. In the toolkits used in this work, and initially by Slater [62], $\alpha$ is set to one. The exchange potential for $\alpha = 1$ originates from the description of a free-electron gas in a solid. [25] In the local density approximation (LDA)

---

[1] XATOM and XMOLECULE directly, XMDYN via XATOM.

of density functional theory (DFT) correlation and exchange are, in practice, calculated separately. [64] The latter is computed with Eq. (2.1), where $\alpha$ is set to $\frac{2}{3}$. [65] Later it was suggested to introduce the parameter $\alpha$ as an adjustable parameter that is to be determined separately for every material, in the so-called X$\alpha$ approximation. [62, 65, 66] Interestingly, the X$\alpha$ method describes the dissociation of the $H_2$ molecule into neutral H atoms correctly [67] (unlike restricted Hartree-Fock (RHF) theory, which predicts 50% ionic $H^+$+$H^-$), and as a rule HFS bond energies are better than HF bond energies. [68] However, in the vast majority of cases HF and HFS results are fairly similar. [63]

### 2.1.2 Electronic structure of the ground state and of excited states

XATOM solves the atomic Hartree-Fock-Slater equations,

$$\hat{f}(i)\phi_a(i) = \epsilon_a\phi_a(i)\,, \tag{2.2}$$

in a self-consistent field (SCF) procedure. The operator $\hat{f}(i)$ is the effective single-particle Fock operator which contains the Slater exchange potential $V_x(\vec{r})$ given in Eq. (2.1). The single-particle wavefunction $\phi_a(i)$ represents the atomic spin-orbital with index $a$, occupied with electron $i$. Within the XATOM framework, Equation (2.2) is solved numerically on a grid [24] for a specific atomic electronic configuration.

In the construction of molecular orbitals $\psi_a(\vec{r})$ the X-ray molecular physics toolkit XMOLECULE employs the linear combination of atomic orbitals (LCAO) approach [23]

$$\psi_a(\vec{r}) = \sum_\mu C_{\mu a}\phi_\mu(\vec{r})\,, \tag{2.3}$$

where $\phi_\mu(\vec{r})$ denotes the $\mu$th atomic orbital, and $C_{\mu a}$ is the coefficient of the $\mu$th atomic orbital for the $a$th molecular orbital. Since atomic orbitals at different atomic sites may overlap, the basis is non-orthogonal. Therefore, XMOLECULE's SCF algorithms aim at finding an HFS solution for the Roothaan-Hall equation [69],

$$\underline{\underline{F}}\left[\underline{\underline{C}}^{\mathrm{old}}\right]\underline{\underline{C}}^{\mathrm{new}} = \underline{\underline{S}}\,\underline{\underline{C}}^{\mathrm{new}}\underline{\underline{\epsilon}}^{\mathrm{new}}\,, \tag{2.4}$$

with $\underline{\underline{F}}$ being the Fock matrix. The notation $\underline{\underline{F}}\left[\underline{\underline{C}}^{\mathrm{old}}\right]$ makes clear that the Fock matrix is built from the current molecular orbital coefficient matrix $\underline{\underline{C}}^{\mathrm{old}}$. The matrix $\underline{\underline{S}}$ is the overlap matrix of the non-orthogonal basis functions. Equation (2.4) is then solved to yield a new molecular orbital coefficient matrix $\underline{\underline{C}}^{\mathrm{new}}$ and a new matrix of orbital energies $\underline{\underline{\epsilon}}^{\mathrm{new}}$. [70] Since the Fock matrix depends on the LCAO coefficients, the Roothaan-Hall equation is solved iteratively until the orbitals become self-consistent at convergence. When this point is reached, the Fock operator built from the orbitals gives the same orbitals as eigenfunctions. In this way the Hartree-Fock variational principle usually yields the best and lowest-energy single Slater determinant approximation of a ground state wavefunction for a given basis set. [70, 71] For obtaining the HFS solution for the **electronic ground state** XATOM and XMOLECULE occupy the energetically lowest orbitals in every SCF iteration, following the aufbau principle. [23, 70]

For computing an approximation of the ground-state electronic structure of atoms and molecules [70, 72], HF theory as well as DFT are well-established methods, and HFS occupies as ancestor of modern DFT [68] the place between them.

The SCF algorithms used in XATOM and XMOLECULE do not directly minimize the HFS energy functional, but use the more efficient way [72] of solving the HFS equations. These procedures are closely related because finding orbitals, which are eigenfunctions of the Fock operator, corresponds to finding a stationary point on the energy hypersurface. [73] This means that one can use XATOM and XMOLECULE not only to find the global minimum of the HFS energy functional (the electronic ground state), but also to find other stationary points on the energy hypersurface that are genuine higher-energy solutions of the SCF problem and can be used to model the electronic structure of **excited states**. [70] In practice, XMOLECULE employs a variant of the maximum overlap method (MOM) [23, 70] to guide the SCF procedure towards such an excited-state solution: In order to obtain the electronic structure consisting of $(n-1)$ electrons after an ionization event, as initial guess the orbitals optimized for the "parent" configuration with $n$ electrons are occupied with the new set of occupation numbers. Subsequently, in every SCF iteration the orbitals are not occupied according to their energy following the aufbau principle as for the ground-state solution, but such as to maximize the overlap between the occupied orbitals in the previous and in the current iteration. [23, 70] This strategy impedes variational collapse to the ground-state solution. [70]

In summary, the presented approach allows finding higher-energy solutions of the SCF equations with orbitals relaxed for the respective excited state at the low computational cost of the HFS electronic structure model. Its practicability strongly relies on starting with a good initial guess in the proximity of the targeted excited-state solution. [70] A combination of HF theory with the MOM for locating higher solutions of the SCF equations yielded surprisingly accurate results for (however, low-lying) excited states of $H_2$. [74]

### 2.1.3 Transition energies

Transition energies for photoionization processes are calculated using Koopmans' theorem [75]. This means that the ionization potential $I_k$ for removing an electron from the $k$th spin orbital is approximated as the negative of the corresponding orbital energy $\epsilon_k$ of the neutral system (that still contains the electron which is later removed)

$$I_k \approx -\epsilon_k\,. \tag{2.5}$$

For canonical Hartree-Fock orbitals the approximation in Eq. (2.5) is exact through first order. [76] Since the underlying derivation is often presented in abbreviated form, it will be given in long form here, following Ref. [77].

In the HF formalism the total ground-state energy of an $n$ electron system ${}^{n}E_0$ is given as

$${}^{n}E_0 = \sum_{i=1}^{n} h_{ii} + \frac{1}{2}\sum_{i=1}^{n}\sum_{j=1}^{n}\left(J_{ij} - K_{ij}\right)\,, \tag{2.6}$$

where the terms $h_{ii}$ are one-electron integrals with the one-electron Hamiltonian $\hat{h}_1$ and the $\psi_i$ describing the $n$ different occupied spin orbitals ($i = 1, ..., n$). In atomic units, they are defined as

$$h_{ii} = \langle i|\hat{h}_1|i\rangle = \int \psi_i^*(\overrightarrow{x_1})\left[-\frac{1}{2}\nabla^2 - \sum_k \frac{Z_k}{r_{ik}}\right]\psi_i(\overrightarrow{x_1})d\overrightarrow{x_1}\,. \tag{2.7}$$

Here, the first operator in square brackets describes the kinetic energy of the electron in the $i$th spin orbital, while the second term is the sum of the Coulomb attraction between this electron and all nuclei with running index $k$, with $Z_k$ being the associated atomic number and $r_{ik}$ the distance between the electron and the nucleus.

The $J_{ij}$ and $K_{ij}$ are two-electron integrals with the part of the Hamiltonian describing the interaction between the electrons in the spin orbitals $i$ and $j$. The $J_{ij}$ are called the Coulomb integrals and the $K_{ij}$ are called the exchange integrals. Using physicists' notation [78], they are defined as

$$J_{ij} = \langle ij|ij\rangle = \int\int \psi_i^*(\overrightarrow{x_1})\psi_j^*(\overrightarrow{x_2})\frac{1}{|\overrightarrow{r_{12}}|}\psi_i(\overrightarrow{x_1})\psi_j(\overrightarrow{x_2})d\overrightarrow{x_1}d\overrightarrow{x_2} \tag{2.8}$$

$$K_{ij} = \langle ij|ji\rangle = \int\int \psi_i^*(\overrightarrow{x_1})\psi_j^*(\overrightarrow{x_2})\frac{1}{|\overrightarrow{r_{12}}|}\psi_j(\overrightarrow{x_1})\psi_i(\overrightarrow{x_2})d\overrightarrow{x_1}d\overrightarrow{x_2} \tag{2.9}$$

The coordinates $\vec{x}$ in Eqs. (2.7)-(2.9) include both the spatial and spin coordinates of the one or two electrons.

The HF energy of the $k$th spin orbital is given as

$$\epsilon_k = \langle k|\hat{f}|k\rangle = h_{kk} + \sum_{j=1}^{n}\left(J_{kj} - K_{kj}\right)\,. \tag{2.10}$$

Now we consider removing an electron from orbital $k$ to create an $(n-1)$ electron system, corresponding to the remaining electronic structure after a photoionization. If we assume that the removal of this electron from orbital $k$ does not alter the other spin orbitals, the total energy of the $(n-1)$ electron system ${}^{n-1}E_k$ reads as

$$ {}^{n-1}E_k = \sum_{\substack{i=1\\i\neq k}}^{n} h_{ii} + \frac{1}{2}\sum_{\substack{i=1\\i\neq k}}^{n}\sum_{\substack{j=1\\j\neq k}}^{n}\left(J_{ij} - K_{ij}\right) \,. \tag{2.11}$$

For the ionization potential $I_k$ that is necessary to remove an electron from the $k$th spin orbital we obtain the following, inserting Eqs. (2.11) and (2.6),

$$\begin{aligned} I_k = {}^{n-1}E_k - {}^{n}E_0 &= \sum_{\substack{i=1\\i\neq k}}^{n} h_{ii} + \frac{1}{2}\sum_{\substack{i=1\\i\neq k}}^{n}\sum_{\substack{j=1\\j\neq k}}^{n}\left(J_{ij} - K_{ij}\right) - \left[\sum_{i=1}^{n} h_{ii} + \frac{1}{2}\sum_{i=1}^{n}\sum_{j=1}^{n}\left(J_{ij} - K_{ij}\right)\right] \\ &= -h_{kk} - \frac{1}{2}\sum_{i=1}^{n}\left(J_{ik} - K_{ik}\right) - \frac{1}{2}\sum_{j=1}^{n}\left(J_{kj} - K_{kj}\right) \,. \end{aligned} \tag{2.12}$$

Since the sums in the last expression exhibit the same limits, we can simplify

$$ I_k = -h_{kk} - \frac{1}{2}\sum_{j=1}^{n}\left(J_{jk} - K_{jk}\right) - \frac{1}{2}\sum_{j=1}^{n}\left(J_{kj} - K_{kj}\right) \,. \tag{2.13}$$

Now we need to recall the symmetry properties of the two-electron integrals

$$ J_{jk} = \langle jk|jk\rangle = \langle kj|kj\rangle = J_{kj} \tag{2.14}$$

$$ K_{jk} = \langle jk|kj\rangle = \langle kj|jk\rangle = K_{kj} \tag{2.15}$$

in order to arrive at the negative of the energy of the $k$th spin orbital (Eq. (2.10)) and thus, Koopmans' theorem (Eq. (2.5))

$$ I_k = -h_{kk} - \sum_{j=1}^{n}\left(J_{kj} - K_{kj}\right) = -\epsilon_k \,. \tag{2.16}$$

As demonstrated, Koopmans' theorem can be derived in the formalism of (restricted) Hartree-Fock theory, assuming in Eq. (2.11) that the other spin orbitals are not altered by the removal of the electron from orbital $k$, i.e., in the *frozen orbital* approximation. In reality, however, the orbitals contract due to the reduced shielding of the nuclear charge. Consequently, the neglect of this orbital relaxation constitutes one main source of error when applying Koopmans' theorem in the HF method.

In addition to this, although the HF variational principle does yield the best single Slater determinant approximation of a ground-state wavefunction [71] for a given basis set (as mentioned earlier), even in the limit of a complete basis set the HF energy $E_{\text{HF limit}}$ is always above the exact energy $E_{\text{exact}}$,

$$ E_{\text{HF limit}} > E_{\text{exact}} \,. \tag{2.17}$$

The reason is that HF theory disregards that electron motion is correlated, i.e., electrons move to avoid each other. Thus, the second main source of error in Eq. (2.5) is the correlation energy $E_{\mathrm{corr}}$ which is always negative,

$$E_{\mathrm{corr}} = E_{\mathrm{exact}} - E_{\mathrm{HF\ limit}} \,. \tag{2.18}$$

In practice one observes a partial cancellation of correlation and relaxation errors, and thus Koopmans' theorem provides reasonable ionization potentials at low computational cost. [79, 80]

In the HFS model employed in this Ph.D. thesis Koopmans' theorem is not fulfilled. [81] However, it is approximately valid [24], and $K$-shell binding energies of noble-gas atoms, calculated with a nonrelativistic HFS-based Herman-Skillman code [82], applying Koopmans' theorem, agree to experimental values from the X-ray Data Booklet [83] within a few per cent. [76] The remaining discrepancies can be traced back to relativistic electronic structure effects and correlation energies. [76]

By analogy with Koopmans' theorem, transition energies for Auger and fluorescence decays are also calculated based on the energy differences of the involved orbitals of the initial system with the core hole. This approach is computationally efficient, as the transition energies are required for calculating transition rates and cross sections. In this way only the electronic structure of the initial state needs to be optimized, and not the electronic structures of all possible final states. Only Chapter 4 deviates slightly from this approach, as kinetic energies of Auger electrons are derived differently from HFS-provided quantities there (see Section 4.4).

### 2.1.4 Simulation of the X-ray matter interaction

The three toolkits used in this Ph.D. work have in common that the interaction between the intense X-ray pulse and the atomic or molecular system is modeled with sequential one-photon ionization steps. Although the unprecedentedly high brilliance of XFELs facilitated first observations of direct (i.e., nonsequential) two-photon processes [84, 85], this approach is justified because the single-photon cross section typically dominates over the direct multiphoton cross section. Consequently, multiphoton absorption in the X-ray regime predominantly takes place as sequential single-photon absorption. [54]

In the simulation every inner-shell photoionization is followed by the associated relaxation of the hole: Auger or fluorescence decay. For atoms with low atomic number $Z$ the Auger decay rate of an inner-shell hole generally exceeds the X-ray fluorescence rate by far. Only for elements heavier than zinc ($Z > 30$) a $K$-shell hole decays preferentially, in a first step, through X-ray fluorescence. [86] In the interaction with an intense X-ray pulse, typically many different electronic configurations play a role, due to consecutive or overlapping cycles of photoionization, Auger and fluorescence events. Our computationally cheap electronic structure model (see Section 2.1.1) allows for the reoptimization of the electronic structure for every multiple-hole electronic configuration which is formed in the course of the X-ray ionization dynamics. Every such electronic configuration $I$ is characterized by the occupation numbers of the atomic or molecular orbitals. On a side note, we disregard electron spin, and degenerate orbitals are occupied with average occupation, therefore also fractional occupation numbers may occur (and not only the integers zero, one and two). As basis functions that represent the atomic orbitals, numerical atomic orbitals (NAOs) are used, which are computed with XATOM [24]. Since valence orbitals deform strongly depending on the occupation of inner shells [23], NAOs are used as basis functions that are adapted to the inner-shell electronic configuration. For example, in Chapter 3 different atomic basis functions were used in the molecular calculation for iodine with one or two holes in the 4*d* subshell.

The time-dependent population of the bound-electron configurations is described by coupled rate equations in the form of Pauli-Master equations

$$\frac{d}{dt}P_I(t) = \sum_{I' \neq I} \left[\Gamma_{I' \to I} P_{I'}(t) - \Gamma_{I \to I'} P_I(t)\right] , \tag{2.19}$$

where $P_I(t)$ denotes the population of the electronic configuration $I$ at time $t$. $\Gamma_{I' \to I}$ and $\Gamma_{I \to I'}$ are the rates which lead to augmentation and depletion of the electronic configuration $I$, respectively, due to transitions between the configuration $I$ and all other configurations $I'$. Transitions considered are photoionization, Auger decay and fluorescence. The time-dependent photoionization rates are calculated as

$$\Gamma_{I \to I'} = \sigma_{I \to I'} J(t) \tag{2.20}$$

from the instantaneous X-ray flux density $J(t)$ at time $t$ and the computed photoionization cross section $\sigma_{I \to I'}$ [24, 27], for a transition between configuration $I$ and $I'$. Resonant excitations and relativistic effects are not included in the calculations presented in this Ph.D. thesis. The rate equation approach had already been successfully applied in the modeling of X-ray-induced multiple ionization [54, 87, 88] before the release of XATOM. [24] For details on our rate equation approach the interested reader is referred to Ref. [86], where also references for a derivation of the rate equations are given. [89–91] Note that our approach constitutes a nonperturbative treatment of sequential multiphoton ionization as we do not assume that the population of the initial (neutral) configuration $\mathrm{P}_{I_0}(t)$ remains close to unity at all times. [86] This is a good assumption at the high X-ray intensities employed in this Ph.D. work, where the systems typically reach very high final charge states.

In the calculations with XATOM and XMOLECULE the coupled, first-order differential equations in Eq. (2.19) are integrated numerically using the fourth-order Runge-Kutta method. [24, 27]

### 2.1.5 X-ray pulse parameters

In all calculations the intense femtosecond X-ray pulse is simulated using a Gaussian envelope with given temporal full-width at half-maximum (FWHM). In reality, most XFELs currently operate on the principle of self-amplification of spontaneous emission (SASE) for generating the X-ray pulses, which inherently results in a temporal distribution composed of several spikes. [92]

Moreover, the spike structures vary shot by shot. [93] Measuring the temporal profile of the X-ray free-electron laser (XFEL) pulse using the X-band transverse deflecting cavity (XTCAV, details given in Ref. [94]), and employing the average over many single-pulse measurements in the simulations yielded in Ref. [21] much better agreement with experimental data than the calculations for a Gaussian-shaped pulse. However, such a characterization of the temporal pulse profile was not performed in the experiment described in Chapter 4.

Beside the **temporal shape**, the X-ray pulse is specified in our calculations by the **photon energy**. Throughout the work photon energies between 1 keV and 2 keV are employed, i.e., the interaction between atoms and molecules and intense soft X-rays is investigated. The third pulse quantity which is necessary for our theoretical modeling is the X-ray **fluence**, i.e., the number of X-ray photons impinging on the sample per unit area. All calculations are performed for one, spatially constant fluence. Please note that experimental data, however, typically do not correspond to a spatially constant fluence, but to a spatial fluence distribution. It is feasible to determine the experimental X-ray fluence on target and the spatial beam profile using a calibration procedure as described in Refs. [21, 95], where charge state distributions of light atoms such as argon or neon are recorded under the same experimental conditions as applied to the system of interest. Theoretical charge state distributions of the light atom are then fitted to the experimental ones, thus identifying a percentual beamline transmission and the relative abundance of the fluence values in the interaction volume. The thus obtained fluence distribution function can then be used in the calculations which are later compared with the corresponding experimental results. [21] Such argon calibration data were recorded during the beam time described in Chapter 4, but at the present moment the analysis of the experimental argon charge state distributions has not been completed. Therefore I could not utilize such a fluence distribution function in my calculations.

## 2.2 XATOM

XATOM [24] is the *ab initio* toolkit of choice for simulating the interaction between high-intensity X-rays and atoms. It is based on nonrelativistic quantum electrodynamics and perturbation theory, as described in Ref. [76]. The electronic structure calculation is similar to the Herman-Skillman code [82] frequently used in atomic physics, aside from the numerical grid method employed. [24] XATOM can compute the following X-ray-induced atomic processes [58]: photoionization cross sections, X-ray fluorescence rates, Auger and Coster–Kronig decay rates, elastic X-ray scattering cross sections and their dispersion correction [96], Compton (i.e., inelastic) scattering cross sections [97] and shake-off branching ratios [84]. The toolkit has been successfully applied in the modeling of experiments with noble gases carried out at XFELs. [84, 98–101] XATOM can either solve the rate equations that are used to model the time-dependent population of the electronic configurations (see Section 2.1.4) by direct time propagation or, if the number of coupled rate equations is large, a Monte Carlo approach [100, 102] can be used. The Monte Carlo approach can be combined with precalculated atomic data. Alternatively, one can choose to calculate atomic data for a certain electronic configuration only if the configuration is de facto visited during an ionization pathway determined by the Monte Carlo sampling. [100] Thus, atomic data are computed only when they are required. This computationally efficient Monte Carlo procedure for both evaluating atomic data and searching probable ionization pathways enables the modeling also of heavy atoms, and is called "Monte Carlo on-the-fly" in this thesis.

The atomic calculations from XATOM serve as a basis and as input for the toolkits XMOLECULE [23] and XMDYN [58], respectively, which are dedicated to the modeling of polyatomic systems (see Sections 2.3 and 2.4 for details). For further details on XATOM the reader is referred to Ref. [24], where also the equations are given that underlie the computation of the photoionization cross sections as well as the Auger and fluorescence decay rates. An executable of XATOM is available via XRAYPAC. [103] Results from XATOM are presented in Chapters 3 and 4 of this Ph.D. thesis.

## 2.3 XMOLECULE

XMOLECULE [23] is the *ab initio* toolkit for calculating efficiently the electronic structure of molecules irradiated by high-intensity X-rays. Molecular orbitals are constructed as linear combination of atomic orbitals (MO-LCAO) which are represented by core-hole adapted basis functions obtained from XATOM [24] as numerical atomic orbitals. Using the Hartree-Fock-Slater method, the Roothaan-Hall-type equations [69] are solved in a self-consistent manner for ground and excited states (see Section 2.1.2 for details). XMOLECULE has successfully modeled the X-ray multiphoton ionization of molecules at the XFEL LCLS [21, 104, 105], including the intramolecular electron rearrangement that considerably augments the degree of ionization compared to isolated atoms. [21]

Like XATOM, XMOLECULE can solve the coupled rate equations either by direct time propagation, by using a Monte Carlo approach with a precalculated table of molecular data, or by using a Monte Carlo approach in which molecular data are calculated on the fly only if required. XMOLECULE treats electrons quantum mechanically and finds approximate solutions to the electronic Schrödinger equation. In order to describe nuclear dynamics, the nuclei are propagated classically along a kinetic Monte Carlo trajectory. The forces acting on them are derived from the gradient of the energy of the electronic subsystem with respect to the nuclear positions. The molecular gradients, transition rates and photoionization cross sections are computed on the fly for a given electronic configuration and molecular geometry.

In the calculation of Auger and fluorescence rates as well as photoionization cross sections, the molecular orbitals of the initial-state configurations are employed to calculate the transitions to all final-state configurations, applying Koompans' theorem (see Section 2.1.3). The equations utilized by XMOLECULE for the calculation of the photoionization cross sections, the Auger and fluorescence decay rates are given in Ref. [27]. For the fluorescence rates, transition dipole matrix elements between the molecular orbitals involved in the fluorescence decays are evaluated.

Since the description of molecular electronic continuum wavefunctions is challenging [106, 107], they are approximated as atomic continuum wavefunctions [27] that are supplied by XATOM [24]. For the photoionization cross sections, the molecular transition dipole matrix elements are expressed in the MO-LCAO approach with atomic basis functions from XATOM [24], and only such transition dipole matrix elements are taken into account where all basis functions as well as the atomic continuum wavefunction are located on the same atom.

Auger decay is commonly considered a mostly intraatomic process at the atom on which the core hole is located. Consequently, in the computation of Auger decay rates only such electron interaction matrix elements are taken into account where all atomic basis functions are located on the atom of the core hole. [27] This approach is known as one-center approximation [108–113] and produces good results compared to experiment. [110, 113]

For further details on XMOLECULE the reader is referred to Refs. [23, 27]. Results from XMOLECULE are shown in Chapters 3 and 4 of this Ph.D. thesis.

## 2.4 XMDYN

As the abbreviation XMDYN for X-ray Molecular Dynamics already suggests, XMDYN [58] is the theoretical toolkit which combines atomic *ab initio* X-ray physics with classical molecular dynamics to simulate dynamics of matter exposed to high intensity X-rays. In a hybrid quantum-classical approach neutral atoms, atomic ions and free electrons are treated as classical particles. Their positions are propagated using the classical molecular dynamics (MD) technique, i.e., Newton's equations of motion are solved. In the simulation, all charged particles interact via Coulomb forces. Bound electrons are modeled as quantum electrons which are assigned to atomic orbitals of the atomic sites (molecular states are disregarded). The electronic configurations are described via the occupation numbers of the atomic orbitals. For every new electronic configuration that emerges in the XMDYN simulation, including all multiple-hole states, relevant atomic data are supplied by the *ab initio* toolkit XATOM [24], i.e., orbital energies as well as a list of possible atomic processes (e.g., photoionization, Auger decay and fluorescence) and their corresponding photoionization cross section or transition rate. These data are either loaded from a precalculated table of atomic parameters for the respective electronic configuration, or XATOM is automatically called to calculate the parameters "on the fly". Based on these atomic data, photoionization, Auger and fluorescence decay are treated as stochastic

processes that have a certain likelihood to happen, and a Monte Carlo algorithm is utilized to generate an ionization pathway consisting of a sequence of bound-electron configurations.
The XMDYN modeling approach has been validated by achieving good agreement with experimental studies on buckminsterfullerene ($C_{60}$) molecules [114–116] as well as noble gas clusters [117], irradiated by XFEL pulses in each case. Also in Chapter 4 of this Ph.D. thesis a good agreement between XMDYN and experimental results is found for the XFEL-induced Coulomb explosion imaging of 2-iodopyridine and iodopyrazine molecules.
For further details on XMDYN, especially on the numerical procedure, the reader is referred to Ref. [58] An executable of XMDYN is available via XRAYPAC. [103] Results from XMDYN are presented in Chapter 4 of this Ph.D. thesis.

### 2.4.1 Classical over-the-barrier model employed in XMDYN

XMDYN has recently been extended [59, 60] to include electron transfer between atoms or atomic ions based on a classical over-the-barrier model. Using this model, critical distances for charge transfer were obtained which are in good agreement with values from time-resolved experiments. [34, 35]

In the following, the classical-over-the-barrier model as it is implemented in XMDYN will be explained in detail, following in part Ref. [118], because the model plays a prominent role in this Ph.D. thesis: in Chapter 4 it is applied, also with substantial further developments to its implementation in XMDYN. In Chapter 5 an alternative scheme for electron transfer in the XMDYN framework, based on quantum mechanics, is presented.

We now consider electron transfer from atom $D$ (donor) to atom $A$ (acceptor) in the over-the-barrier picture. In XMDYN the diatomic donor-acceptor model is applied to identify if electron transfer between a pair of atoms in a polyatomic system shall be executed in the next time step. In every time step it is checked for electron transfer between all pairs of atoms in the system, with the order of the examined atoms chosen randomly.

The implementation follows for the most part the conventional over-the-barrier model as described in Ref. [61]. Accordingly, an electron is transferred from the donor atom $D$ to the acceptor atom $A$ if it has sufficient energy to overcome the potential barrier between the atoms. The electron which is considered for electron transfer experiences a potential which is given by the superimposed Coulomb potentials of the two ions,

$$V(\vec{r}) = -\frac{Q_D + 1}{|\vec{r} - \vec{r}_D|} - \frac{Q_A}{|\vec{r} - \vec{r}_A|}, \tag{2.21}$$

where $Q_D$ and $\vec{r}_D$ ($Q_A$ and $\vec{r}_A$) denote the charge and position of the donor (acceptor), respectively. The term $Q_D + 1$ takes into account that the electron does not feel its own shielding of the donor nuclear charge.

The height of the potential barrier $V_b$ is given by the one of the saddle point along the straight line which connects the donor and acceptor atoms,

$$V_b = -\frac{(\sqrt{Q_D + 1} + \sqrt{Q_A})^2}{R}, \tag{2.22}$$

where $R := |\vec{r}_A - \vec{r}_D|$ denotes the donor-acceptor distance. Applying first-order perturbation theory within the electrostatic monopole approximation, the donor energy level $E_D$ is given by the atomic orbital energy $\epsilon_D$, influenced by the electrostatic interaction with acceptor atom $A$

$$E_D = \epsilon_D - \frac{Q_A}{R}. \tag{2.23}$$

In the monopole approximation the potential behaves as if all the charge of the acceptor $Q_A$ was a point charge, i.e., the spatial extension of nucleus and atomic orbitals are neglected. Consequently, this is a good approximation if the distance between the atoms is large in comparison with the spatial extension of the electron clouds.

Different from Ref. [61] we not only calculate the atomic orbital energies of hydrogen and hydrogenlike systems, but also atomic orbital energies of any atom or atomic ion in any charge state, using XATOM [24].

In XMDYN electron transfer from donor to acceptor is performed when the electron at the donor possesses an energy which exceeds the height of the potential barrier, i.e., when the condition

$$E_D > V_b \tag{2.24}$$

is fulfilled. Hence, we do not take into account any quantum tunneling through the potential barrier. Equation (2.24) is also a prerequisite for electron transfer in the work by Ryufuku and Sasaki [61]. However, they demand a second condition which can be rewritten as

$$E_D = E_A, \tag{2.25}$$

where $E_A$ denotes the acceptor energy level with a vacancy which the electron occupies after the transfer. By analogy with $E_D$, $E_A$ is given by

$$E_A = \epsilon_A - \frac{Q_D}{R}, \tag{2.26}$$

with $\epsilon_A$ being the atomic orbital energy computed with XATOM.

Equation (2.25) shall ensure energy conservation when performing electron transfer. In the previous XMDYN studies with charge transfer [59, 60] as well as in the early stages of the Coulomb explosion imaging project, Equation (2.25) was disregarded, and electron transfer was performed regardless of the energy difference between $\epsilon_D$ and $\epsilon_A$, or $E_A$ and $E_D$. To compensate, a sudden kinetic energy transfer was given to the ion cores in order to satisfy energy conservation. This approach led to artifacts in the Newton plots, which was corrected in the course of the project. See Chapter 4 for more details.

# Chapter 3

# Iodopyridine Isomers Irradiated with Intense, Femtosecond Soft X-ray Pulses

In this chapter computational investigations on the regioisomers 2-, 3- and 4-iodopyridine in the soft X-ray regime are presented. The charges in the molecular calculations are compared with the ones obtained for independent atoms, in order to inspect if a molecular ionization enhancement is also found for irradiation with intense **soft** X-ray pulses. First, the choice of the computational method is justified and the calculation setup is outlined. The remaining sections present results for the total molecular charges of the isomers as well as partial charges of the individual atoms for various pulse parameters, and compare those with the charges obtained in the independent-atom picture.

## 3.1 Choice of computational method

I simulated the interaction between the iodopyridine isomers and the intense, soft X-rays using the *ab initio* toolkit XMOLECULE [23], as it has proven to model reasonably well the molecular ionization enhancement of iodomethane in ultraintense hard X-ray pulses. [21] In order to keep the computational effort feasible, nuclear dynamics are not included, since doing so would have multiplied the computation time approximately by a factor of six (∼six weeks instead of ∼one week for one XMOLECULE Monte Carlo trajectory). This approximation is justified by the fact that in the iodomethane and iodobenzene studies the charge rearrangement predominantly happens prior to fragmentation. [21, 22] For quantifying the molecular ionization enhancement, I compare the molecular calculations with calculations for independent atoms, which were obtained using XATOM [24].

## 3.2 Calculation setup

I performed geometry optimizations for neutral 2-, 3- and 4-iodopyridine using GAMESS [119] at the RHF theory level with a 3-21G* basis set. This method-basis combination yields bond lengths for 2-iodopyridine which are in reasonably good agreement with experimental values. [120] For XMOLECULE calculations, I used numerical atomic orbitals from XATOM, adapted to the inner-shell electronic configuration, as basis functions. Specifically, the minimal basis set was extended by $5d$, $6s$, $6p$ and $6d$ basis functions on iodine. As in the iodobenzene study [22], the electronic structure, transition rates and photoionization cross sections of every multiple-hole electronic configuration that was formed during the ionization dynamics were taken into account by employing the Monte Carlo on-the-fly technique [100], both in the usage of XMOLECULE and of XATOM.

I employed photon energies of 1.2 keV and 2 keV and assumed X-ray pulses with a Gaussian pulse envelope of 30 fs full-width at half-maximum (FWHM). In the calculations with independent atoms the fluence was varied between $4 \times 10^8$ photons/µm$^2$ and $4 \times 10^{14}$ photons/µm$^2$, and for each data point in the fluence maps 200 XATOM Monte Carlo on-the-fly trajectories were run. In the full molecular model a low fluence of $1 \times 10^{11}$ photons/µm$^2$ and a very high fluence of $2 \times 10^{13}$ photons/µm$^2$ were chosen, and $46 - 50$ XMOLECULE Monte Carlo on-the-fly trajectories were run for each data point.

## 3.3 Results and discussion

### 3.3.1 Photoionization cross sections

At photon energies of 1.2 keV and 2 keV, the ratio between the total photoionization cross sections of iodine and carbon is an order of magnitude smaller than at 8.3 keV (see Table 3.1), which was the photon energy used in the iodobenzene and iodomethane studies [21, 22].

TABLE 3.1: **Ratio of the total atomic photoionization cross sections of neutral iodine and neutral carbon.** Values are calculated with the XATOM [24] toolkit, given for different photon energies.

| Photon energy [eV] | $\frac{\sigma_{\text{Total}}(I)}{\sigma_{\text{Total}}(C)}$ | |
|---|---|---|
| 1200 | $\frac{1.39\,\text{Mb}}{2.64\times10^{-2}\,\text{Mb}} \approx$ | 53 |
| 2000 | $\frac{4.21\times10^{-1}\,\text{Mb}}{6.02\times10^{-3}\,\text{Mb}} \approx$ | 70 |
| 8300 | $\frac{5.23\times10^{-2}\,\text{Mb}}{7.51\times10^{-5}\,\text{Mb}} \approx$ | 696 |

Hence, in the soft X-ray regime it cannot be excluded a priori that the electrons of the carbon and nitrogen atoms are directly photoionized without any prior electron rearrangement towards the iodine site.

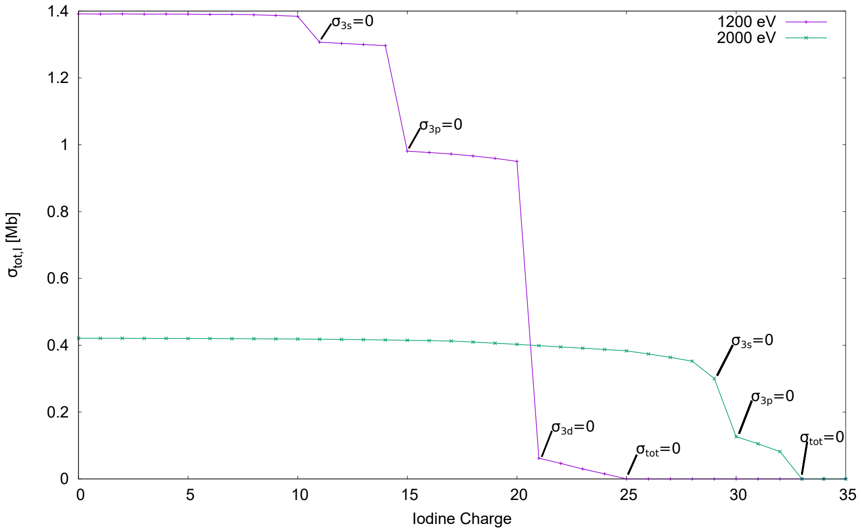

FIGURE 3.1: **Total atomic photoionization cross section of iodine for 1.2 keV and 2.0 keV as a function of the iodine charge,** calculated with the XATOM [24] toolkit.

I will start the detailed discussion with the 1.2 keV case and will subsequently proceed to 2.0 keV.
A photon energy of 1.2 keV is above the *M*-, *N*- and *O*-edges of neutral iodine. Positive charges on the iodine shift the ionization edges towards increasingly higher binding energies. Consequently, with increasing iodine charge, certain ionization channels become energetically unavailable, which is reflected in stepwise declines in the total photoionization cross section as a function of the iodine charge. Figure 3.1 shows the calculated atomic photoionization cross section of iodine for photon energies of 1.2 keV and 2 keV as a function of charge state. As can be seen, starting from a charge of +11, the iodine 3*s* binding energy shifts above 1.2 keV and the total cross section calculated for 1.2 keV becomes smaller. Please note that I am discussing here both calculated atomic binding energies and calculated atomic photoionization cross sections despite dealing with the molecules 2-, 3- and 4-iodopyridine. Considering that the largest part of the total photoionization cross section of iodine is made up of inner-shell contributions, the associated error should, however, be small. From an iodine charge of +21 on, exclusively the iodine *N*-shell contributes to the total cross section, giving rise to a further reduction of the total cross section.

At an iodine charge of +25 the total photoionization cross section drops to zero because all remaining electrons are in subshells with binding energies above 1.2 keV. This means that, once an iodine charge of +25 is reached during the pulse, further absorption of photons can (in the independent-atom picture) only take place as direct photoionization of carbon or nitrogen or resonant excitation of iodine electrons. The latter is not included in the calculations.

Figures 3.2(a) and 3.2(b) show a comparison between the atomic photoionization cross sections of iodine, carbon and nitrogen as a function of charge state. The comparison indicates that for 1.2 keV photon energy, starting from an iodine charge of +23, the total iodine and the total carbon and nitrogen photoionization cross sections become comparable.

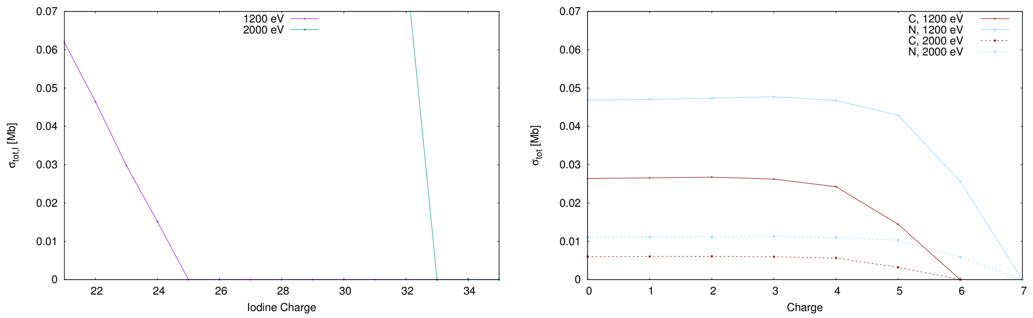

(a) Cutout of Fig. 3.1 for the high iodine charges.

(b) Carbon and nitrogen.

FIGURE 3.2: **Comparison between the total atomic photoionization cross sections of iodine, carbon and nitrogen,** for 1.2 keV as well as 2.0 keV, as a function of charge state. Calculations were performed with the XATOM [24] toolkit.

With a photon energy of 2.0 keV the total photoionization cross section of neutral iodine lowers by a factor of 3.3 (see Fig. 3.1) as compared to 1.2 keV. The $K$- and $L$-edges are still energetically out of reach. As a result of the higher photon energy the total photoionization cross section drops to zero at a higher iodine charge of +33 instead of +25. Unlike in the 1.2 keV case, there is no range where exclusively the $N$-shell contributes to the total photoionization cross section because the $M$-edges exceed 2 keV for high iodine charges around +30 that correspond to electronic configurations with an already empty $N$-shell. It is interesting to note that the 1.2 keV and 2.0 keV iodine cross section graphs intersect at an iodine charge of $\sim$+21. The total photoionization cross section for neutral carbon at 2 keV is lowered more than the iodine one, by a factor of 4.4, thus leading to an increased ratio $\frac{\sigma_{\text{Total}}(I)}{\sigma_{\text{Total}}(C)}$ in Table 3.1 as compared to the 1.2 keV case (see page 20).

### 3.3.2 Fluence maps of the total molecular ionization enhancement

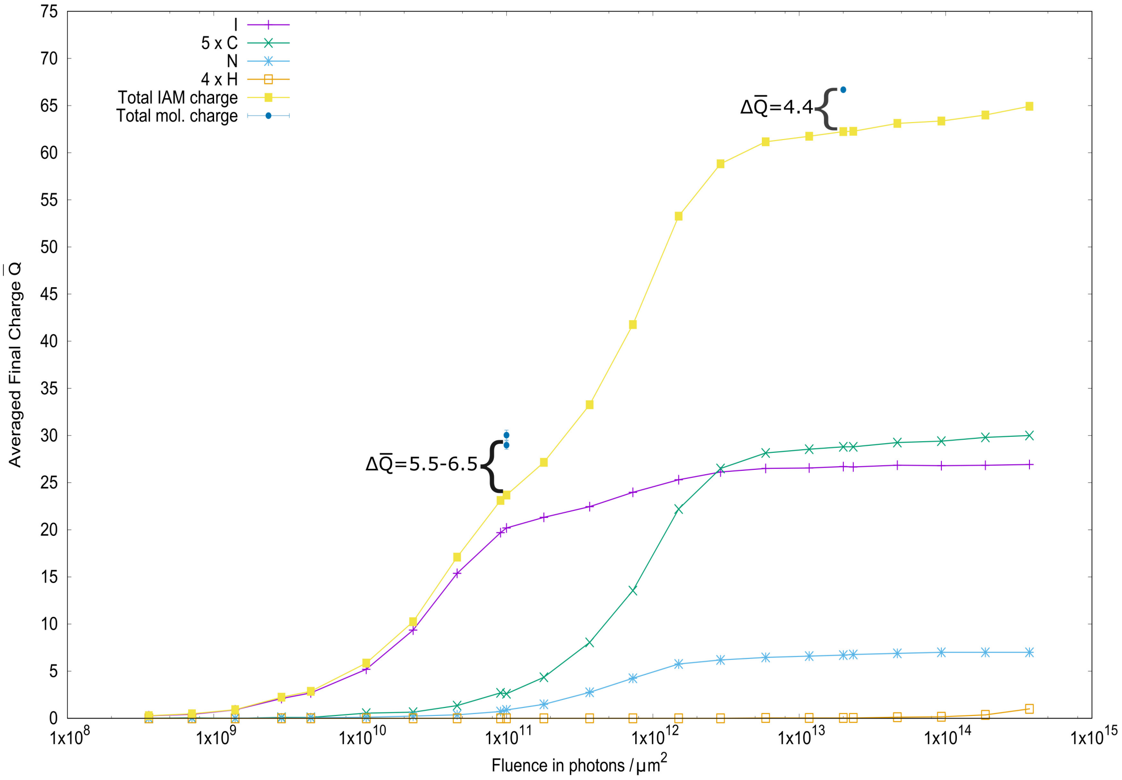

FIGURE 3.3: **Fluence map of the total molecular ionization enhancement at 1.2 keV.** Average total molecular charge from XMOLECULE [23] for an X-ray pulse with 30 fs FWHM: $+30.0 \pm 0.5$ for 2-iodopyridine and $+29.0 \pm 0.4$ for 4-iodopyridine at $1 \times 10^{11}$ photons/μm$^2$, and $66.7 \pm 0.2$ for 4-iodopyridine at $2 \times 10^{13}$ photons/μm$^2$. The error bars indicate the standard error of the mean. Also given are the total charges and the elemental group charges in the independent-atom model for a range of fluences, as calculated using XATOM [24].

Figure 3.3 illustrates the fluence dependence of the total molecular ionization enhancement at 1.2 keV. The figure shows the total charges in the full molecular model and within the independent-atom model (IAM). The average total molecular charge in the IAM is given as sum of the average charges of the independent atoms. The charges of the elemental groups constituting the IAM are also shown in the figure (chemical formula of iodopyridine: $C_5H_4IN$). I want to analyze the difference $\Delta\bar{Q}$ between the average total charge in the molecular calculation for the respective isomer $\bar{Q}_{\text{tot,mol}}$ and the average total charge in the independent-atom calculation $\bar{Q}_{\text{tot,IAM}}$. At a fluence of $1 \times 10^{11}$ photons/μm$^2$ I obtain

$$\Delta\bar{Q}_{\text{4-Iodopyridine}} = \bar{Q}_{\text{tot,mol,4-Iodopyridine}} - \bar{Q}_{\text{tot,IAM}} = +29.0 - (+23.5) = +5.5$$

$$\Delta\bar{Q}_{\text{2-Iodopyridine}} = \bar{Q}_{\text{tot,mol,2-Iodopyridine}} - \bar{Q}_{\text{tot,IAM}} = +30.0 - (+23.5) = +6.5$$

This corresponds to a relative molecular ionization enhancement of +23 % and +28 %, respectively. Thus, here in the soft X-ray regime a large relative molecular ionization enhancement is found already for low fluences. In contrast, in the previous studies with hard X-rays [21, 22] a molecular ionization enhancement was observed only for higher fluences. This qualitatively different behavior is a consequence of the total photoionization cross sections having higher values at the lower photon energies (see Table 3.1 on page 20). The curves for the five carbon atoms and for the nitrogen atom reveal that for fluences greater than $1 \times 10^{11}$ photons/µm$^2$ direct photoionization of carbon and nitrogen atoms becomes important, i.e., an average carbon charge of at least $+0.5$ emerges in the independent-atom model. This implies that there is only a relatively small fluence window that is dominated by the pure CREXIM mechanism known from Ref. [21], with significant photoionization only on the iodine atom and the charges on the other atoms generated solely by electron rearrangement towards the positively charged iodine site. This fluence window is found above the one-photon absorption saturation of iodine and below the one-photon absorption saturation of carbon and nitrogen in Table 3.2.

TABLE 3.2: **Saturation fluences for one-photon absorption,** calculated with the XATOM [24] toolkit for carbon, nitrogen and iodine at two photon energies.

| Photon energy [eV] | C $\left[\frac{\text{photons}}{\mu\text{m}^2}\right]$ | N $\left[\frac{\text{photons}}{\mu\text{m}^2}\right]$ | I $\left[\frac{\text{photons}}{\mu\text{m}^2}\right]$ |
|---|---|---|---|
| 1200 | $3.8 \times 10^{11}$ | $2.1 \times 10^{11}$ | $7.2 \times 10^{9}$ |
| 2000 | $1.7 \times 10^{12}$ | $9.0 \times 10^{11}$ | $2.4 \times 10^{10}$ |

The photoionization probability of the neutral atoms per X-ray pulse can be estimated as

$$\sigma \times \mathcal{F} , \tag{3.1}$$

with $\sigma$ being the total photoionization cross section of the neutral atom. The X-ray fluence $\mathcal{F}$ is the X-ray flux density from Eq. (2.20) on page 12, integrated over time. Photoionization is saturated for

$$\sigma \times \mathcal{F} > 1 , \tag{3.2}$$

and the saturation fluence for one-photon absorption $\mathcal{F}_{\text{Sat}}$ is thus calculated as

$$\mathcal{F}_{\text{Sat}} = \frac{1}{\sigma} . \tag{3.3}$$

For a fluence exceeding the saturation fluence for one-photon absorption of iodine, $\mathcal{F} > \mathcal{F}_{\text{Sat}}(I)$, iodine absorbs at least one photon. Thus, the X-ray multiphoton regime is entered, in which CREXIM takes place, as high charges on the iodine are required to attract the electron density from the rest of the molecule. For fluences $\mathcal{F} > \mathcal{F}_{\text{Sat}}(N)$ charges on the light atoms are not only created by electron transfer to the heavy absorber iodine, but also significantly via direct photoionization of nitrogen and carbon atoms.

At 2 keV the fluence window between one-photon absorption saturation of iodine and one-photon absorption saturation of carbon and nitrogen is broader than at 1.2 keV (see Table 3.2). Figure 3.4 illustrates the fluence dependence of the total molecular ionization enhancement at 2.0 keV.

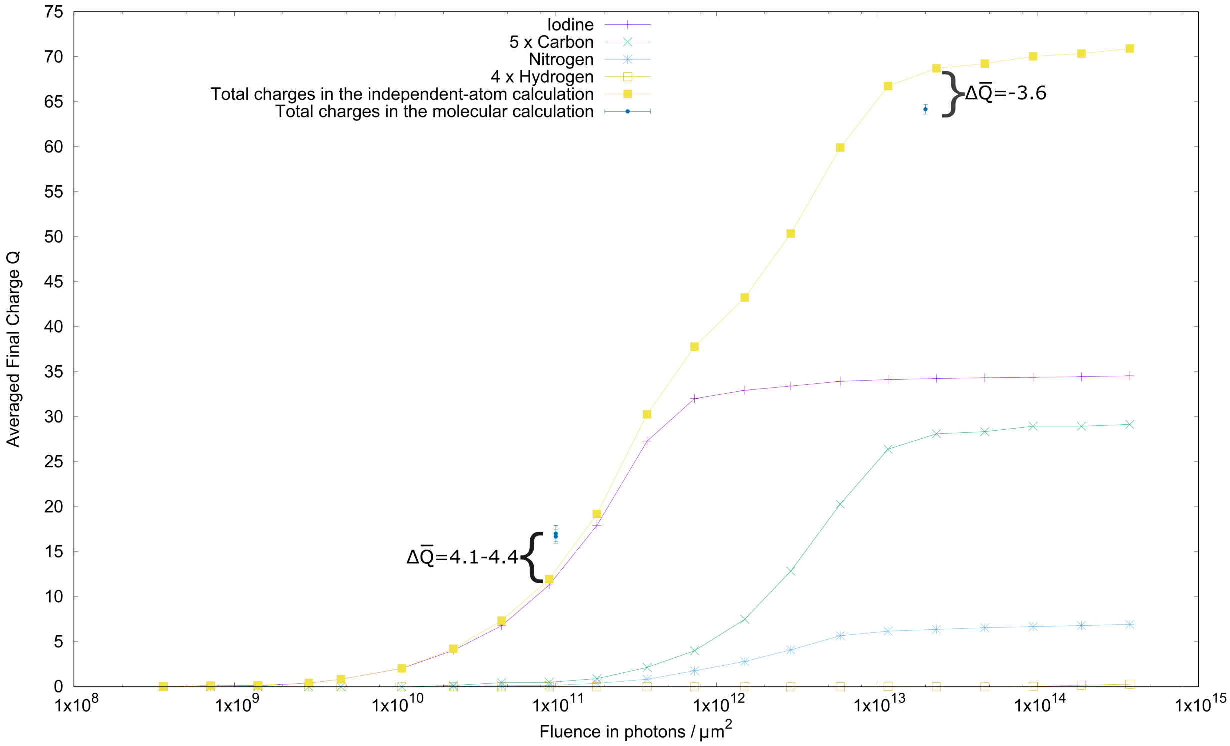

FIGURE 3.4: **Fluence map of the total molecular ionization enhancement at 2.0 keV.** Average total molecular charge from XMOLECULE [23] for an X-ray pulse with 30 fs FWHM: $+17.0 \pm 0.9$ for 2-iodopyridine and $+16.7 \pm 0.7$ for 4-iodopyridine at $1 \times 10^{11}$ photons/μm$^2$, and $+65.0 \pm 0.4$ for 4-iodopyridine at $2 \times 10^{13}$ photons/μm$^2$. The error bars indicate the standard error of the mean. Also given are the total charges and the elemental group charges in the independent-atom model for a range of fluences, as calculated using XATOM [24].

The relative molecular ionization enhancement at $1 \times 10^{11}$ photons/μm$^2$ is +33 % and +35 % for 2-iodopyridine and 4-iodopyridine, respectively (see also below).

$$\Delta\bar{Q}_{\text{4-Iodopyridine}} = \bar{Q}_{\text{tot,mol,4-Iodopyridine}} - \bar{Q}_{\text{tot,IAM}} = +16.7 - (+12.6) = +4.1$$

$$\Delta\bar{Q}_{\text{2-Iodopyridine}} = \bar{Q}_{\text{tot,mol,2-Iodopyridine}} - \bar{Q}_{\text{tot,IAM}} = +17.0 - (+12.6) = +4.4$$

In summary, at 2 keV compared to the 1.2 keV case, I observe a broader fluence window dominated by the pure CREXIM mechanism, and a slightly more pronounced relative molecular ionization enhancement.

The molecular ionization enhancement predicted for both photon energies stands in contrast with previous experiments in the soft X-ray regime [32–35] that suggest the charge of atoms in a polyatomic molecule can be inferred from the charges induced in the respective isolated atoms.

I will discuss the high-fluence case in Section 3.3.5. In Section 3.3.4 I will analyze how the low-fluence charges in the molecular and in the independent-atom calculation are spread over the individual atoms for the different regioisomers of iodopyridine. But before that we will have a look at the Mulliken partial charges of the neutral molecules in order to know from where we start chargewise in the neutral molecules.

### 3.3.3 Partial-charge distribution in the neutral molecules

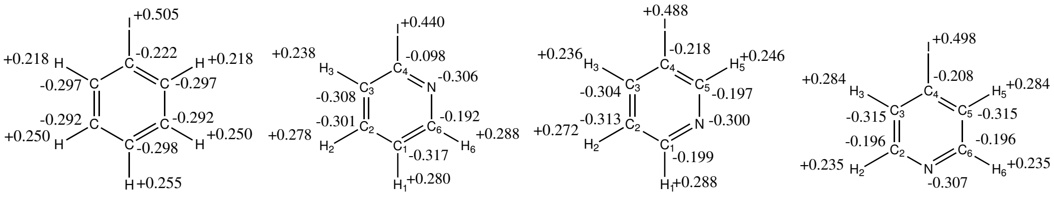

(a) Iodobenzene (b) 2-Iodopyridine (c) 3-Iodopyridine (d) 4-Iodopyridine

FIGURE 3.5: **Mulliken partial charges of the neutral molecules,** calculated with XMOLECULE [23].

Figure 3.5 shows the Mulliken partial charges [121] of neutral iodobenzene, 2-, 3- and 4-iodopyridine. It becomes clear that the replacement of a =CH- group by the isosteric =N- group, following the azalogy principle [122], does not significantly alter the Mulliken partial charges of the atoms. The nitrogen atoms in all three iodopyridine isomers have almost the same Mulliken charge, and this charge almost equals the partial charge of the carbon atoms in iodobenzene at the respective position in the aromatic ring. The high electronegativity of nitrogen shows up in slightly more positive partial charges of the neighboring carbon atoms. From electrophilic aromatic substitutions we know that a pyridyl group is altogether electron poorer than a phenyl group.

In summary, from this consideration the introduction of a nitrogen atom at different positions in the ring seems not to heavily modify the electronic structure compared to iodobenzene. In the iodobenzene study [22] for the highest fluence of $5 \times 10^{12}$ photons/µm$^2$, the three carbon atoms at the far end from iodine end up on average 1.5 charges more highly charged than the three carbon atoms closer to the iodine. Accordingly, one should analogously expect the final nitrogen charge in the next two sections to be significantly higher for the 3- and 4-iodopyridine isomers than for the 2-isomer.

### 3.3.4 Charge distribution for the low-fluence case

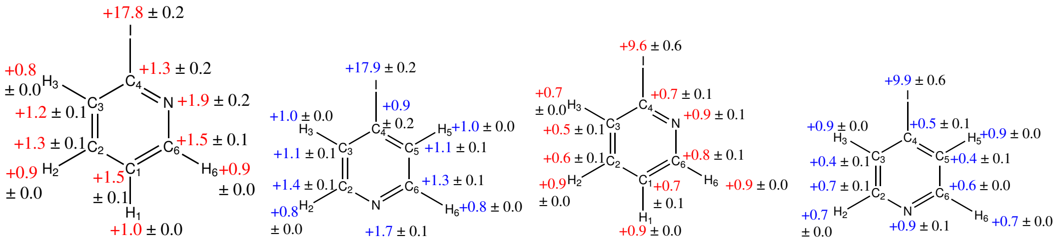

(a) 1.2 keV: 2-Iodopyridine $\bar{Q}=+30.0 \pm 0.5$

(b) 1.2 keV: 4-Iodopyridine $\bar{Q}=+29.0 \pm 0.4$

(c) 2.0 keV: 2-Iodopyridine $\bar{Q}=+17.0 \pm 0.9$

(d) 2.0 keV: 4-Iodopyridine $\bar{Q}=+16.7 \pm 0.7$

FIGURE 3.6: **Mulliken partial charges for the low-fluence case.** The averaged final Mulliken partial charges are given with standard error of the mean (SEM) for a fluence of $1 \times 10^{11}$ photons/µm$^2$. Given are also the averaged total molecular charges obtained from XMOLECULE [23].

Figure 3.6 shows the averaged final Mulliken partial charges of 2- and 4-iodopyridine after exposure to an X-ray pulse with a fluence of $1 \times 10^{11}$ photons/µm$^2$. In all four cases the nitrogen atom exhibits the highest charge among all atoms in the aromatic ring. One reason is that nitrogen has a higher total photoionization cross section than carbon for both photon energies, due to the one additional electron. Thus, the nitrogen charges are higher than the carbon charges also in the independent-atom calculation (see Table 3.3).

TABLE 3.3: **Independent-atom charges for the low-fluence case.** The averaged final charges are given with standard error of the mean (SEM), calculated with the XATOM [24] toolkit for $1.00 \times 10^{11}$ photons/µm$^2$. The number of trajectories is specified in the line below, respectively.

| Photon energy [eV] | $\bar{Q}$(I)± SEM | $\bar{Q}$(C)± SEM | $\bar{Q}$(N)± SEM | $\bar{Q}$(H)± SEM |
|---|---|---|---|---|
| 1200 | $+20.19 \pm 0.01$ | $+0.49 \pm 0.01$ | $+0.86 \pm 0.01$ | $+0.00 \pm 0.00$ |
| | 22200 tr. | 9000 tr. | 7900 tr. | 200 tr. |
| 2000 | $+11.87 \pm 0.03$ | $+0.10 \pm 0.01$ | $+0.23 \pm 0.01$ | $+0.00 \pm 0.00$ |
| | 27100 tr. | 2600 tr. | 6500 tr. | 200 tr. |

Equation (3.4) indicates how to estimate the average molecular ionization enhancement of atom $A$ due to CREXIM $\bar{q}_{\mathrm{CREXIM}}(A)$.

$$\bar{q}_{\mathrm{CREXIM}}(A) = \bar{q}_{\mathrm{Mull.,f}}(A) - q_{\mathrm{Mull.,n}}(A) - \bar{q}_{\mathrm{IAM}}(A) \tag{3.4}$$

With the difference between the averaged final Mulliken partial charge $\bar{q}_{\mathrm{Mull.,f}}(A)$ and the Mulliken partial charge in the neutral molecule $q_{\mathrm{Mull.,n}}(A)$, the effective charging enters. With the average charge in the independent-atom model $\bar{q}_{\mathrm{IAM}}(A)$ the charge increase of atom $A$ due to direct photoionization is subtracted. In this way, I obtain values for $\bar{q}_{\mathrm{CREXIM}}$ between $+0.6$ and $+1.3$ for the carbon atoms in both isomers at 1.2 keV. From the corresponding values for nitrogen, which are $+1.3$ and $+1.5$, we can conclude that alongside the higher photoionization cross section also a tendentially more efficient charge transfer to the iodine causes the nitrogen charge to be higher than the carbon charges.

The term mesomerism in chemistry describes the phenomenon that the bonding properties in some molecules cannot be reflected by one single structural formula. Instead, mesomeric structures can be derived by shifting electron pairs that all contribute to the real species. The true state of the molecule then lies in between the limits specified by the mesomeric structures. Figure 3.7 displays the mesomeric structures one can formulate for the iodopyridine isomers.

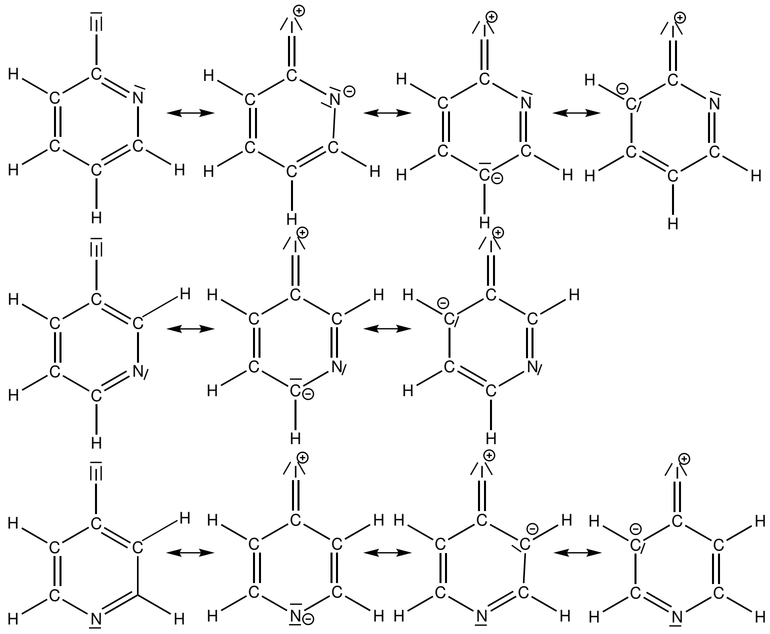

FIGURE 3.7: **Mesomeric structures of the iodopyridine isomers.** Displayed are the mesomeric structures of 2-iodopyridine (upper row), 3-iodopyridine (middle row) and 4-iodopyridine (bottom row).

One might think that these mesomeric structures explain why the charge transfer from nitrogen in the aromatic ring to the iodine is more efficient than from a carbon atom in the ring to the iodine. For both 2- and 4-iodopyridine one can formulate mesomeric structures involving a negative charge on the nitrogen atom. These structures are based on the +M effect of iodine and the -M effect of nitrogen. One might think that due to this increased charge density at the nitrogen atomic site electrons can be more easily transferred to the iodine than from carbon to iodine. In order to verify this, I performed additional calculations for 3-iodopyridine, for which it is not possible to formulate a mesomeric structure with a negative charge on the nitrogen atom (see middle row of Fig. 3.7). As indicated in Fig. 3.8, the nitrogen atom in 3-iodopyridine does receive the lowest final charge (+1.6 ± 0.1) as compared to the nitrogen charges in the other isomers (+1.7 ± 0.1; +1.9 ± 0.2). The difference, however, is subtle and within the error, i.e., perhaps the mesomeric effect contributes a little to the higher nitrogen than carbon charges for the 2- and 4-isomers.

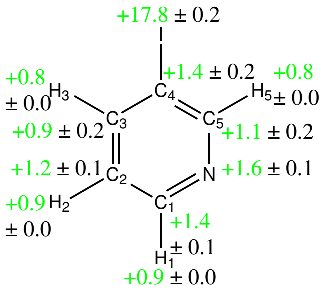

FIGURE 3.8: **3-Iodopyridine at low fluence.** The averaged final Mulliken partial charges are given with standard error of the mean (SEM), for 3-iodopyridine at 1.2 keV and 1 × $10^{11}$ photons/µm$^2$.

Figures 3.6(c) and 3.6(d) show the average final Mulliken partial charges at 2 keV and a fluence of 1 × $10^{11}$ photons/µm$^2$. All charges are lower than in the 1.2 keV case because, as I discussed in Section 3.3.1, the photoionization cross sections are smaller. As indicated in Table 3.3, direct photoionization of carbon and nitrogen atoms is almost negligible under these conditions. Based on the partial charges in Fig. 3.6 only the 4-isomer seems to clearly exhibit the iodobenzene charge distribution trend with higher partial charges further away from iodine. [22] The average molecular ionization enhancement $\bar{q}_{\text{CREXIM}}$ is shown in Fig. 3.9. It becomes clear that apart from the nitrogen charge also in 2-iodopyridine the relative charge change compared to the neutral molecule follows the iodobenzene charge distribution trend.

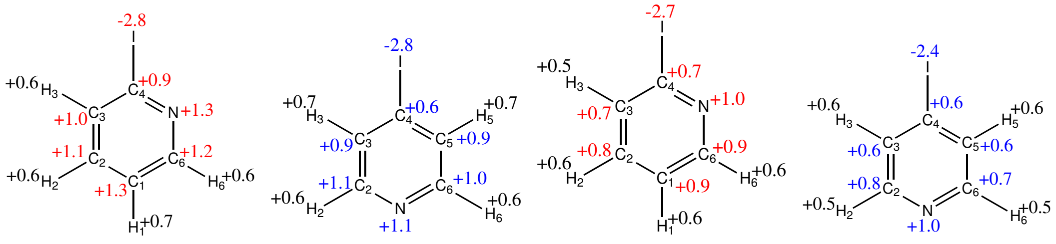

(a) 1.2 keV: 2-Iodopyridine

(b) 1.2 keV: 4-Iodopyridine

(c) 2.0 keV: 2-Iodopyridine

(d) 2.0 keV: 4-Iodopyridine

FIGURE 3.9: **Molecular ionization enhancement of the individual atoms.** The average molecular ionization enhancement due to CREXIM $\bar{q}_{\text{CREXIM}}$ (Eq. (3.4)) is indicated, for a fluence of 1 × $10^{11}$ photons/µm$^2$.

Contrary to the expectation I expressed in Section 3.3.3, neither the nitrogen Mulliken partial charges in Fig. 3.6 nor the nitrogen $\bar{q}_{\mathrm{CREXIM}}$ values in Fig. 3.9 are higher for the 4-isomer than for the 2-regioisomer of iodopyridine. At 2.0 keV the numbers are the same, and at 1.2 keV the 2-isomer features even a higher nitrogen partial charge and a higher $\bar{q}_{\mathrm{CREXIM}}(N)$ than the 4-isomer. At this point the reason is not clear. The overall ionization degree is presumably not sufficiently high for the electron density polarization from Ref. [22] to distinctly emerge.

It is interesting to compare the average hydrogen partial charges in Fig. 3.6: for both photon energies they are higher closer to the iodine for the 4-isomer, whereas for the 2-isomer they are higher further away from the iodine. As Figure 3.9 indicates, the molecular ionization enhancement amplifies this trend, which was already weakly preformed in the partial-charge distributions of the neutral molecules (see Fig. 3.5).

### 3.3.5 Charge distribution for the high-fluence case

For the highest fluence considered here, $2 \times 10^{13}$ photons/μm$^2$, and 1.2 keV photon energy the average total molecular charge of 4-iodopyridine is found to be $+66.7$. This average charge is reached after time propagation up to 300 fs. The extremely high value of $+66.7$ even slightly exceeds the maximum charge calculated for iodobenzene: $+66$ [22] (at 8.3 keV, $5 \times 10^{12}$ photons/μm$^2$ and 30 fs pulse FWHM). As can be seen in Fig. 3.3, the difference to the independent-atom charge, however, is not $+20$ as in the iodobenzene case [22], but only $+4.4$.

$$\Delta\bar{Q}_{\text{4-Iodopyridine}} = \bar{Q}_{\text{tot,mol,4-Iodopyridine}} - \bar{Q}_{\text{tot,IAM}} = +66.7 - (+62.3) = +4.4$$

The reason is that under the given conditions we do not deal with pure CREXIM, with photoionization only on the heavy iodine atom. At 1.2 keV there is much more direct photoionization of carbon and nitrogen atoms as compared to 8.3 keV, i.e., also as independent atoms, carbon and nitrogen become strongly ionized.

I will now analyze the average final Mulliken partial charges of the individual atoms in the molecular calculation in order to discuss the molecular ionization effects. The partial charges are depicted in Fig. 3.10 on the left side. The corresponding charges obtained from independent-atom calculations are shown in Table 3.4. It becomes clear that the 4.4 charges difference can mainly be ascribed to the four electrons of the hydrogen atoms. These electrons have a negligible probability of being ionized if they are part of isolated hydrogen atoms, as opposed to being embedded in a molecular framework. The hydrogen electrons are ejected via the CREXIM mechanism, i.e., they fill holes on heavier atoms and are emitted through photoionization or Auger decay at those atomic sites with higher ionization probability. This finding is in line with the molecular electron rearrangement predicted for the $H_2O$ molecule. [26, 27]

Except for hydrogen, all other atomic charges are almost the same in the molecular and in the independent-atom calculation. The carbon and nitrogen atoms end up fully ionized at this ultrahigh intensity, both in the atomic and the molecular calculation. The iodine charge is limited by the total (atomic) photoionization cross section of iodine that drops to zero at an iodine charge of +25, as we saw in Fig. 3.1 in Section 3.3.1. Slightly higher iodine partial charges than +25 can arise, e.g., due to Auger decays involving electrons from molecular orbitals with non-zero expansion coefficient on an iodine atomic orbital. In this way, the averaged final Mulliken charge of +26.4 for iodine can be understood.

On the left side of Fig. 3.13 the corresponding ionization changes of the individual atoms due to molecular effects are indicated.

TABLE 3.4: **Independent-atom charges for the high-fluence case.** The averaged charges are given with standard error of the mean (SEM), calculated with the XATOM [24] toolkit for $2.00 \times 10^{13}$ photons/µm$^2$. The number of trajectories is specified in the line below, respectively.

| Photon energy [eV] | $\bar{Q}$(I)± SEM | $\bar{Q}$(C)± SEM | $\bar{Q}$(N)± SEM | $\bar{Q}$(H)± SEM |
|---|---|---|---|---|
| 1200 | $+26.69 \pm 0.01$ | $+5.77 \pm 0.01$ | $+6.70 \pm 0.01$ | $+0.01 \pm 0.00$ |
| | 13400 tr. | 4200 tr. | 4000 tr. | 1200 tr. |
| 2000 | $+34.22 \pm 0.01$ | $+5.59 \pm 0.01$ | $+6.39 \pm 0.02$ | $+0.00 \pm 0.00$ |
| | 16900 tr. | 3800 tr. | 500 tr. | 200 tr. |

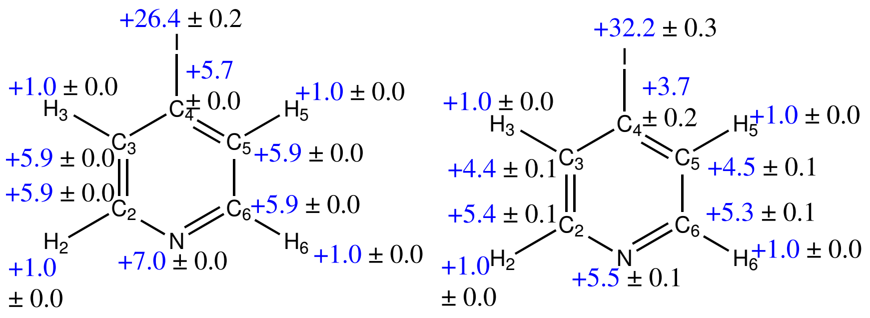

FIGURE 3.10: **Mulliken partial charges for the high-fluence case.** The averaged final Mulliken partial charges of 4-iodopyridine are given with standard error of the mean (SEM), at $2 \times 10^{13}$ photons/µm$^2$. The calculations were performed with XMOLECULE [23] for 1.2 keV (left) and 2.0 keV (right).

Interestingly and surprisingly, for the same fluence but 2.0 keV photon energy the total charge is in the independent-atom calculation 3.6 charges *higher* than in the molecular calculation (see Fig. 3.4).

$$\Delta\bar{Q}_{\text{4-Iodopyridine}} = \bar{Q}_{\text{tot,mol,4-Iodopyridine}} - \bar{Q}_{\text{tot,IAM}} = +65.0 - (+68.7) = -3.6$$

Such a "molecular ionization suppression" was not observed in any of the former studies [21, 22, 26, 27]. Figure 3.11 illustrates one of the underlying reasons, namely the energetic position of the ionization edges. Shown are the calculated cross sections for an isolated iodine atom and iodine in a molecule for 1.2 keV (left), and 2.0 keV (right), as a function of iodine charge state. In the molecular calculation all atoms in the pyridine ring (C, N, H) are assumed to be fully ionized. For an extremely high fluence of $2 \times 10^{13}$ photons/µm$^2$ this is likely the case. As can be seen, at 1.2 keV the ionization cross section drops to zero at the same charge of $+25$ for both cases with the ionization of the last 4*s* electron. Hence, the iodine charges in the molecular and atomic calculations are with $+26.4$ and $+26.7$ very similar. At 2.0 keV, on the contrary, ionization stops by two charges earlier in the molecular case than in the isolated atom case. Since in our molecular calculation the electrons are more tightly bound due to the electrostatic attraction from the surrounding bare nuclei, the fourth and third last 3*d* electron can only be photoionized in the atomic case. This effect could explain why the average iodine partial charge in the molecular calculation is 2.0 charges lower than in the calculation with independent atoms (+32.2 vs. +34.2).

The average charge on the ring is found to be lower by 1.6 charges in the molecular calculation than in the independent-atom calculation. We can additionally subtract the four charges of the hydrogens that are present in the molecular calculation and not in the atomic calculation. Then the question arises why the carbon atoms and the nitrogen atom are in sum 5.6 charges less charged in the molecular case than in the independent-atom calculation (in addition, see the $\bar{q}_{\text{CREXIM}}$ values on the right side of Fig. 3.13).

The relevant molecular and atomic photoionization cross sections are expected to be very similar. Striking is the observation of very late Auger decays in the molecular calculation under these conditions. Initially, all molecular calculations were performed with 300 fs propagation time. Then it was found that after 300 fs none of the trajectories run for 2000 eV and $2 \times 10^{13}$ photons/µm$^2$ had a vanishing total Auger rate, as is indicated in Table 3.5.

TABLE 3.5: **Percentage of trajectories exhibiting a vanishing total Auger rate after 300 fs and 10000 fs propagation time, respectively,** for 1200 eV and 2000 eV photon energy. A fluence of $2 \times 10^{13}$ photons/µm$^2$ is used.

| | 300 fs | 10,000 fs |
|---|---|---|
| 1200 eV | 65 % | 100 % |
| 2000 eV | 0 % | 25 % |

Hence, for this parameter combination the propagation time was prolonged to 10,000 fs. In this way, the total Auger rate could be brought down to zero for not more than 25 % of the trajectories, and the average total charge increased from $+63.8$ to $+65.0$ for the identical trajectories. Contrary to the

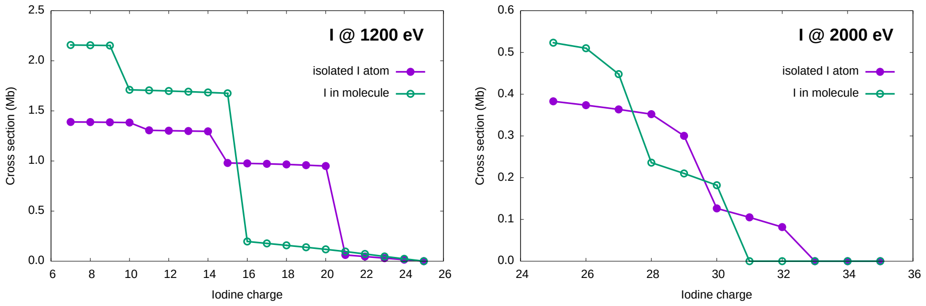

FIGURE 3.11: **Photoionization cross sections for an isolated iodine atom and for iodine in a charged molecular environment.** Shown are the total iodine photoionization cross sections as a function of iodine charge state for photon energies of 1.2 keV (left) and 2.0 keV (right). The atomic calculation was performed with XATOM [24], and the molecular calculation with XMOLECULE [23].[1]

molecular calculation, the atomic calculation is automatically propagated until the sum of all rates vanishes. Therefore the lower charge in the molecular calculation could be a consequence of the circumstance that 10,000 fs still mean a too short propagation time. It is known from a study on Xenon that $M$-shell Auger lifetimes increase strongly for charge states above $+25$ (Supplementary information of Ref. [98]). In the current molecular calculation the Auger lifetimes might additionally be overestimated by the one-center approximation [108–113] that is applied here in order to calculate the molecular Auger transition rates. [27] In this simplification only such electron interaction matrix elements are taken into account where all basis functions are located on the atom of the core hole. The one-center approximation has yielded good results compared to experiment (see, e.g., Refs. [110, 113]). In the present case of extremely highly charged molecules with delocalized valence orbitals, this approach might, however, lead to unrealistically long Auger lifetimes. This reasoning is supported by the average time-dependent occupation number of the C 1$s$ and N 1$s$ orbitals in the atomic and molecular calculation, that is shown in Fig. 3.12.

---

[1] This figure was kindly provided by Dr. Sang-Kil Son.

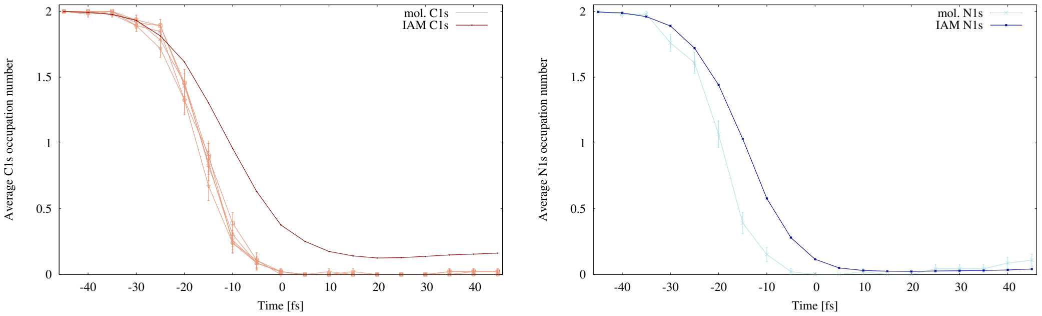

FIGURE 3.12: **Time-dependent occupation of the C 1*s* and N 1*s* orbitals in the atomic and molecular calculation.** The average occupation number of all five molecular C 1*s* orbitals and of the IAM C 1*s* orbital (left) as well as the average occupation number of the N 1*s* orbital in the molecular and IAM calculation (right) are shown, for the time interval between 45 fs before and after the pulse center. All results were obtained for 30 fs FWHM pulse duration, 2 keV photon energy and $2 \times 10^{13}$ photons/µm$^2$. 4100 (C 1*s*) and 6000 (N 1*s*) Monte Carlo trajectories were calculated with XATOM [24] for the independent-atom model.

From 20 fs before the pulse center onwards, the occupation of the C 1*s* and N 1*s* orbitals is considerably lower in the molecular case than in the atomic calculation. Since the C 1*s* and N 1*s* orbital photoionization cross sections in the presented atomic and molecular calculations are expected to be very similar (see also Ref. [27]), this difference must arise from discrepancies in the Auger transition rates. As opposed to the suspected too long Auger lifetimes in the presented molecular calculations, it is generally known that Auger and fluorescence decays in molecular environments are usually faster than in atoms due to the increased number of valence electrons being present. [110]

Ultimately, the lower carbon and nitrogen charges in the molecular calculation might thus be ascribed to a “molecular frustrated absorption [54, 123] effect” in the calculations: the electrons spend more time in valence orbitals than in core orbitals during the pulse due to overestimated Auger lifetimes, where the corresponding photoionization cross section is much smaller according to Table 3.6. Consequently, fewer photons are absorbed and eventually lower final charge states are reached.

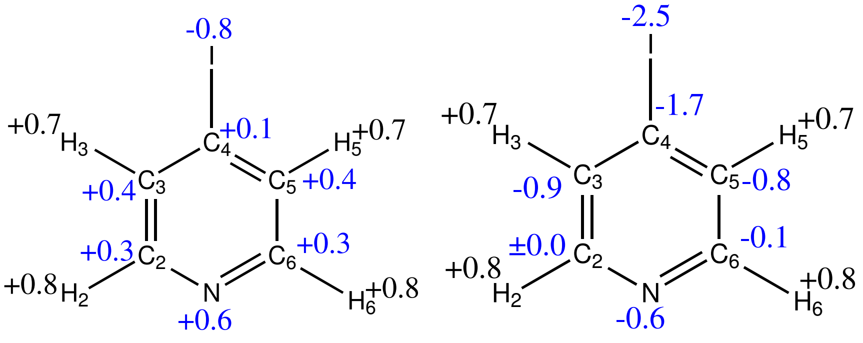

(a) 1.2 keV: 4-Iodopyridine (b) 2 keV: 4-Iodopyridine

FIGURE 3.13: **Molecular ionization changes of the individual atoms.** The average molecular ionization enhancement or suppression $\bar{q}_{\mathrm{CREXIM}}$ (Eq. (3.4)) is indicated, for a fluence of $2 \times 10^{13}$ photons/µm$^2$.

TABLE 3.6: **Subshell photoionization cross sections for different electronic configurations of $C^{5+}$,** calculated with XATOM [24].

| Photon energy [eV] | $\sigma_{C_{1s^1 2s^0 2p^0}}$ [Mb] | $\sigma_{C_{1s^0 2s^1 2p^0}}$ [Mb] | $\sigma_{C_{1s^0 2s^0 2p^1}}$ [Mb] |
|---|---|---|---|
| 1200 | $1.45 \times 10^{-2}$ | $1.57 \times 10^{-3}$ | $1.52 \times 10^{-4}$ |
| 2000 | $3.21 \times 10^{-3}$ | $3.68 \times 10^{-4}$ | $2.15 \times 10^{-5}$ |

In some XMOLECULE trajectories, even after 10 ps propagation time, there are still electrons occupying ring valence orbitals, i.e., the molecules do not reach the electronic ground state of the respective final charge state, for which it is expected that all remaining electrons are located at the iodine site, in analogy to iodobenzene with final charge +60. In Ref. [22] the incomplete electron transfer from the phenyl group to the iodine was explained with "huge potential barriers among highly charged ions", impeding full electron transfer from the ring to the iodine. However, as Figure 3.14 illustrates, in the present case there is no such potential barrier found between $I^{32+}$ and a $C_4^{5+}$ ion, where the last electron occupies a valence orbital (corresponding to the electron configurations C $1s^0 2s^0 2p^1$ and C $1s^0 2s^1 2p^0$ in the depicted atomic calculation).

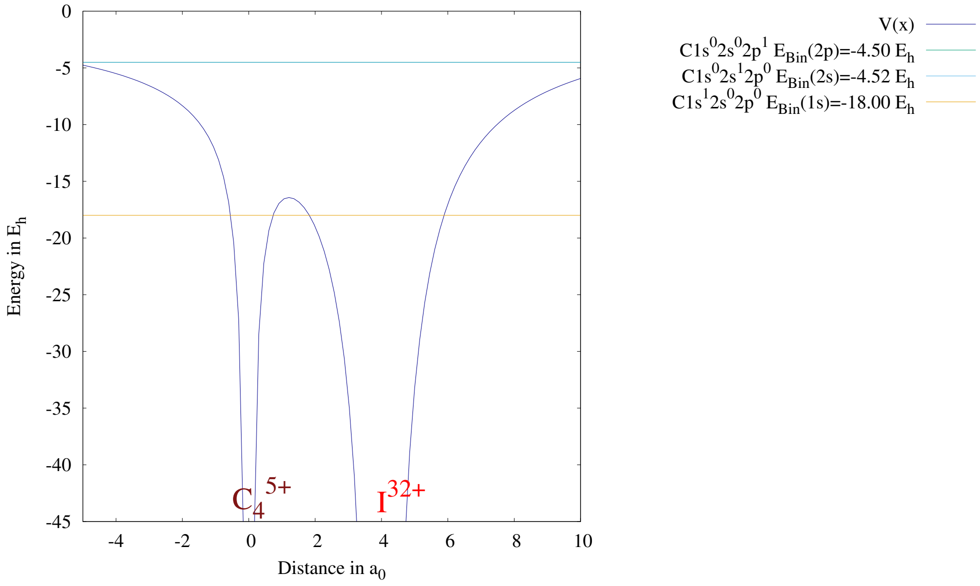

FIGURE 3.14: **Coulomb potential landscape between $C_4^{5+}$ and $I^{32+}$.** The potential $V(x) = -\frac{6}{|x|} - \frac{32}{|x-4|}$ is depicted (as in Section 4.5.2 the last electron on the $C_4^{5+}$ ion does not feel its own shielding of the nuclear charge). Also indicated are the binding energies of the last electron in different electronic configurations of $C^{5+}$, approximated as the respective orbital energies obtained from XATOM [24] (Koopmans' theorem [75]).

So potential barriers seem not to impede the transfer of the valence electron density from the pyridyl ring to the iodine. In XMOLECULE calculations the electron transfer towards the iodine finds expression in a shift of the molecular orbitals towards the iodine. In my understanding, this means that the occupied molecular orbitals change their character in a way that the iodine atomic orbital coefficients become greater in magnitude, therefore the contribution of the iodine atomic orbitals to the molecular orbitals increases.

Applying the Rydberg formula for hydrogen-like ions, I calculate that the computed C $1s^0 2s^0 2p^1$ and C $1s^0 2s^1 2p^0$ binding energies of ~-4.5 $E_h$ correspond to an energy level of $I^{32+}$ with a prinicipal quantum number $n = 11$, i.e., to a diffuse Rydberg orbital [124] far from the ion core (atomic units are used unless specified otherwise):

$$-\frac{1}{2}\frac{Z^2}{n^2} = -4.5 \tag{3.5}$$

$$-\frac{1}{2}\frac{32^2}{n^2} = -4.5 \tag{3.6}$$

$$-\frac{32^2}{n^2} = -9 \tag{3.7}$$

$$-32^2 = -9n^2 \tag{3.8}$$

$$n^2 = \frac{32^2}{9} = 113.\bar{7} \tag{3.9}$$

$$n = 10.\bar{6} \approx 11 \tag{3.10}$$

Obviously, $I^{32+}$ still has 21 electrons left, and not just one like a hydrogen-like atom or ion. Therefore, the Rydberg formula cannot be fully trusted in this case. Hence, I used XATOM to verify the result, and also XATOM yields a principal quantum number $n = 11$ ($I^{32+}$ 11*f* orbital energy -4.58 $E_h$; $I^{32+}$ 12*s* orbital energy -4.05 $E_h$). By contrast, for the outermost used 6*d* basis function for iodine, I calculated a considerably more negative orbital energy of -16.25 $E_h$ for $I^{32+}$. For comparison, for neutral iodine I obtain a 6*d* orbital energy of -0.03 $E_h$, thus illustrating how strongly the orbital energies are altered by the intense ionization dynamics.

These results point towards a basis set problem that causes the valence electron density of the pyridyl ring not to be transferred to the iodine and ejected there via the CREXIM mechanism. We know from Molecular Orbital Theory that atomic orbitals combine most effectively with other atomic orbitals that are of similar energy. Therefore, due to the insufficient basis set on iodine, the iodine atomic orbitals cannot mix effectively with the ring valence orbitals in the calculations. Diffuse Rydberg orbitals would need to be included in the basis set to facilitate the electron transfer from the ring atoms to the iodine.

The electron density remaining on the pyridyl ring on the right side of Fig. 3.10 is markedly polarized according to the pattern known from iodobenzene [22], with higher charges further away from the highly positively charged, and thus other positive charges repelling, iodine.

### 3.3.6 Temporal evolution of the charge build-up

XMOLECULE [23] provides not only static information such as the hitherto discussed final charge states but also time-dependent information throughout the whole ionization dynamics. In Fig. 3.15 the time evolution of the average Mulliken partial charges is depicted, for the 4-iodopyridine isomer at four different combinations of photon energy and fluence.

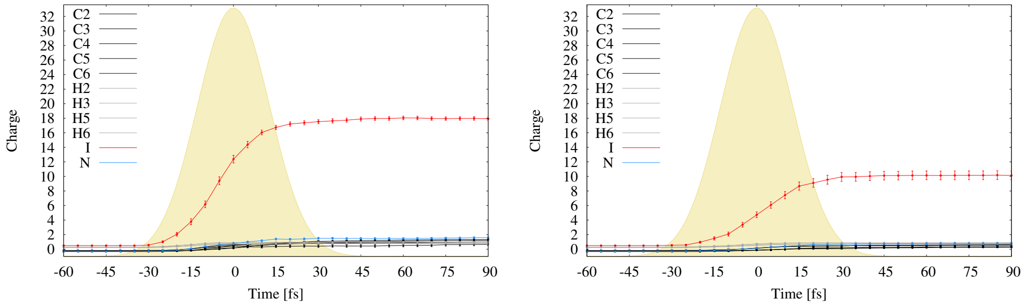

(a) 1.2 keV and $1\times10^{11}\,\frac{\mathrm{ph}}{\mu\mathrm{m}^2}$ (b) 2.0 keV and $1\times10^{11}\,\frac{\mathrm{ph}}{\mu\mathrm{m}^2}$

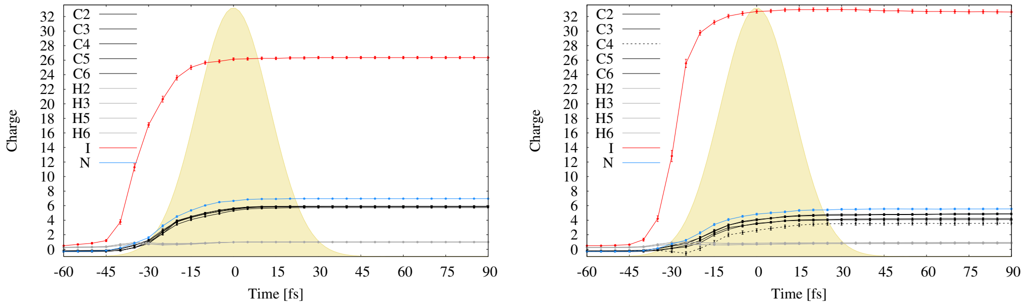

(c) 1.2 keV and $2\times10^{13}\,\frac{\mathrm{ph}}{\mu\mathrm{m}^2}$ (d) 2.0 keV and $2\times10^{13}\,\frac{\mathrm{ph}}{\mu\mathrm{m}^2}$

FIGURE 3.15: **Time evolution of the average Mulliken partial charges of all atoms of 4-iodopyridine for the four different photon energy and fluence combinations considered.** Indicated in yellow is a Gaussian pulse with 30 fs FWHM as I assume it in the calculations, with its center at 0 fs. The error bars indicate the standard error of the mean.

One sees immediately that for the low-fluence cases, the iodine charge has its steepest gradient when the X-ray pulse is most intense. In contrast, $2\times10^{13}$ photons/$\mu$m$^2$, is such an ultrahigh intensity that the average iodine charge reaches its maximum value already before the X-ray pulse reaches its peak intensity. Among all high-fluence trajectories the earliest photoionization was observed already 60 fs before the pulse center, for 1.2 keV photon energy. For 2.0 keV the earliest photoionization occurred later, 54 fs before the pulse center, due to the smaller photoionization cross sections at this photon energy (see Section 3.3.1). For $1\times10^{11}$ photons/$\mu$m$^2$ the earliest photoionization was found considerably later, for both photon energies 34 fs before the pulse peak.

Interestingly, in Fig. 3.15(d) $C_4$, which is the carbon closest to iodine, first becomes more negatively charged, before it charges up in positive direction. This is a clear indication of the early polarization of the pyridine ring in close vicinity to an iodine atom that is charging up on ultrafast timescales.

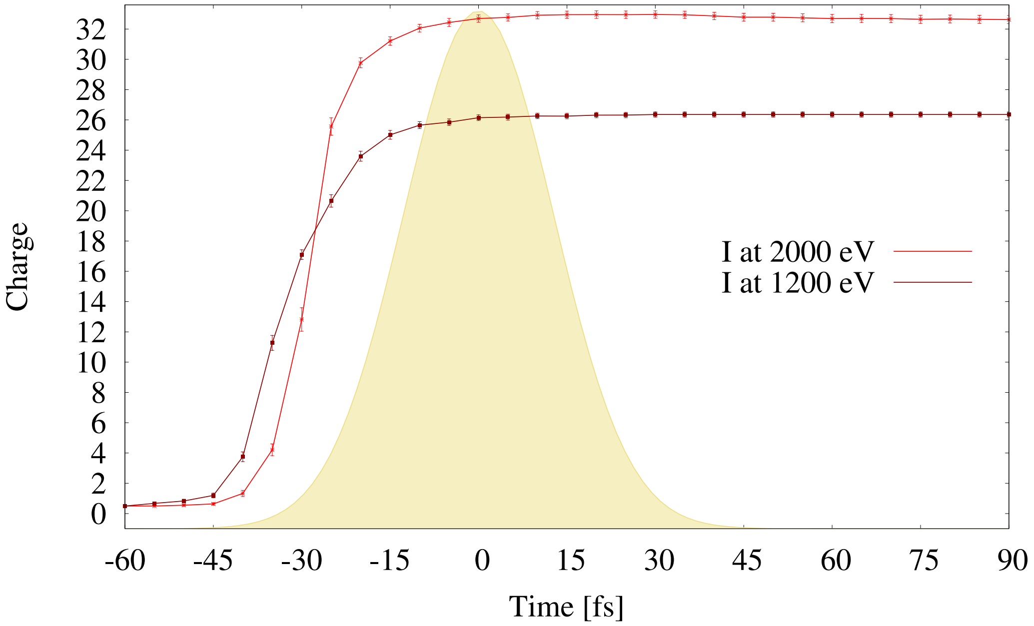

FIGURE 3.16: **Comparison of the time-dependent average Mulliken partial charges of iodine for the high-fluence case at both photon energies.** For comparison the iodine curves from Figs. 3.15(c) and 3.15(d) are plotted in one graph.

In Fig. 3.16 the two high-fluence iodine graphs from Figs. 3.15(c) and 3.15(d) are plotted together for comparison. Due to the higher photoionization cross sections the iodine charge increases earlier in the 1.2 keV case. At 28 fs before the pulse center, however, an intriguing intersection of the two curves is found. The reason is that at this point in time the average charges (∼+19) are close to the charge state (∼+21), for which we have likewise seen an intersection in the atomic total iodine photoionization cross sections in Section 3.3.1.

### 3.3.7 Reoptimization of molecular orbitals for every hole configuration

In the sequence of photoionization events, Auger and fluorescence decays, the molecular electronic structure is reoptimized for every new mutliple-hole electronic configuration, employing a variant of the maximum overlap method (MOM) [23, 70]. If the XMOLECULE SCF calculation fails to converge, the occupation number is smoothly adapted to the new electronic configuration in fractional steps of $\Delta f = 0.1$. If this procedures also fails to yield a converged solution, molecular orbitals optimized from the previous step are used that are occupied according to the new electronic configuration. The last case occurs in about 55 % of all ionization steps in the calculations for the combination of 2 keV and $1 \times 10^{11} \frac{\text{ph}}{\mu\text{m}^2}$, which induce a comparably low ionization degree. For all other parameter combinations with higher ionization degrees the algorithm finds no other than this solution in about 76 % of all ionization steps.

As detailed in Section 2.1.2, XMOLECULE uses the orbitals optimized for the previous electronic configuration, occupied with the new occupation pattern, as initial guess for the electronic structure of the new configuration, and in every SCF iteration the orbitals are occupied to achieve the maximum overlap between the occupied orbitals in the previous and current iterations. This approach relies on the assumption that the orbitals stay similar to each other. However, in consequence of an ionization step, the molecular electronic structure may as well change drastically, such that a low overlap value may sometimes erroneously prevent the algorithm from finding a solution. An illustrative example for this is given in Section 3.3 of Ref. [125], where a low overlap value of 0.25 between parent and final configurations of carbon monoxide prevents XMOLECULE from finding a converged solution for the final configuration if this parent configuration is used as an initial guess.

Motivated also by the SCF convergence problems that I encountered in this iodopyridine isomers project, a new fallback strategy has been developed by Michael Obermeyer and Dr. Ludger Inhester to resolve excited-state SCF convergence failures. [125, 126] It partially lifts the restrictions imposed by the MOM, thus allowing to find SCF solutions for excited states with increased flexibility. This new fallback strategy called “partial freezing" could resolve all six examined XMOLECULE SCF failure cases for CO, and yielded also promising preliminary results for phenol.

# Chapter 4

# XFEL-Induced Coulomb Explosion Imaging of Complex Single Molecules

Essential parts of this chapter are published as Ref. [127]. In Sections 4.1 and 4.2 of this chapter, first the experiment is described which our international collaboration carried out, with the main experimental collaborators being Dr. Rebecca Boll and Prof. Dr. Till Jahnke from European XFEL. I was also a part of the team that conducted the experiment. The remaining sections of this chapter, Sections 4.3 to 4.5, discuss in detail how I modeled this experiment by use of the toolkit XMDYN [58].

## 4.1 Experimental details

The experiment was performed during a beam time at the X-ray free-electron laser European XFEL in March 2019. It was carried out using a COLTRIMS reaction microscope [57] which is part of the Small Quantum Systems (SQS) scientific instrument at the European XFEL.

### 4.1.1 Information on the X-ray radiation source

Detailed information on the high-repetition-rate soft and hard X-ray free-electron laser European XFEL can be found in Ref. [11]. It is a young research facility, with the first experiments by user groups performed in September 2017.

European XFEL operates on the principle of **SASE** which means that coherent X-ray radiation is generated in a single passage of an electron beam through a very long undulator, i.e., a periodic lattice of alternating magnetic dipolar fields. In accordance with the principle in classical electromagnetism, that accelerated charged particles emit radiation, the electrons undulating through the periodic magnet array emit (X-ray) photons. [1] These photons interact back with the electrons, such that towards the end of the undulator, the electrons become bunched at the radiation wavelength, and thus radiate coherently. [1]

European XFEL stands out among the currently existing XFELs due to its superconducting linear accelerator which allows for the production of up to

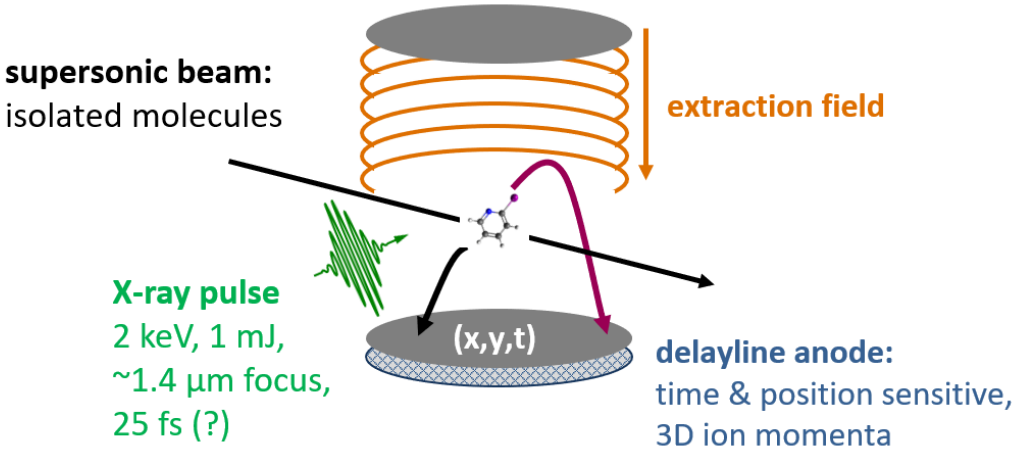

FIGURE 4.1: **Scheme of the experimental setup**. The focused X-ray beam intersects a supersonic gas jet containing the target molecules at right angle inside the reaction microscope. Ions are extracted by an electric field onto a time- and position-sensitive charged particle detector. From the time-of-flight information and the hit position the initial three-dimensional momentum vector of each ion can be calculated. Figure taken from Ref. [130].

27000 X-ray pulses per second (i.e., a **repetition rate** of 27000 Hz). [11, 128] In contrast, non-superconducting XFELs provide repetition rates of only 10-120 Hz. [21, 128] An augmented repetition rate opens up new areas of research by enabling the collection of sufficient data in short beam times also from systems which give very weak signals. [128]

### 4.1.2 Experimental setup

The experimental setup is shown schematically in Fig. 4.1. By expanding vapor of the target molecules through a nozzle into vacuum, using helium as carrier gas, a supersonic gas jet [129] was generated. In this way every X-ray pulse typically interacted with only a single molecule. Among the iodopyridine isomers only 2-iodopyridine ($C_5H_4IN$) was investigated, as its state of aggregation at room temperature (liquid) renders it easier to handle experimentally than the 3- and 4-iodopyridine isomers which are solid at room temperature. Besides, iodopyrazine ($C_4H_3IN_2$) was studied which is also liquid at room temperature and the heterocyclic compound related to 2-iodopyridine, but with two nitrogen atoms in the aromatic ring (see Figs. 4.3A and 4.3D on page 44 for structural formulae).

A photon energy of 2 keV was used, and the X-ray focus size was calculated to be 1.4 µm in diameter. The average pulse energy was 1 mJ (see Section 4.4 for conversion into fluence on target). Using the COLTRIMS reaction microscope [57], the three-dimensional (3D) momenta of the ionized fragments were measured in coincidence.

Figure 4.2 illustrates schematically the time structure of the XFEL pulses used in the experiment. The European XFEL provided ten electron bunch

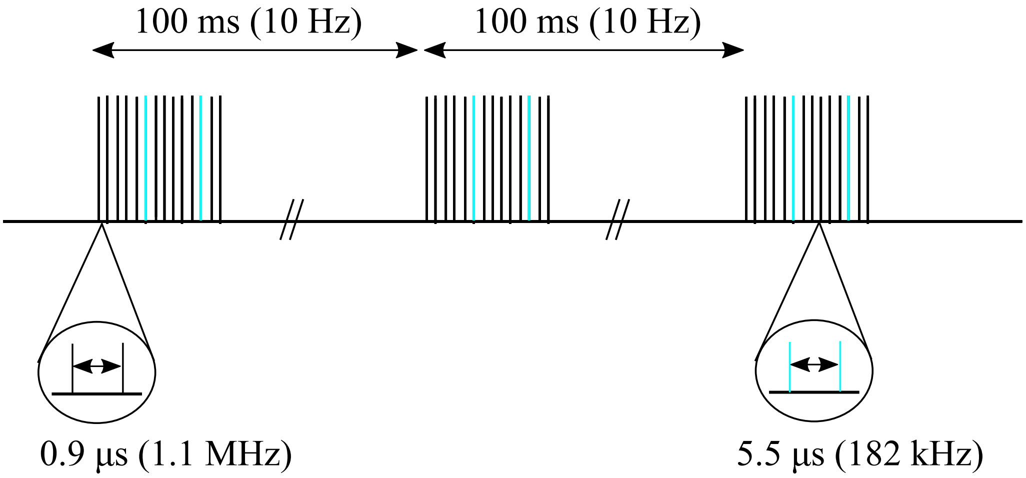

FIGURE 4.2: **Time structure of the European XFEL in the so-called burst mode**. Per second ten electron bunch trains were delivered with an inter-train repetition rate of 1.1 MHz. We used every sixth electron bunch to generate X-ray pulses for our experiment (indicated in blue), such that the photon pulses within one X-ray pulse train had a spacing of 5.5 μs.

trains per second (i.e., 10 Hz train repetition rate), with a spacing of 1.1 MHz between the electron bunches within one train. With this intra-train repetition rate we can thus confirm that the European XFEL is the first MHz repetition rate XFEL. [11, 128] In the lasing process of a SASE XFEL the individual femtosecond electron bunches generate X-ray pulses with femtosecond pulse durations. We used every sixth electron bunch for generating X-ray pulses for our experiment, as indicated in blue in the figure. Hence, the photon pulses in our experiment had a spacing of 5.5 μs, limited by the flight times of the heaviest fragments. Eventually, we received 250 – 570 X-ray pulses per second. From this we can conclude that every X-ray pulse train consisted of 25 to 57 X-ray pulses with a spacing of 5.5 μs, i.e., the X-ray pulse trains had a duration between 140 and 310 μs. In between the individual X-ray pulse trains, which had a spacing of 100 ms, there was thus between 99.7 and 99.9 ms idle time.

Based on the electron bunch charge of 250 pC in the accelerator, an upper limit of 25 fs was calculated for the X-ray pulse duration. For a more detailed discussion of the pulse duration, see Section 4.5.9.

## 4.2 Experimental results

Figure 4.3 shows the most important experimental results from the beam time. The 2-iodopyridine and iodopyrazine molecules were multiply ionized by the X-ray pulses and thus, all atoms were charged rapidly. As a consequence, the molecules underwent an explosion due to Coulomb repulsion of their constituents. In the figure the ion momenta are depicted which occurred after fragmentation of the molecules into $I^+$, $N^+$ and $H^+$ ions (Figs. 4.3B and 4.3E) as well as into $I^+$, $N^+$ and $C^+$ ions (Figs. 4.3C and 4.3F), respectively.

The coordinate frame is rotated in such a way that the $I^+$ momentum points along the $z$-axis, and spans the $(y, z)$ plane together with the $N^+$ momentum. The ion species are marked in different colors, as they can be identified by their different flight times in the spectrometer (which are determined by a particle's mass-over-charge ratio $m/q$).

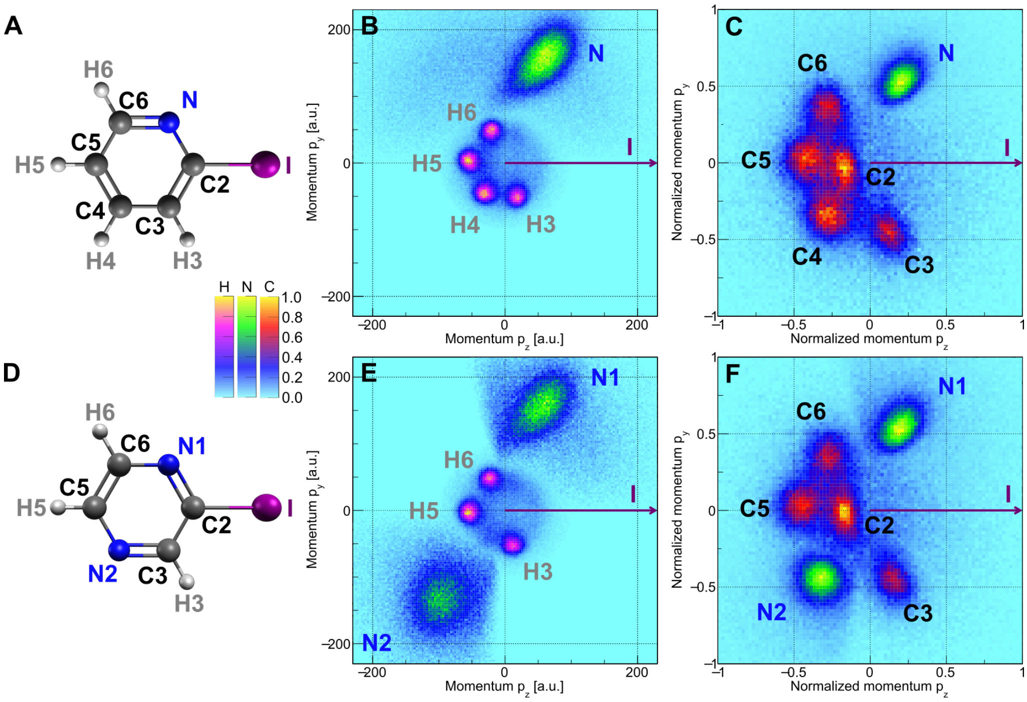

FIGURE 4.3: **Coulomb explosion imaging of 2-iodopyridine and iodopyrazine.** Newton plots of $N^+$ and $H^+$ ions (B) & (E), as well as $N^+$ and $C^+$ ions (C) & (F) show the experimentally measured momenta following Coulomb explosion of 2-iodopyridine (A)–(C) and iodopyrazine molecules (D)–(F). For all coincidences in which $I^+$, $N^+$, and at least one $H^+$ or $C^+$ ion were detected, the coordinate frame is rotated such that the $I^+$ momentum points along the $z$-axis ($p_{I_x} = p_{I_y} = 0$), and the $N^+$ momentum spans the $(y, z)$ plane together with the $I^+$ momentum ($p_{N_x} = 0, p_{N_y} > 0$). The momentum of the third particle is plotted in this coordinate frame. In (C) & (F) all ion momenta are additionally normalized such that the iodine momentum equals 1 ($p_{I_z} = 1$). No background was subtracted.

The structural analogies between the equilibrium molecular geometries (depicted in Figs. 4.3A and 4.3D) and the ion momentum distributions are so clear that one can easily assign distinct momentum regions to the individual atomic ions. Momentum images of this quality, with complex molecules of this size being completely imaged as atomic ions, are remarkable and as far as I am aware, unprecedented. The clarity is attributable to the fast charging of all ten or eleven atoms of the molecules within only a few femtoseconds (see also corresponding modeling results in Section 4.5.1), thus leading to a direct explosion without rotation or formation of intermediate molecular fragments. Underlying this is the key advantage of using an XFEL to trigger Coulomb explosions: it is feasible to create very high charge states within a few femtoseconds. This is very difficult to achieve with femtosecond optical lasers as in this case ionization occurs via tunnel ionization. The higher the molecular charge state is, the broader is the tunnel barrier that the remaining electrons have to tunnel through at the increased magnitude of their binding energy. Thus, for a given laser intensity the ionization probability decreases exponentially as a function of the charge state. And the currently available laser intensities are too low [52, 53] for their electric field to sufficiently distort (i.e., narrow) the tunnel barrier so that very high molecular charge states could be easily reached.

In Fig. 4.3 molecular fingerprints are obtained in the momentum distributions that provide direct insight into the fragmentation dynamics. The carbon atom C2, located closest to the iodine atom, receives only little overall momentum compared to the other carbon atoms because it is repelled by the other ions in the ring as well as by the heavy iodine ion, and the resulting repelling force vectors partially cancel each other. Moreover, the proton momenta in Figs. 4.3B and 4.3E are found to be unexpectedly small ($|p_H| \sim 55$ a. u.). In contrast, a simple point-charge Coulomb explosion model that instantaneously assigns a charge of $+1$ to each atom at its equilibrium position results in asymptotic proton momenta of $|p_H| \sim 110$ a. u. The lower proton momenta observed experimentally imply that the light protons are ejected before the molecule reaches its final ionization degree.

The Newton plots in Fig. 4.3 show coincidences between only three atomic ions (out of a set of four measured ions). If only a fraction of the generated fragments is detected in coincidence, this usually implies a reduction of information. For example, the handedness of individual chiral molecules cannot be determined with certainty anymore if one out of five atomic fragments is missing. [53]

The high repetition rate of the European XFEL (up to 570 Hz in this case) enabled also the recording of up to eight-fold ion coincidences. These produce images which look identical to the three- and four-fold ion coincidences, as displayed in Fig. 4.4 (Fig. 4.4A: coincident detection of $I^+ + N^+ + C^+$; Fig. 4.4B: $I^+ + N^+ + C^+ + H^+$; Fig. 4.4C: $I^+ + N^+ + C^+ + C^+ + C^+ + H^+$; Fig. 4.4D: $I^+ + N^+ + C^+ + C^+ + C^+ + H^+ + H^+ + H^+$). This reveals that, for the planar molecules under investigation, the reduced set of information from partial coincidences already captures the essence of the asymptotic momentum density distribution of the fully fragmented molecule. The sharp momentum distributions obtained for three-fold ion coincidences in Fig. 4.4A indicate that the entire fragmentation pathway is determined by selecting the final charges of only three atomic fragments.

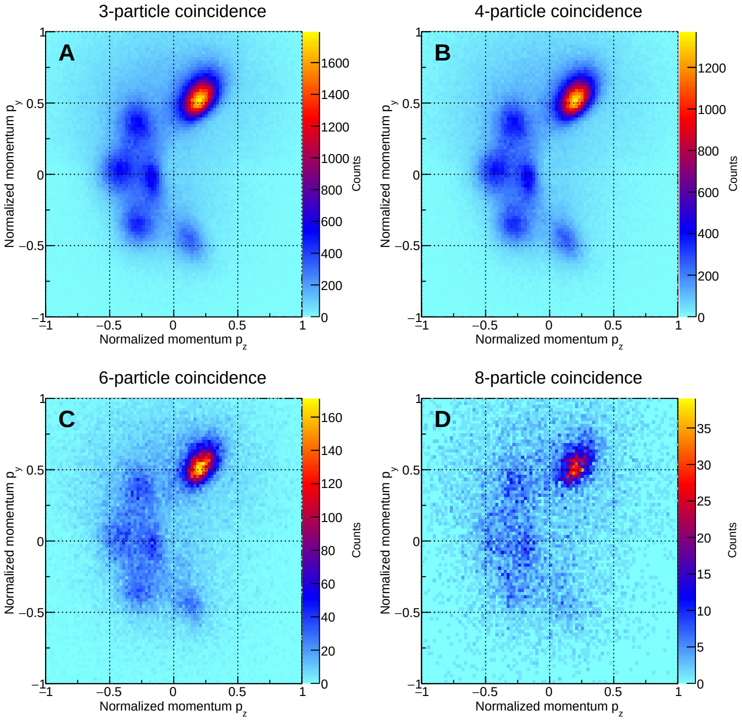

FIGURE 4.4: **Experimental $I^+ + N^+ + C^+$ Newton plots for (A) three-fold, (B) four-fold, (C) six-fold, and (D) eight-fold coincidence analysis.** The intensity of the nitrogen ion appears five times as high as compared to the carbon ions because, unlike in Fig. 4.3, in all cases, one nitrogen ion was detected and is plotted, while only one of the five different carbon ions is plotted (even in cases where more than one carbon ion was detected). The ion momenta are normalized such that the iodine momentum equals 1 ($p_{I_z} = 1$).

In Figs. 4.3B and 4.3E the hydrogen (H3-H6) signals are readily well localized in Newton plots displaying absolute momenta. The momenta of the individual carbon atoms (C2-C6) could likewise become clearly separated in Figs. 4.3C and 4.3F by normalizing the momenta to the magnitude of the momentum vector measured for the iodine ion originating from the same molecule (i.e., $\vec{p}_{norm} = \vec{p}/|\vec{p}_I|$). The impact of this normalization is illustrated by the difference between the first two pictures in the bottom row of Fig. 4.5.

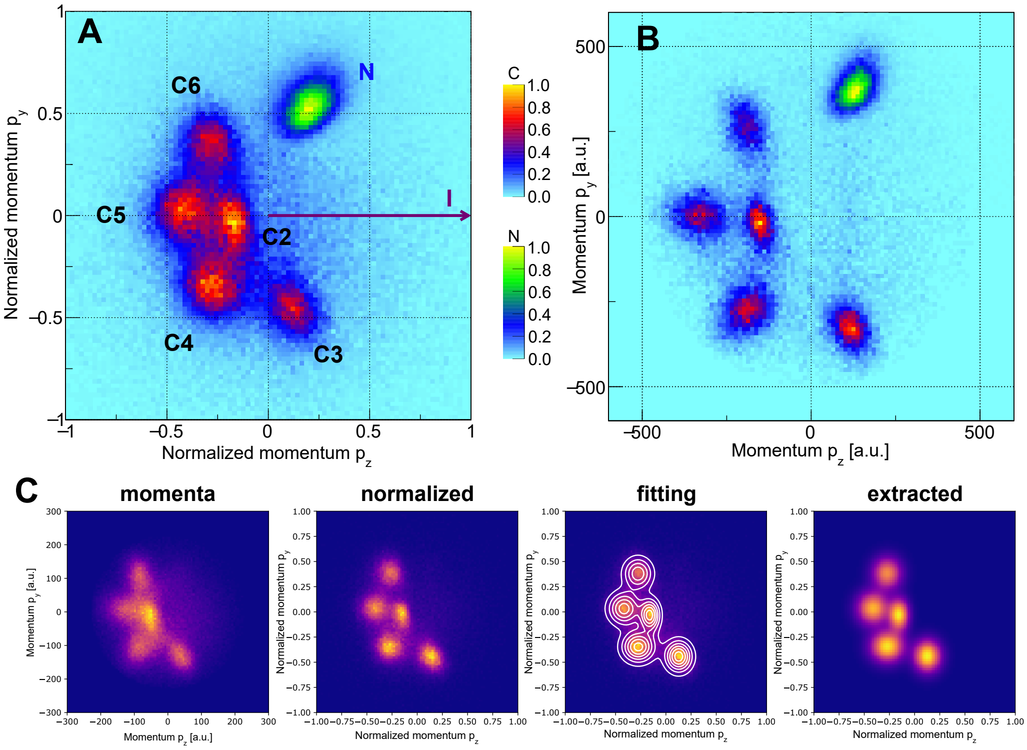

FIGURE 4.5: **Momentum-space normalization and extraction of site-specific charge abundances from experimental data.** (A) Normalized Newton plot for $I^{+}+N^{+}+C^{+}$ coincidences (identical to Fig. 4.3C). (B) Absolute molecular-frame momenta for $I^{4+}+N^{2+}+C^{2+}$ coincidences. (C) Visualization of the procedure for extracting site-specific charge abundances (repeated for every combination of charges to yield charge state distributions).

The normalization separates the momentum distributions of the individual ions, hence the final charge abundances of the individual atoms can be analyzed. Please also note that Newton plots for higher molecular charges provide clearly distinct carbon ion distributions even without normalization, as Fig. 4.5B shows for the $I^{4+}+N^{2+}+C^{2+}$ channel. A higher final charge implies a quicker charge-up and stronger repulsive forces, which separates the ion momenta in the Newton plots better.

For extracting site-specific charge state distributions, the procedure visualized in Fig. 4.5C is repeated for each carbon charge state from the three-fold coincidence data set consisting of a least one carbon, one nitrogen, and one iodine ion. For each carbon charge state a two-dimensional (2D) histogram of the normalized Newton plots is generated. A sum of five 2D-Gaussian distributions is fitted to each of these histograms, thus obtaining the relative abundances of the carbon atoms C1 to C5 for each charge state. The abundances of the different charge states are then normalized for every carbon atom and shown in Fig. 4.6 for three coincidence channels of 2-iodopyridine.

My calculations show that at the given photon energy of 2 keV, 91 % of all photoionization events occur at the iodine site (for more details see Section 4.5.8). The fact that aside from iodine ions also multiply charged carbon and nitrogen ions as well as protons are detected, indicates that ultrafast electron transfer from the aromatic ring to the the heavy absorber iodine takes place, as in the previous studies on iodine-containing compounds at high X-ray intensities [21, 22].

Although only one of the iodopyridine isomers from Chapter 3 could be examined experimentally, the result of the intramolecular electron rearrangement could be retrieved due to the ability to clearly distinguish between the signals of the individual carbon atoms in the momentum maps. This had not been expected, and renders the introduction of nitrogen as marker atom for the charge transfer at different positions in the aromatic ring superfluous.

Figures 4.6A to 4.6C show the experimental charge state distributions for all carbon atoms in the ring for different coincidence channels. Given are the abundances of the detected final charges of the carbon ions, i.e., the result of the intramolecular electron rearrangement after X-ray multiphoton ionization and fragmentation of the molecules. For higher iodine charges also the average carbon charge is shifted to higher values. For the $I^{+}+N^{+}$ coincidence (Fig. 4.6A) the relative abundance of the charge states $+1$ and $+2$ is the same for all carbon atoms, independent of the position in the ring. As opposed to this, for higher molecular charges (Figs. 4.6B, 4.6C) the C2 atom (red bar) is more often singly charged and less often triply charged than the other carbon atoms. Intuitively one might have expected the contrary – that the C2 atom receives the highest and not the lowest average charge. Considering that it is located closest to the source of charge (the iodine), and stays, unlike the other atoms, within close vicinity to the iodine for several tens of femtoseconds (see modeling results in Section 4.5.1), and that the electron transfer probability is strongly augmented by a shorter internuclear distance. [34] The observed trend in the charge state distributions, however, shows that these effects are overcompensated by the rapid rearrangement of the ring atom electrons on timescales much faster than the nuclear motion, adapting to the momentary molecular geometry. Due to Coulomb repulsion with the highly charged iodine, the positive partial charge locates preferentially furthest apart. The electron density is pulled towards the attractive potential of the iodine, leading to the lower charge on the C2 atom. Such behavior was suggested in previous studies [22, 131].

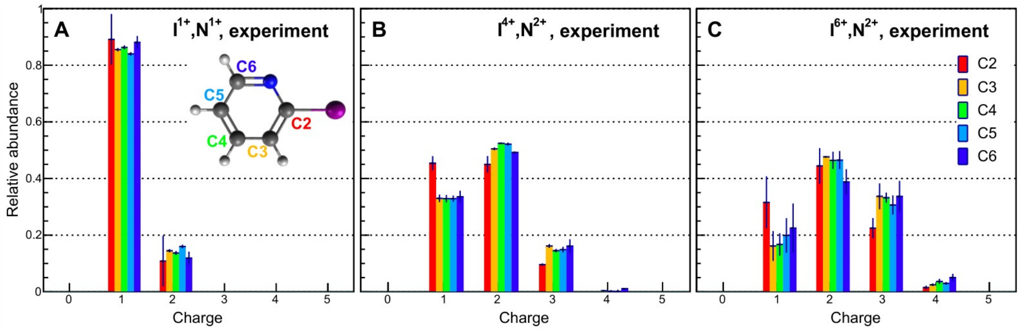

FIGURE 4.6: **Experimental charge state distributions of carbon atoms,** for three coincidence channels of 2-iodopyridine. The ion yields are obtained by fitting a 2D Gaussian to each peak in the respective normalized Newton plots (see Fig. 4.5). The error bars represent an estimate of the systematic error introduced in the fitting. Please note that the experiment is not sensitive to neutral fragments.

## 4.3 Choice of computational method

Aside from the intramolecular electron rearrangement part, the experiment yielded promising results regarding imaging purposes, as complex molecules could be imaged as atomic ions in their entirety, and with unexpected quality. Since modeling a Coulomb explosion imaging experiment involves analyzing the asymptotic fragment momenta (and not solely the final charge states of a highly ionized molecule), XMOLECULE [23] calculations with fixed nuclei as in Chapter 3 are clearly not suited. And the computational cost of XMOLECULE calculations with nuclear dynamics is prohibitive for larger systems such as iodobenzene and 2-iodopyridine. [21, 22, 132]

As explained in Section 4.2, a simple point-charge Coulomb explosion model that propagates the particles classically, employing an instantaneous assignment of a charge of $+1$ to all atoms at their equilibrium position, overestimates the experimentally measured proton momenta considerably. In fact, it is common to assume that Coulomb explosion does not take place at the internuclear distances of the neutral molecule, but rather at elongated distances, which reduces the available energy as well as the asymptotic fragment momenta. [133] In order to extract all information from the experimentally measured momenta, more advanced theoretical modeling is thus required which can describe the X-ray induced ionization as well as the associated atomic motion during the ionization dynamics.

An investigation [132] conducted by the summer student Natasha Feinstein revealed that the toolkit XMDYN [58] with charge transfer produces results for iodomethane $CH_3I$ similar to those obtained with XMOLECULE, but with a computational cost reduced by at least an order of magnitude. Figure 4.7 shows that for 8.3 keV photon energy a good agreement between the XMDYN and the XMOLECULE results is found for fluences above $4 \times 10^{12}$ photons/μm$^2$. In other words, for these pulse parameters XMDYN with charge transfer via the classical over-the-barrier model can describe the molecular ionization enhancement at high X-ray intensities. This is interesting insofar as in the XMOLECULE calculations the electron migration towards the iodine finds expression in a shifting of the molecular orbitals towards the iodine, while in the XMDYN calculations no molecular orbitals are present but only atomic orbitals, and a rapid ongoing movement of electrons between the atoms takes place before the critical distances for charge transfer are reached. [132] For the lower fluences, however, XMDYN underestimates the phenomenon of CREXIM [21] (see Fig. 4.7a). Please bear in mind at this point that we learned in Chapter 3 that fluence-dependent behavior cannot be directly transferred when going from 8.3 keV photon energy to 2.0 keV photon energy.

Building on this investigation [132], I examined if XMDYN can be used to model the XFEL-induced CEI of 2-iodopyridine and iodopyrazine as well as the intramolecular electron rearrangement at a practicable computational cost. See the subsequent sections for the results.

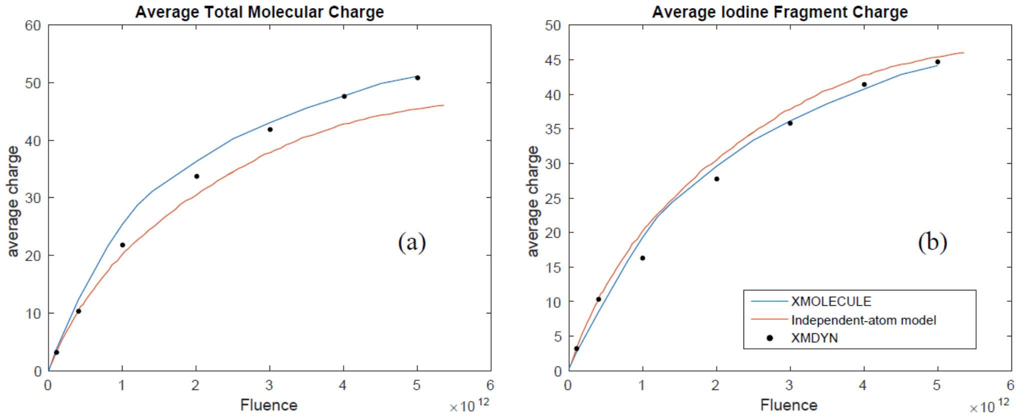

FIGURE 4.7: **XMOLECULE, XMDYN and independent-atom results from XATOM for average charge states computed for the entire molecule $CH_3I$ (a), as well as for the iodine fragment (b).** X-ray pulse parameters are the same as in Ref. [21], i.e., 30 fs FWHM, 8.3 keV photon energy, and the fluences ranging from 0 to 5 $\times$ $10^{12}$ photons/µm$^2$. Figure taken from Ref. [132].

An alternative (which I did not test) would have been to use the simplified Coulomb explosion model from Appendix C of Ref. [22]. There the positions of the atoms constituting iodobenzene are propagated classically with Coulomb forces taken from the time-dependent atomic partial charges in XMOLECULE calculations with fixed nuclei. This approach yielded for the average C-I bond distance in $CH_3I$ good agreement with the full ionization and nuclear dynamics calculation (see Fig. 6 in Ref. [22]). For the present CEI problem, apart from the error of using fixed-nuclei calculations, this approach would be challenged by the convergence problems encountered in

Chapter 3 for the iodopyridine isomers. The task would then be to find a fluence for which a sufficient number of trajectories contain final (Mulliken) partial charges that meet rounded to integers the respective coincidence condition under consideration. As a trial, I calculated 50 XMOLECULE trajectories with fixed nuclei for the same pulse parameters I employed for obtaining the $I^{+}$+$N^{+}$ coincidence trajectories with XMDYN (i.e., 2 keV, 10 fs FWHM and $7.5 \times 10^{10}$ photons/µm$^2$). Among these 50 trajectories, I did not find a single trajectory meeting the criterion of rounded final partial charges $I^{+}$+$N^{+}$.

Given that many more XMDYN trajectories had to be run than could be used (see Table 4.1), and that one XMOLECULE trajectory with fixed nuclei alone would take ~5 days, without the classical propagation of the atoms, compared to 5 min for one XMDYN realization, this approach would implicate a tremendously augmented computational cost. Nevertheless, it would be interesting to see the impact of the presence of molecular orbitals on the charge state distributions, as well as on the absolute ion momenta. Therefore, this approach could be worthy of being considered for future studies, especially if the convergence problems can be mitigated. In particular, since the latter would also reduce the computation time.

## 4.4 Calculation setup and simulation parameters

The 2-iodopyridine and iodopyrazine molecules are initially in their neutral equilibrium geometries which were obtained using GAMESS [119] at the RHF theory level with a 3-21G* basis set. This method-basis combination results in a structure for 2-iodopyridine which is in reasonably good agreement with experimental values. [120] In the XMDYN calculations all atomic orbitals which are occupied in the neutral ground state of the atoms are incorporated. The atoms can exchange electrons[1] based on the classical over-the-barrier model described in Section 2.4.1, and particles carrying a charge interact via Coulomb forces.

---

[1] In case the atoms or atomic ions have a different charge.

```
######################## XMDYN input file ##########################################

### X-ray pulse parameters
EPH             2000                # photon energy [eV]
NPH             7.5e+10             # fluence [(number of photons)/(micrometre^2)]
T               10e-15              # pulse duration [s]
T0              20e-15              # center of beam in time [s]
BEAM            gauss               # temporal pulse profile: step or gaussian

### Propagation, snapshots
DT              1e-18               # time step [s]
STEPS           1000000             # number of time steps
SNP             0:1000000:          # saving snapshots
PROGRESS        10                  # progress logging

### Phenomenae on/off (y/n)
ts               y                  # MD-block on/off
ph               y                  # photoionization on/off
fl               y                  # fluorescent decay on/off
au               y                  # Auger decay on/off
elsc             n                  # elastic scattering on/off
si               n                  # secondary ionization on/off
ir               n                  # recombination on/off
ph_aniz          y                  # photoelectron anisotropy on/off
ch_mgr           E-notconserved     # charge migration on/off

### MD integration method and its parameters
INT_METHOD       verlet             # verlet or subverlet2 or RK4

RANDSEED         9000000105         # random seed

XATOM_INACTIVE_ORBITS     53:4f     #iodine 4f orbitals not incorporated

### How binding energy is calculated based on XATOM data
XATOM_E          mixed              # XATOM_E mixed or table
```

FIGURE 4.8: **Typical XMDYN input file, displaying the most important simulation parameters.** Inspired by Ref. [58].

Figure 4.8 displays the simulation parameters employed for generating the theory results shown in Fig. 4.3. A photon energy of 2 keV was used in all calculations, as in the experiment. For propagating the positions of atoms and electrons in time, I applied the velocity Verlet algorithm with 1 million 1-attosecond time steps, i.e., the Monte Carlo trajectories were propagated up to 1 ps. X-ray pulses with a temporal Gaussian pulse envelope of 10 fs FWHM were assumed everywhere, except for Section 4.5.9 on the pulse duration dependence, where results for 20 fs FWHM are additionally shown. The positions of the classical particles were propagated using the molecular dynamics technique (“MD-block on”). Photoionization as well as fluorescent and Auger decay events were taken into account. As in Ref. [132], secondary ionization (electron impact ionization) and recombination between ions and free electrons into deep shells were excluded since they were expected unlikely to occur in a system of one small molecule, but rather in a plasma [134], i.e., in the fourth state of matter of an electrically conductive, ionized gas. Classical recombination between ions and free electrons (i.e., into high-lying Rydberg states) identified during postprocessing could, however, take place with these settings (and did take place, see Section 4.5.7).

Charge transfer between atoms and atomic ions was allowed, with the option “E-notconserved” specifying that no more sudden kinetic energy transfer to the ion cores was performed in order to strictly enforce energy conservation in electron transfer events (see Section 4.5.5).

Bonds between the atoms in the molecules are not taken into account (please refer to Section 4.5.6 for a discussion). Each trajectory is given a random seed (option "RANDSEED") as unique identifier, i.e., a number used to initialize a pseudo-random number generator. By this means, the same sequence of numbers, or in other words, a trajectory, can be reproduced by specifying the same initial random seed.

The option "XATOM_E" specifies how exactly the kinetic energies of the ejected photoelectrons $E_{\text{kin, photoel.}}$ and Auger electrons $E_{\text{kin, Auger el.}}$ are calculated in XATOM-related events by XMDYN. In general, they are given as

$$E_{\text{kin, photoel.}} = \mathrm{h}\nu - IP_{\text{photoel.}} \tag{4.1}$$

$$E_{\text{kin, Auger el.}} = \Delta E - IP_{\text{Auger el.}} \tag{4.2}$$

where h$\nu$ is the photon energy of the ionizing light. $\Delta E$ denotes the energy difference between the orbital with the core hole and the orbital from which the electron replenishes the core hole. $IP_{\text{photoel.}}$ and $IP_{\text{Auger el.}}$ are the ionization potentials of the photo- and Auger electrons, respectively.

The first possible setting is "XATOM_E table", which means that transition energies for generating electron kinetic energies are calculated using Koopmans' theorem, i.e., based on the energy differences between the orbitals involved in the transition, optimized for the inital electronic configuration (see Section 2.1.3 for details). The second possible setting is "XATOM_E total_E", which means that the transition energies for generating electron kinetic energies are taken as the difference between the total energies of the final and initial states. This approach is known as ΔSCF, and represents an alternative to Koopmans' theorem for calculating ionization potentials on the level of the HF approximation which takes into account orbital relaxation [135]. This approach is usually quite accurate, provided that the excited state is reasonably well described by the single-determinant approximation employed in HF theory. [136] For generating the results presented in this thesis in Section 4.5, the third possible setting "XATOM_E mixed" was used. In earlier XMDYN studies on $C_{60}$ [60, 114, 115] photoelectron energies obtained with "XATOM_E table" were in better agreement with experimental values, while for the Auger electron energies values from "XATOM_E total_E" were better. This is combined by "XATOM_E mixed", i.e., photoelectron energies are taken from "table" and Auger electron energies from "total_E". Energies of emitted fluorescent X-ray photons $h\nu_{\text{fluor. ph.}} = \Delta E$ are not relevant here. (For the sake of completeness, they are calculated with "table" values, if "XATOM_E mixed" is specified.)

Please note that in XATOM Koopmans' theorem is always applied. Using ΔSCF would require two calculations for both the intial and final state. For a given inital state, XATOM would have to go through all available final states to evaluate transition energies, which are required for calculating transition rates and cross sections, although it is not yet decided which final state will be chosen in the Monte Carlo scheme. This would create too much computational overhead for calculating rates and cross sections. When using Koopmans' theorem, only the orbital energies of the inital state are required.

Calculating Auger and / or photoelectron kinetic energies in XMDYN based on the ΔSCF procedure does not reduce computational efficiency because it is not required to pre-calculate the total energies for the final configurations of all possible processes of a given atomic configuration. Only the rates from XATOM are needed, and if an event occurs based on the rates, the transition energy is needed. Then XATOM is called to obtain a value for the total energy of the chosen final configuration. Since anyhow a calculation for the final state is required, e.g., to obtain rates for transitions (using Koopmans' theorem) which in turn start from this configuration, choosing "XATOM_E mixed" or "XATOM_E total_E'" in XMDYN does not reduce computational efficiency.

Unless specified otherwise, a fluence of $7.5 \times 10^{10}$ photons/µm$^2$ was employed, optimized to result in a high fraction of $I^+$+$N^+$ coincidences. For Figs. 4.12 and 4.17, fluences were chosen such as to yield the highest percentage of the respective coincidence. I did not find a fluence leading to more than 1 % $I^{6+}$+$N^{2+}$. As a consequence of the highly selective nature of the presented reaction-microscope data, I had to run many more Monte Carlo realizations than I could use. Table 4.1 indicates how many trajectories had to be calculated in order to obtain in Fig. 4.12 a sufficiently small statistical error (normalized square root of the number of trajectories with the carbon atom in the respective final charge state).

TABLE 4.1: **Fluences and numbers of XMDYN Monte Carlo trajectories underlying Fig. 4.12 and Fig. 4.17, for all three coincidence channels**. Given are the sum of all trajectories calculated as well as the number of trajectories meeting the coincidence criterion (coinc. traj.), and the corresponding fraction.

| figure | coinc. | fluence [ph/µm$^2$] | coinc. traj. | sum of all traj. | fraction |
|---|---|---|---|---|---|
| 4.12D & 4.17G | $I^+$+$N^+$ | $7.5 \times 10^{10}$ | 2212 | 15000 | 15 % |
| 4.12E & 4.17H | $I^{4+}$+$N^{2+}$ | $1.8 \times 10^{11}$ | 1429 | 30000 | 5 % |
| 4.12F & 4.17I | $I^{6+}$+$N^{2+}$ | $2.3 \times 10^{11}$ | 459 | 45000 | 1 % |
| 4.17D | $I^+$+$N^+$ | $7.5 \times 10^{10}$ | 4560 | 15000 | 30 % |
| 4.17E | $I^{4+}$+$N^{2+}$ | $1.8 \times 10^{11}$ | 8385 | 75000 | 11 % |
| 4.17F | $I^{6+}$+$N^{2+}$ | $2.3 \times 10^{11}$ | 335 | 45000 | 1 % |

In the experiment a maximum X-ray pulse energy $E$ of 1 mJ was measured on average upstream of the beamline mirrors by a gas monitor detector. At a photon energy of 2 keV, a beamline transmission $T$ of 80 % was measured, resulting in 0.8 mJ on target. The diameter of the X-ray focus was calculated to be 1.4 µm, which can be used to calculate the focal area $A$.

Inserting these values, a conversion into average peak fluence $\mathcal{F}_{\text{peak}}$ on target can be performed [100]

$$\mathcal{F}_{\text{peak}}\left[\frac{\text{Joule}}{\mu\text{m}^2}\right] = \frac{4\ln(2)}{\pi} \times \frac{E}{A} \times T \tag{4.3}$$

$$= \frac{4\ln(2)}{\pi} \times \frac{1\times 10^{-3}\text{J}}{(1.4\,\mu\text{m})^2} \times 0.8 \tag{4.4}$$

$$= 3.6 \times 10^{-4}\,\frac{\text{J}}{\mu\text{m}^2} \tag{4.5}$$

The factor $\frac{4\ln(2)}{\pi}$ arises from assuming a Gaussian focal shape. [100] Each photon possesses an energy of $2\,\text{keV} \mathrel{\widehat{=}} 3.2 \times 10^{-16}\,\text{J}$. Using this, the fluence in photons per $\mu\text{m}^2$ can be calculated

$$\mathcal{F}_{\text{peak}}\left[\frac{\text{ph}}{\mu\text{m}^2}\right] = \frac{4.1\times 10^{-4}\,\frac{\text{J}}{\mu\text{m}^2}}{3.2\times 10^{-16}\,\frac{\text{J}}{\text{ph}}} = 1.1 \times 10^{12}\,\frac{\text{ph}}{\mu\text{m}^2} \tag{4.6}$$

This value for the experimental peak fluence is higher than the fluences I assumed, which ranged between $7.5 \times 10^{10}$ photons/$\mu\text{m}^2$ and $2.3 \times 10^{11}$ photons/$\mu\text{m}^2$. Extended Data Figure 6 in Ref. [21] shows exemplarily that typically lower fluence values contribute more to the experimental fluence distribution function obtained from calibration with argon atoms. Please refer to Section 2.1.4 for a discussion about the assumption of a spatially constant fluence value in the calculations.

## 4.5 Theory results and discussion

### 4.5.1 $\text{I}^+ + \text{N}^+$ coincidence channel

The calculated Newton plots obtained with XMDYN [58] are shown in Figs. 4.9C, 4.9E, 4.9H and 4.9J. All momenta shown are absolute values, in order to provide a straightforward comparison between experiment and theory. The overall agreement of the XMDYN with the experimental results is remarkable, in particular considering that, for computational efficiency, no molecular orbitals or chemical bonds are included in the modeling. In comparison to the simple point-charge Coulomb explosion model depicted by the black markers, a clear improvement is achieved with XMDYN. The reason is that XMDYN can describe the atomic motion during the charge-up, while the simple model instaneously assigns a charge of $+1$ to each atom at its equilibrium position.

The demonstrated ability to reproduce experimental ion momenta by inserting a known equilibrium molecular geometry into the model represents a first important step towards future structural inversions of experimental XFEL-CEI data.

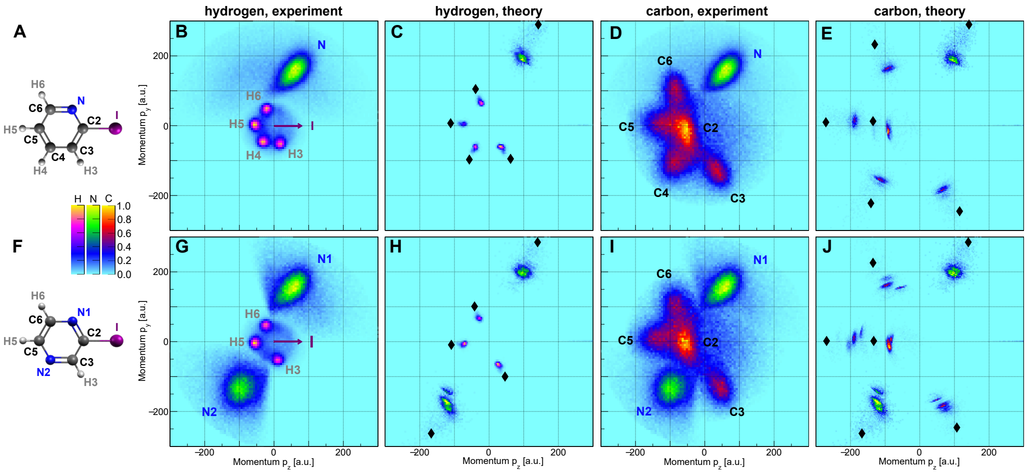

FIGURE 4.9: **Coulomb explosion imaging of 2-iodopyridine and iodopyrazine, in experiment and theory.** Newton plots of $N^+$ and $H^+$ ions (B) & (G), as well as $N^+$ and $C^+$ ions (D) & (I) display the measured absolute momenta following Coulomb explosion of 2-iodopyridine ($C_5H_4IN$), (A) and iodopyrazine ($C_4H_3IN_2$) molecules (F). For all cases in which $I^+$, $N^+$, and at least one $H^+$ and one $C^+$ ion were detected, the coordinate frame is rotated such that the $I^+$ momentum points along the $z$-axis ($p_{I_x} = p_{I_y} = 0$), and the $N^+$ momentum spans the $(y, z)$ plane together with the $I^+$ momentum ($p_{N_x} = 0$, $p_{N_y} > 0$). The momentum of the third particle is plotted in this coordinate frame. No background was subtracted. The corresponding modeling results from XMDYN are given in panels (C), (E), (H) and (J), respectively. The diamond-shaped markers depict the asymptotic fragment momenta when a single positive charge is applied to each atom instantaneously.

In order to obtain the results in Fig. 4.9, the model was further developed (see Section 4.5.5). I ascribe the remaining discrepancies between the experimental and theoretical Newton plots predominantly to residual chemical bonding (see Section 4.5.6). This can presumably be overcome by adding a force field in the model. An iterative optimization scheme could then compare calculated and experimentally measured momenta, thus identifying the start geometry that leads to the best match. Using such a procedure, the molecular structure of $D_2O$ was reconstructed with an accuracy of 0.3 Å for the bond length and 15 ° for the bond angle, inverting the Coulomb explosion induced by a femtosecond optical laser. [40]

Against this background, considering the ease with which XFELs can create very high molecular charge states within a few femtoseconds, as well as the computationally efficient design of XMDYN which allows the modeling of large biomolecules [137], structure reconstruction also of larger molecules comes closer to reach. Machine learning methods can assist in solving such an inverse problem where one seeks to reconstruct parameters of a system from indirect observations. [138]

In addition, please note that CEI can also succeed in determining unknown structures by comparing Coulomb explosion results in momentum space to the ones of related known structures (see the paragraph on $C_3^+$ in Ref. [46]), and that modeling can provide support in this regard.

The good agreement in Fig. 4.9 permits the addition of time-resolved information to the study – which was experimentally not accessible, as no suitable pump laser was available for performing a pump-probe experiment. The modeling provides access to the structural dynamics occurring on femtosecond timescales. Figures 4.10A and 4.10B display snapshots of the distributions of ion momenta and positions during and after the X-ray pulse[2]. Figures 4.10C and 4.10D show the average interatomic distances and the average atomic charges as a function of time.

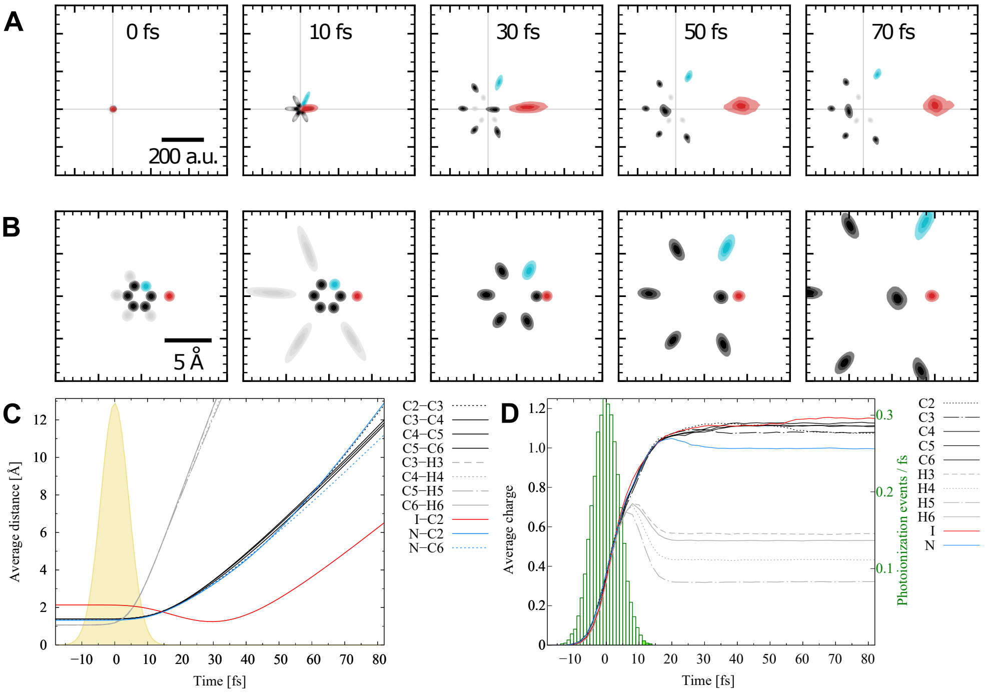

FIGURE 4.10: **Time-dependent geometry and charge evolution of 2-iodopyridine molecules,** created from XMDYN trajectories resulting in $I^+$ and $N^+$ ions. Snapshots of the distributions of ion momenta (A) and ion positions (B) are displayed at different times (red: $I^+$, blue: $N^+$, black: $C^+$, grey: $H^+$). The origin of the coordinate frame is the molecular center-of-mass, the horizontal axis points along the I equilibrium position, and the plane of the figure is spanned by the I and N equilibrium positions such that N points upwards. Grey gridlines indicate $p_x = p_z = 0$. Average interatomic distances and charges are shown in (C) and (D), respectively. The yellow area in (C) indicates the assumed X-ray pulse shape, a Gaussian of 10 fs FWHM (see Section 4.5.9 for 20 fs results). In (D) the average number of absorbed photons per molecule and fs is shown in green.

---

[2] They are taken from the corresponding videos that Benoît Richard created from my 2-iodopyridine data.

The positions of the hydrogens evolve as the earliest among all atoms (see second snapshot of Fig. 4.10B and Fig. 4.10C), already considerably during the assumed X-ray pulse of 10 fs FWHM. The average C-H distance almost duplicates within the first 5 fs after the pulse center, confirming the rapid proton ejection suspected in Section 4.2. The early proton emission can be explained with the molecular geometry. The hydrogens have only one bonding partner at a comparably short distance (i.e., strong repulsive force); and a C-H bond is weaker than an aromatic C-C bond which every ring atom possesses twofold[3]. Furthermore, the protons have a large charge-to-mass ratio, i.e., they are accelerated rapidly via $a = \frac{F}{m}$. The repulsive force evoked by the protons initially keeps the ring structure intact. Such a rapid proton ejection was also predicted for hydride clusters. [139]

The heavier fragments start moving significantly only after the X-ray pulse is over. The C-C and C-N distances elongate as expected, but for the I-C2 distance a minimum after 30 fs is found. This intriguing behavior is caused by the force vector acting on C2 which is initially directed towards the iodine, until the ring has undergone Coulomb explosion and the repulsion by the iodine dominates. As a result, the C2 atom turns into the other direction, moving away from the iodine. The I and C2 atoms come on average as close as 1.24 Å. On a side note, in view of the iodine atomic radius of 1.40 Å [140] the monopole approximation becomes definitely questionable here (applied in the implementation of the over-the-barrier model, see Section 2.4.1). For channels with higher total charge, an I-C2 distance minimum is observed as well, for example for the $I^{4+}$ + $N^{2+}$ coincidence, where it is reached already after 13 fs (see Section 4.5.4).

In Appendix C of the iodobenzene study [22] the I-C distance evolution was compared with the one observed for $CH_3I$. For consistency the carbon atom next to iodine in iodobenzene will be called C2 in the following. It was similarly found that for a given fluence of $5 \times 10^{12}$ photons/µm$^2$, due to the repelling force evoked by the charges on the other carbon atoms, which is directed towards the iodine, the distance between the iodine and the C2 atom evolves more slowly than in $CH_3I$. Furthermore, the slower I-C2 distance evolution was attributed to the effective distribution of the charge within the benzene ring, such that the individual atom feels a considerably lower Coulomb force. However, a motion of the C2 atom towards the iodine, followed by a turnaround, is not found for iodobenzene, not even for the lower considered fluence of $4 \times 10^{11}$ photons/µm$^2$ with an iodine final charge of $+6$. In the latter case this is also due to the fact that Hao *et al.* [22] propagate the atomic positions classically based on the time-dependent partial charges from the XMOLECULE [23] calculations with fixed nuclei, and ignore negativ partial charges. In this approach, the C2 atom receives a partial charge slightly above 0.0 and thus experiences Coulomb repulsion only long after the other carbon atoms, such as the one located opposite of C2, became charged and moved apart.

---

[3] Please note that argumentation with bond strengths refers to the low proton momentum observed experimentally, as in the modeling no chemical bonds are incorporated.

In Fig. 4.10D, all average charges first rise simultaneously, until the I, C, and N charges reach a plateau after 20 fs. This confirms the fast charging of all atoms that was suspected behind the clarity in the experimental momentum images in Section 4.2. The average hydrogen charges stand out due to a maximum after 10 fs. The maximum is caused by the respective barriers in the model, which allow between 10 fs and 14 fs for electron transfer only from C to $H^+$, but not from H to $C^+$ (see Section 4.5.2).

When comparing Figs. 4.10C and 4.10D, it is interesting to note that the charges on the atoms rise markedly before they start to move. This is a hint that the inertial delay (discussed in Ref. [18]) in the conversion of potential energy into kinetic energy is observed in the modeling with XMDYN, even without accounting for chemical bonds.

The final charge states are determined by the late-time charge evolution (see Section 4.5.7), and the calculated average total molecular charge is $+9$ for fragmentation of 2-iodopyridine into $I^+$ and $N^+$ ions.

### 4.5.2 Potential barriers explaining the hydrogen charge maximum

The striking maximum in the hydrogen charge evolution curves in Fig. 4.10D can be understood by regarding how the charge redistribution is accounted for in the simulations. Figure 4.11 displays the potential barriers at three points in time between carbon and hydrogen for the case where one of the atoms carries a charge of $+1$ and the other one is neutral. The depicted potential is composed of a charge of $+1$ on both atomic sites because the electron on the neutral atom which is considered for charge transfer to the other atom does not feel its own shielding of the nuclear charge. Please refer to Section 2.4.1 for a detailed description of the over-the-barrier model. As an illustration of the mechanisms in the over-the-barrier model, the shown snapshots were generated using the average C3–H3 distance at 0 fs, 10 fs, and 14 fs, with the relation between time and distance taken from Fig. 4.10C. At 0 fs (A), the atoms are still close together and there is no potential barrier between them, therefore the electrons can be transferred in both directions. At the same time, the average hydrogen charges in Fig. 4.10D rise, reflecting the overall strong ionization dynamics when the pulse is most intense at 0 fs. At 10 fs (B), the top of the potential barrier reaches the energy level of H ($1s$), such that electron transfer in the direction from H to $C^+$ is no longer possible. However, in the direction from C to $H^+$ electron transfer is still possible until 14 fs, as the top of the potential barrier only equals the C ($2p$) energy level after the C and H atoms moved further apart from each other. Consequently, for the time between 10 fs and 14 fs, electron transfer between C and H is only possible in the direction $[C,H^+] \rightarrow [C^+,H]$, thus leading to a decrease of the average hydrogen charges in this time interval in Fig. 4.10D. At 14 fs after the pulse center (C), the potential barrier top exceeds both energy levels and the average hydrogen charges reach a plateau.

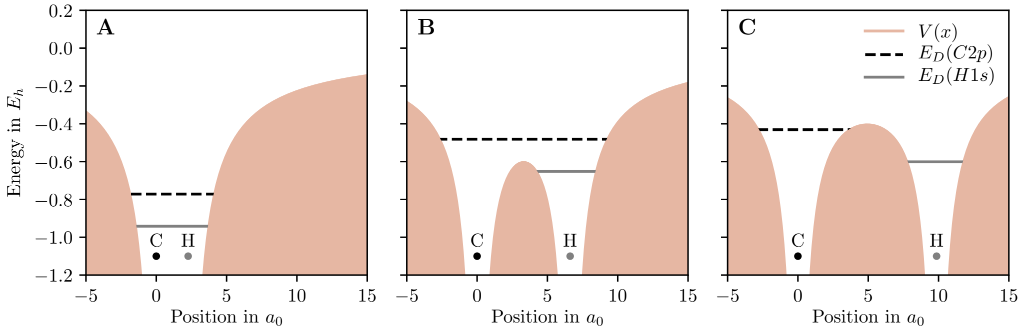

FIGURE 4.11: **Potential barriers between C and H at 0 fs (A), 10 fs (B), and 14 fs (C)**. The potential $V(x)$ is calculated as $V(x) = -\frac{1}{|x|} - \frac{1}{|x-R|}$, where $R$ is the momentary average C3–H3 distance at the respective point in time taken from Fig. 4.10C. Filled areas indicate forbidden regions, as no quantum tunneling is incorporated in the model. The donor energy levels $E_D(\mathrm{C}\,2p)$ and $E_D(\mathrm{H}\,1s)$ are computed based on the atomic orbital energies, influenced by the electrostatic interaction with the other ion, using Eq. (2.23) in Section 2.4.1.[4]

---

[4] Figure content from me, layout slightly altered by Benoît Richard.

### 4.5.3 Charge state distributions of carbon atoms

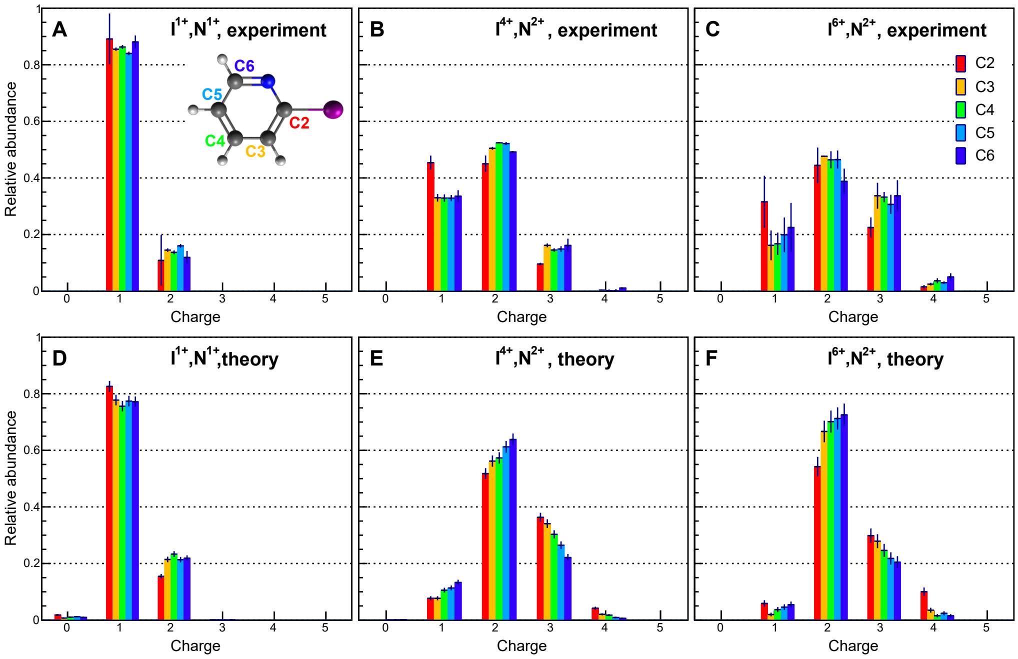

FIGURE 4.12: **Charge state distributions of carbon atoms in experiment and theory,** for three coincidence channels of 2-iodopyridine. The experimental ion yields (A)–(C) are obtained by fitting a 2D Gaussian to every peak in the respective Newton plots (see Fig. 4.5). The experimental error bars are an estimate of the systematic error introduced in the fitting. Please note that the experiment is not sensitive to neutral fragments. Theory results (D)–(F) are shown with the statistical error derived from the finite number of trajectories (see text). I used fluences of $0.75 \times 10^{11}$ (D), $1.80 \times 10^{11}$ (E), and $2.30 \times 10^{11}$ photons/μm$^2$ (F) in the calculations.

The calculated charge state distributions obtained from XMDYN are shown in Figs. 4.12D to 4.12F. They reproduce the average atomic charges with an average deviation of 12.5 % (and 12.5 % standard deviation). See also the values for the individual atoms in Table 4.2. For the $I^+$+$N^+$ case a remarkable agreement with the experimental charge state distribution is found - thus confirming that XMDYN can, at least in some cases, accurately model CREXIM (see also Section 4.3).

TABLE 4.2: **Deviation of theoretical average charges from the experimental values,** for the individual carbon atoms and three coincidence channels.

| | C2 | C3 | C4 | C5 | C6 |
|---|---|---|---|---|---|
| $I^{+}+N^{+}$ | +2.8 % | +5.6 % | +7.6 % | +3.8 % | +8.1 % |
| $I^{4+}+N^{2+}$ | +44.4 % | +25.3 % | +22.6 % | +19.0 % | +13.5 % |
| $I^{6+}+N^{2+}$ | +25.8 % | +4.7 % | +0.1 % | +2.4 % | -1.4 % |

However, the lower charge on the C2 atom for the higher-charge coincidences is not captured by the current XMDYN model. In contrast, XMOLECULE calculations for iodobenzene with fixed nuclei predict the experimentally observed electron density polarization, with the lower partial charges on the carbon atoms closer to the highly charged iodine. [22] Therefore, I believe that molecular orbitals are indispensable in order to accurately model the collective rearrangement of the ring electron density. In the current, computationally efficient version of XMDYN only individual atom pairs with atomic energy levels are taken into account in electron transfer events (see Section 2.4.1). In light of the computational iodobenzene study [22], we learn from the current experimental results (4.12B, 4.12C) that the electron rearrangement is not impeded by the nuclear motion (as it was conjectured for different pulse parameters also there). Please refer to Section 4.5.4 for an explanation.

The overestimation of the carbon charges for the higher-charge coincidences (Figs. 4.12E, 4.12F) could, aside from a too high fluence, also be caused by the assumption of a too short pulse duration in the calculations (see Section 4.5.9). In future work calculations for 20 fs pulse durations and $1.80 \times 10^{11}$ as well as $2.30 \times 10^{11}$ photons/μm$^2$ fluence could be additionally performed. It is conceivable that a longer pulse duration could have a stronger influence on the higher-charge coincidence channels, as a longer pulse duration enables more atomic motion during the ionization dynamics, and more highly charged ions move faster. This motion lets the potential barriers rise, which potentially causes more imbalance in the distribution of charge between iodine and the ring (i.e., lower carbon charges for a given iodine charge). Apart from this, it would be interesting to know which results for the charge state distributions are obtained using the approach described in Section 4.3, based on time-dependent partial charges in XMOLECULE calculations with fixed molecular geometry.

### Error bars in the charge state distributions

The theory results in Fig. 4.12 are depicted with statistical error bars. I applied the "common recipe" of taking the square root of the number of events $\sqrt{n}$ as error bars. [141] Here, this corresponds to the square root of the number of trajectories with the carbon atom in the respective final charge state $q$, $\sqrt{n_q}$. As the shown value itself $\frac{n_q}{N}$, also the error bar is given normalized to the total number of trajectories $N$, i.e., as $\frac{\sqrt{n_q}}{N}$. Underlying this $\sqrt{n}$ method is the assumption of a Poisson distribution. [141] In fact, the charge state distribution of every carbon atom is described by a multinomial distribution, the generalization of the bionomial distribution with more than two possible outcomes (here the charges from 0 to 6 are the possible outcomes). It is a property of the multinomial distribution that the abundance of each of the charges $q$ is given by a binomial distribution. The variance $\sigma^2$ of a binomially distributed variable is given as

$$\sigma^2 = N p_q \left(1 - p_q\right) . \tag{4.7}$$

I approximate the probability for each charge state $p_q$ with the relative abundance $\frac{n_q}{N}$ observed in the calculations, and define the absolute error $\Delta q$ for every charge state as the square root of the variance, i.e., the standard deviation

$$\Delta q = \sqrt{\cancel{N} \frac{n_q}{\cancel{N}} \left(1 - \frac{n_q}{N}\right)} . \tag{4.8}$$

For the normalized error $\frac{\Delta q}{N}$ follows

$$\frac{\Delta q}{N} = \frac{\sqrt{n_q \left(1 - \frac{n_q}{N}\right)}}{N} . \tag{4.9}$$

As a binomial distribution approaches a Poisson distribution in the case of rare events, Equation (4.9) only converges to $\frac{\sqrt{n_q}}{N}$ for $\frac{n_q}{N} \ll 1$. This is clearly not fulfilled here, at the sight of, for example, more than 80 % $C^{1+}$ in the $I^{+}+N^{+}$ coincidence channel. Since the missing factor $\sqrt{1 - \frac{n_q}{N}}$ is always smaller than 1, using $\frac{\sqrt{n_q}}{N}$ instead of Eq. (4.9) only results in overestimated, conservative error bars in Fig. 4.12, which is not a problem.

### 4.5.4 Higher-charge coincidence channels

The intense XFEL pulses generated not only ions with a charge of +1 (as shown in Fig. 4.9), but also ions carrying considerably higher charges: in the experimental data iodine ions with charges up to $I^{25+}$ are contained. Where statistics are sufficient, the coincidence channels with higher ion charges produce Newton plots which are qualitatively similar to Fig. 4.9, but the absolute ion momenta increase as a consequence of the higher charges. Figure 4.13 shows two exemplary higher-charge coincidence channels of 2-iodopyridine, in experiment and theory.

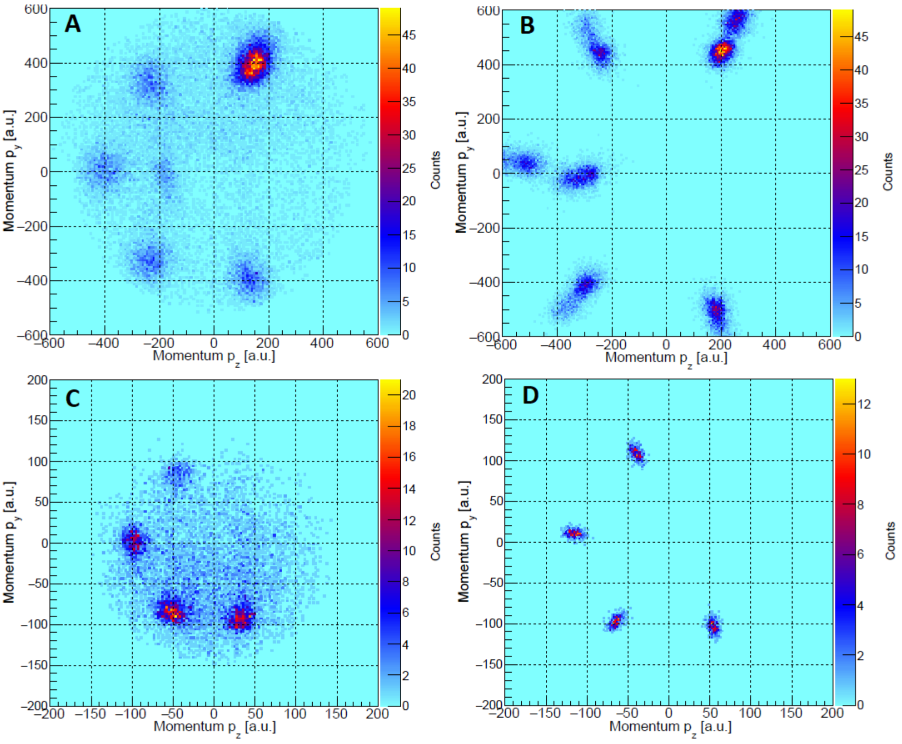

FIGURE 4.13: **Experimental and theoretical Newton plots of higher-charge coincidence channels.** $I^{4+}$+$N^{2+}$+$C^{3+}$ Newton plots in experiment (A) and theory (B), as well as $I^{6+}$+$N^{2+}$+$H^{+}$ Newton plots in experiment (C) and theory (D). I employed fluences of $1.8 \times 10^{11}$ (B) and $2.3 \times 10^{11}$ photons/μm$^2$ (D) in the calculations.

The slight smudginess in the experimental subfigures is probably a consequence of insufficient statistics. The agreement between experiment and theory is good, in particular for the proton momenta. The signals for the individual atoms are a bit further separated from each other than in the $I^{+}$+$N^{+}$+$C^{+}$ and $I^{+}$+$N^{+}$+$H^{+}$ cases. This confirms the finding in Ref. [41], that the mapping from initial atomic positions to final fragment momenta is more straightforward for higher charge states.

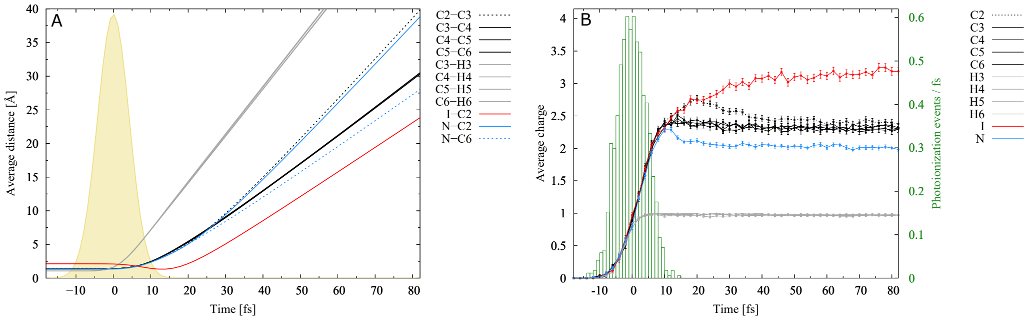

FIGURE 4.14: **Calculated time-dependent geometry and charge evolution of 2-iodopyridine molecules fragmenting into $I^{4+}$+$N^{2+}$ ions.** The average interatomic distances are shown in (A), and (B) depicts the average charge on each atom. In (A) the assumed Gaussian-shaped X-ray pulse of 10 fs FWHM is displayed, which is centered at 0 fs. In (B) it is shown in green how this assumed pulse finds expression in the average number of photoionization events per molecule and per femtosecond time interval. Error bars are not indicated in (A) because the standard errors of the mean would not be larger than the data point markers. In (B) the standard error of the mean is shown as error bars.

In comparison with the $I^{+}$+ $N^{+}$ coincidence (Fig. 4.10), in the case of the $I^{4+}$+ $N^{2+}$ coincidence (Fig. 4.14) the structural changes of 2-iodopyridine start earlier and take place with higher velocity. An I-C2 distance minimum is also found for this coincidence. Here it is reached immediately after the end of the pulse, at 13 fs, compared to 30 fs in the $I^{+}$+ $N^{+}$ case. The hydrogen charge evolution curves in Fig. 4.14B exhibit no maximum. Instead, the charges rise until nearly all hydrogens are ionized already 5 fs after the pulse center.

Figure 4.14 was generated from a subset of the trajectories yielding $I^{4+}$+ $N^{2+}$ ions at the end of the propagation time (see Section 4.5.7), calculated with a fluence of $7.5 \times 10^{10}$ photons/µm$^2$. When comparing Figs. 4.14A and 4.14B, it becomes clear that the charges on the carbon atoms predominantly build up in the simulations before the carbon and nitrogen ions move. This can serve as an explanation as to why the electron density polarization observed for the $I^{4+}$+$N^{2+}$ case experimentally is not impeded by the nuclear dynamics (see also Section 4.5.3).

### 4.5.5 Improvements of the model

#### Sudden kinetic energy transfer to the ion cores

In XMDYN electron transfer is carried out between two atoms whenever the over-the-barrier condition (Eq. (2.24) in Section 2.4.1) is found to be fulfilled. Equation (2.25) is not a necessary precondition for electron transfer in XMDYN, as it is rarely satisfied in systems with discrete energy levels and diverse atomic numbers as well as charge states. Obviously, then the question arises how to treat the energy differences between the orbitals involved in charge transfer events. In the previous XMDYN studies with electron transfer [59, 60], a methodology was employed which is also used in surface hopping methods [142], in order to ensure energy conservation after electron transfer between atomic orbitals with different energy. Energy was conserved via a small, but sudden kinetic energy transfer to the ion cores, executed in a directionality preserving momentum. Also the change in the total classical potential energy which can emerge following the displacement of a charge in an electron transfer event was compensated with such a sudden kinetic energy transfer to the ion cores.

In the earlier studies [59, 60] all atoms had the same atomic number, and due to the overall low ionization degree, the system typically consisted of neutral or singly charged atoms. Therefore, when performing charge transfer, typically the electronic configurations of two atoms were simply exchanged, yielding overall no change in the sum of atomic orbital energies and thus minimizing the energy differences that led to a sudden modification of ion kinetic energies in such a methodology. However, in the current CEI study, atomic numbers are different, and the system is highly ionized. Consequently, energy differences between the atomic orbitals involved in an electron transfer can emerge which are large, relative to the total kinetic energy of the system. Modifying ion kinetic energies to enforce strict energy conservation leads to artifacts in the Newton plots, as shown in Fig. 4.15, where data points are scattered and distinctive ion momentum distributions no longer persist.

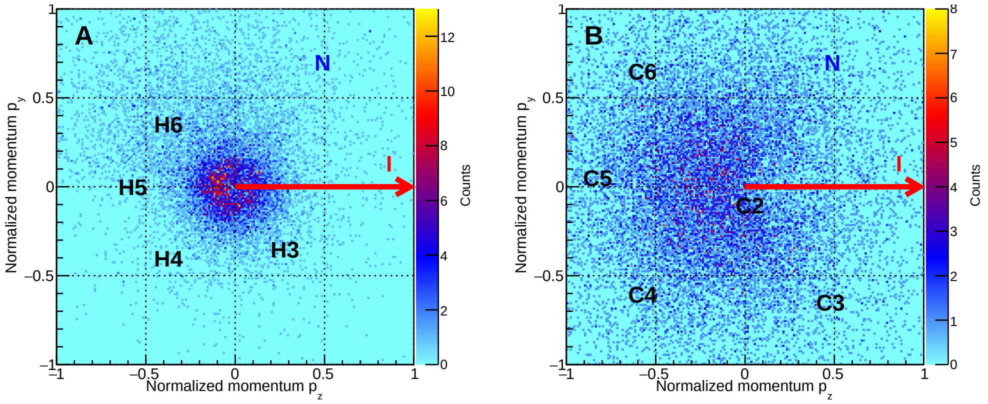

FIGURE 4.15: **Newton plots with sudden kinetic energy transfer to the ion cores.** Newton plots from XMDYN for a coincident detection of $I^+$ + $N^+$ and all occurring $H^+$ ions (A), and $I^+$ + $N^+$ and all occurring $C^+$ ions (B). These results were obtained with the old scheme of treating atomic orbital energy differences in electron transfer events (see text). The magnitudes of all ion momenta are normalized such that the iodine momentum equals 1 ($p_{I_z} = 1$)

A fully consistent framework for handling this general charge transfer case is not yet available and is a subject of further ongoing studies. Therefore, I disregarded the atomic orbital energy differences and changes of the potential energies in the current charge transfer scheme, and did not perform any sudden change of ion kinetic energies. With this approach I obtained the normalized Newton plots in Figs. 4.16A and 4.16B, which are in very good agreement with the experimental results (see Figs. 4.16C and 4.16D), and also the non-normalized Newton plots in Figs. 4.9 and 4.13. Consequently, the presented joint experimental and theoretical study is very valuable because the comparison with the experiment helped to improve XMDYN (see also below and Section 4.5.6).

Recalling how electrons in real molecules can transfer between electronic states differing in energy, there is, for example, internal conversion in a Jablonski diagram [143], where an electron can switch from an electronically excited state into an excited vibrational state of an energetically more deeply lying electronic state. When in the future XMDYDN will be equipped with a generic force field, one could analogously counterbalance (small) atomic orbital energy differences in electron transfer events by occupying a different vibrational state with the force field. The reactive force field ReaxFF being implemented in XMDYN can be used to calculate vibrational frequencies. [144]

In Ref. [132] it was emphasized that XMDYN obtains a greater spread in the ion kinetic energies than XMOLECULE, thus better resembling the experimental spread of kinetic energies. It can now be conjectured that this is, at least partially, an artifact caused by the additional kinetic energy given to the ions in electron transfer events.

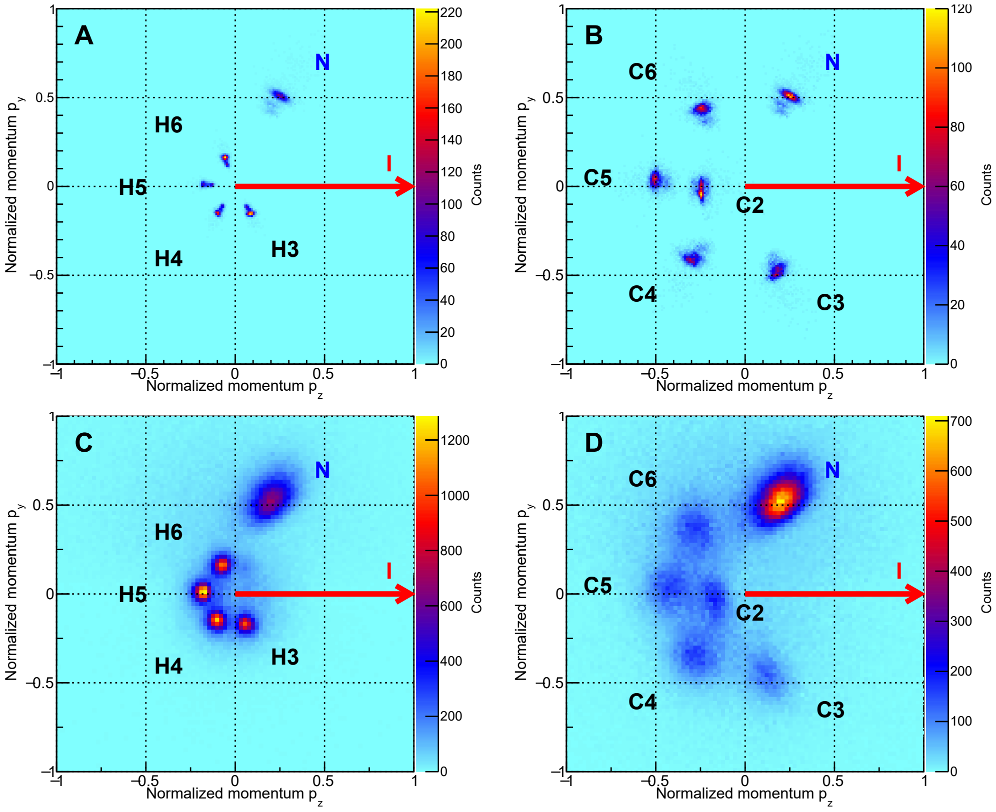

FIGURE 4.16: **Newton plots without sudden kinetic energy transfer to the ion cores.** Comparison of calculated $I^+ + N^+$ Newton plots from XMDYN (A, B) to experimental data (C, D). Shown are $H^+$ (A, C) and $C^+$ ion momenta (B, D). The magnitudes of all ion momenta are normalized such that the iodine momentum equals 1 ($p_{I_z} = 1$).

### Exclusion of electron transfer into the iodine *M*- and *N*-shells

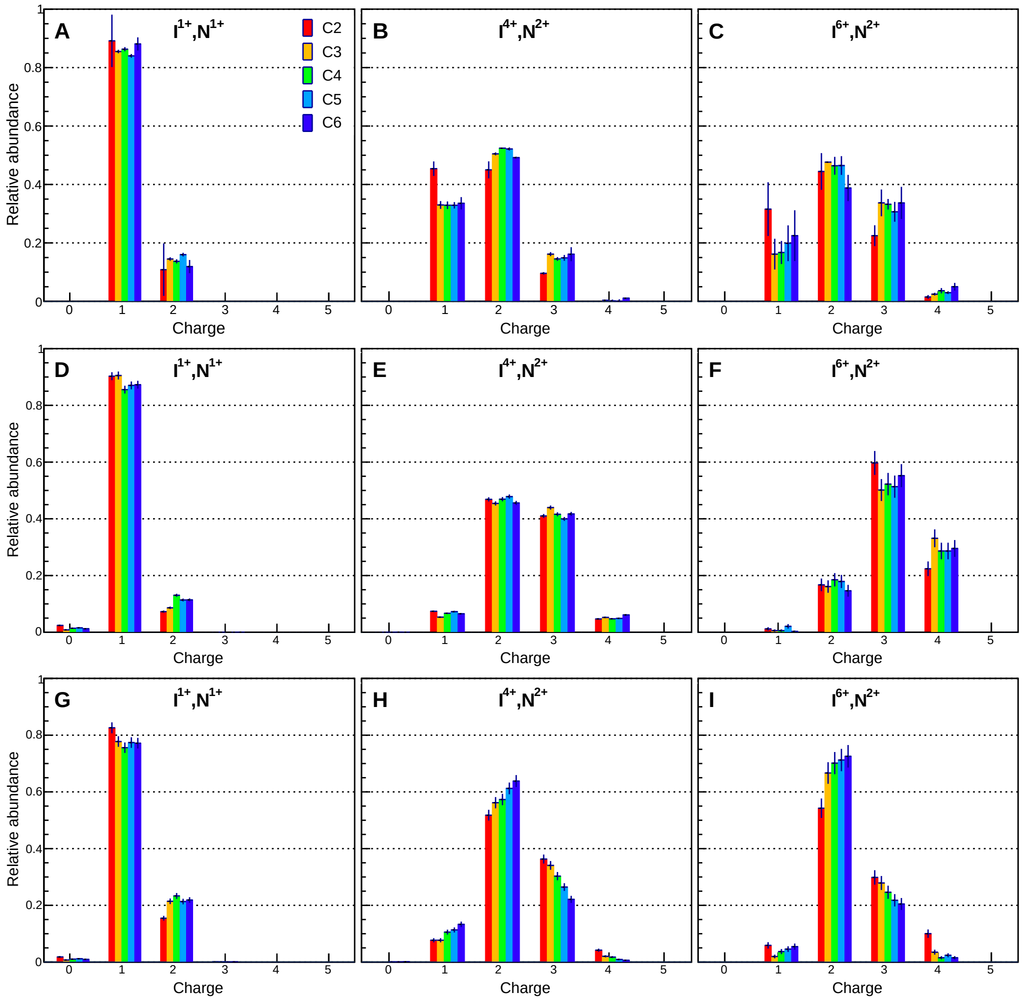

FIGURE 4.17: **Charge state distributions of carbon atoms in experiment and two theory versions,** for different coincidence channels of 2-iodopyridine. The experimental ion yields (A)–(C) are obtained by fitting a 2D Gaussian to each peak in the respective Newton plots (see Fig. 4.5). The experimental error bars represent an estimate of the systematic error introduced in the fitting. Please note that the experiment is not sensitive to neutral fragments. Theory results (D)–(I) are displayed with the statistical error derived from the finite number of trajectories. I employed fluences of $0.75 \times 10^{11}$ (D), (G), $1.80 \times 10^{11}$ (E), (H), and $2.3 \times 10^{11}$ photons/µm$^2$ (F), (I) in the calculations. Panels (D)–(F) show the results obtained from the initial model, i.e., when all orbitals of iodine with vacancy were considered. In a model refinement electron transfer into the iodine *M*- and *N*-shells was excluded (G)–(I).

The calculated charge state distributions which I obtained initially are shown in Figs. 4.17D to 4.17F. For the $I^+ + N^+$ coincidence a good agreement with the experimental data is found. However, for the higher-charge coincidences

(Figs. 4.17E, 4.17F), the distributions are shifted towards higher average charge as compared to the experimental findings. I show results for the fluences that maximize the percentage of the respective coincidence (see also Table 4.1 in Section 4.4). But even for considerably lower fluences I found a carbon charge overestimation for the higher-charge coincidences. I could then achieve a clearly improved agreement of the average total charges for the given fluences after exclusion of direct transfer of electrons from other atoms into the iodine *M*- and *N*-shells (see Figs. 4.17H and 4.17I). Allowing for such electron transfer, executed in the next 1-attosecond time step if the over-the-barrier condition (Eq. (2.24) in Section 2.4.1) is fulfilled, had neglected the Auger lifetimes (1.1 fs and 13.4 fs) of holes in the iodine *M*- and *N*-shells. These shells predominantly absorb X-ray photons at 2 keV photon energy (see also Section 4.5.8). Besides, the implementation of the over-the-barrier model was refined in such a way that the transferred electron no longer occupies the "outermost" acceptor atomic orbital with a vacancy (outermost is to signify the orbital with the highest quantum number). Instead, the electron is put into the orbital with a vacancy at the acceptor atom which is most similar in energy to the donor atom orbital that was originally occupied by the electron. This approach is based on quantum mechanical principles, and inspired by the findings in Chapter 5.

The results improved in this way (Figs. 4.17G to 4.17I) are also shown in the second row of Fig. 4.12.

### 4.5.6 Ion momenta in experiment and theory

The asymptotic ion momenta depicted in Fig. 4.9 are on average larger in the XMDYN simulations than in the experiment. For the $I^+$ + $N^+$ coincidence channel of 2-iodopyridine, the absolute iodine momenta are overestimated by about 60 % in the calculations, the $C^+$ momenta by about 40 %, the $N^+$ momentum by about 30 %, and the $H^+$ momenta by about 20 %. I ascribe the overestimation of the momenta to the lack of chemical bonds in the simulation, since chemical bonds give rise to a force naturally working against a Coulomb explosion of a molecule into atomic fragments.

In the study by Berrah *et al.* [60], the impact of chemical effects such as chemical bonds and charge transfer on the fragmentation of buckminsterfullerene after X-ray multiphoton ionization was investigated. They found for $C_{60}$ with $\sim$13 positive charges that the system does not undergo immediate fragmentation. Instead, it takes time for the $C_{60}$ molecule to break up into smaller fragments with still-existing chemical bonds. In addition, it was found that the XMDYN simulation with charge transfer and chemical bonds strongly reduced the maximum carbon atom displacement as compared to the XMDYN simulation without chemical effects, i.e., the chemical effects counteract the fragmentation and structural changes.

In the current study, the average charge on each of the eleven atoms in 2-iodopyridine is higher (calculated average total molecular charge of $+9$ for the $I^+$+$N^+$ coincidence). As discussed in Section 4.2, there is no evidence for the formation of intermediate molecular fragments. Therefore, an even larger part of the total accumulated electrostatic energy is spent on breaking the chemical bonds in the 2-iodopyridine molecule, diminishing the Coulomb energy being turned into kinetic energy, and thus the momenta of the atomic ions. The sum of all binding energies in the 2-iodopyridine molecule would be 54 eV, based on tabulated bond dissociation energies. In the current study, however, the molecule does not stay in its neutral ground state, but reaches highly ionized states, for which the binding energies are expected to be smaller.

In order to include chemical bonds for any given molecule in the XMDYN simulations (and not only phenomenologically for $C_{60}$, as described in Ref. [58]), Malik M. Abdullah and Dr. Zoltan Jurek have recently implemented a generic reactive force field (ReaxFF [145, 146]) that can describe bond breaking and bond formation, both of which are crucial in high-intensity X-ray studies. [18] While first test calculations on light-atom systems have been carried out, the force field is not yet ready for heavy atoms such as iodine and thus I could not use it in the work presented in this Ph.D. thesis.

For the coincidence channels involving higher charges, the overestimation of the iodine momentum is systematically lower the higher the ion charges are (about 50 % for $I^{4+}+N^{2+}$ and 40 % for $I^{6+}+N^{2+}$ vs. the mentioned 60 % for $I^{+}+N^{+}$). This can be explained with the missing chemical bonds becoming less important at higher total charges, as the underlying potential energy surfaces are more and more governed by pure Coulomb repulsion without bound potentials.

This reasoning is in accordance with the findings by Zhou *et al.* [41], that a model covering only Coulombic forces but no chemical bonds overestimates the fragment velocities for low charges, but achieves an increasingly adequate description for higher charges. Furthermore, this argumentation is supported by Corrales *et al.* [133] who propagated wavepackets on *ab initio* potential energy curves for the Coulomb explosion of $CH_3I$ into $CH_3^+$ and $I^{q+}$ ($q \leq 3$). They found that bound potentials could explain why they measured lower kinetic energy distributions of the fragment ions than those predicted considering only Coulomb repulsion forces.

As a last point, please note that aside from the incorporation of a force field, the XMDYN simulations would also be expected to achieve better agreement with experimental results in the case of higher molecular charging induced by a shorter pulse, resulting in practically purely Coulombic potential energy surfaces.

### 4.5.7 Late-time charge evolution

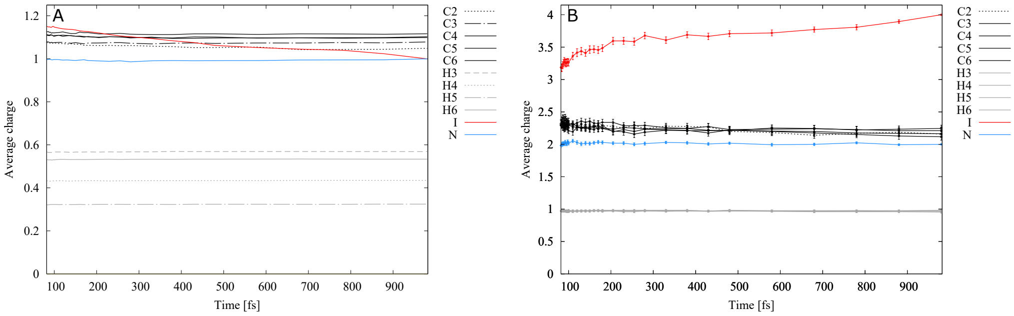

FIGURE 4.18: **Simulated late-time charge evolution of 2-iodopyridine molecules.** In both cases the time interval between 82 fs and 982 fs is shown, in continuation of Figs. 4.10D and 4.14B. At the end of the propagation time, the systems reach the coincidence condition of $I^{+}+N^{+}$ ions (A), and $I^{4+}+N^{2+}$ ions (B), respectively. Error bars are not shown in (A) because the standard errors of the mean would not be larger than the data point markers. In (B) the standard error of the mean is given as error bars.

In Fig. 4.10D the average charge on iodine is +1.15 at the latest shown time of 80 fs, in spite of the fact that only fragmentation events resulting in $I^{+}$ were selected from the data set. Similar to this, in Fig. 4.14B the average iodine charge is +3.19 after 80 fs, for trajectories yielding $I^{4+}$. These peculiarities can be understood by analyzing the late-time charge evolution displayed in Fig. 4.18, in which it becomes clear that the final iodine charge is reached in the model only after 1 ps. The late change of the iodine charge can be explained as follows: in the XMDYN framework free electrons ejected from the atoms after photoionization events or Auger decays are treated as classical particles. If these electrons are captured in the general electrostatic potential around a cluster of positively charged ions, they no longer count as free particles. Instead, they are considered as **delocalized** electrons. If an electron is close to one ion and its kinetic energy is lower than the electrostatic attraction towards the ion, it is essentially **trapped** in the field around the ion. More precisely, the code checks if the electron stays for $n$ full periods around the same ion, with $n$ being an input parameter. [58] If this condition is fulfilled, the system is identified as recombined, the electron is assigned to this ion, and the ion's charge is lowered by one. The chosen setting "ir no" (= recombination off, see Section 4.5.7) means that this assignment is not carried out internally in XMDYN during the run, but during postprocessing. In this retrospective procedure of checking for recombination, a conversion of a classical into a quantum bound electron cannot be performed. I.e., the electron is kept classical even if its classical orbiting energy is lower (more negative) than the orbital energy of the highest considered orbital containing a vacancy. [58]

I could trace back the late changes in the average iodine charges in Fig. 4.18 to these classically recombined electrons: the decrease in Fig. 4.18A is caused by an increase in the average number of electrons trapped around the iodine ion. Interestingly, the late iodine charge rise in Fig. 4.18 originates from a reduction of trapped electrons. A possible explanation could be autoionization-like events between either two trapped electrons or one delocalized electron and a trapped one, where one trapped electron receives enough energy to leave the field around the iodine ion. As a result, the charge assigned to the iodine ion increases by one.

### 4.5.8 Photoionization sites and CREXIM

My calculations show that at the given photon energy of 2 keV, 91 % of all photoionization events occur at the iodine site, both for all 15000 trajectories and the subset of 4560 $I^+ + N^+$ trajectories (see Table 4.3). Consequently, the vast majority of charges detected on carbon and nitrogen ions as well as protons are created by ultrafast electron transfer from the aromatic ring to the heavy absorber iodine, as in the previous studies on iodine-containing compounds at high X-ray intensities [21, 22]. The I 3*d* subshell accounts for the largest share of photoionization events, followed by the I 3*p* subshell.

TABLE 4.3: **Insight into the X-ray multiphoton ionization of 2-iodopyridine.** Given are the average number of photoionization events per trajectory and atomic photoionization sites in the XMDYN calculations for $7.5 \times 10^{10}$ photons/μm$^2$ fluence, 2 keV photon energy and 10 fs pulse duration. The value for C is summed up over all five carbon atoms.

| trajectories | av. photoionizations | C | H | I | N |
|---|---|---|---|---|---|
| all 15000 | 3.44±0.02 | 6.6 % | 0.0 % | 91.1% | 2.4 % |
| 4560 $I^+ + N^+$ | 3.32±0.02 | 7.1 % | 0.0 % | 90.6% | 2.3 % |
| 171 $I^{4+} + N^{2+}$ | 7.00±0.10 | 4.3 % | 0.0 % | 94.2% | 1.5 % |

Selecting $I^+ + N^+$ trajectories does not significantly alter the atomic site of photoionization compared to the average over all trajectories, whereas selecting $I^{4+} + N^{2+}$ trajectories implicates selecting cases where the photoionization events occurred even more predominantly at the iodine site than for the average over all trajectories. Table 4.3 additionally reveals that along the fragmentation pathway, which results in the coincidence with the final charges $I^+ + N^+$, an average of three photons are absorbed, while in the case of the $I^{4+} + N^{2+}$ coincidence, on average, seven photoionization events occur.

In order to quantify the molecular ionization enhancement, I carried out simulations for 2-iodopyridine as molecular system using XMDYN and XMOLECULE as well as in the independent-atom model using XATOM, for the same pulse parameters. Table 4.4 shows the results. Two features are salient: (a) the molecular ionization enhancement is almost twice as high based on the XMDYN results compared to the XMOLECULE results ($\Delta C_5H_4IN_{\text{XMDYN-IAM}} = +13.7 - (+10.5) = +3.2$ vs. $\Delta C_5H_4IN_{\text{XMOLECULE-IAM}} = +12.2 - (+10.5) =$

+1.7)). (b) XMDYN yields considerably higher charges on the ring atoms and a lower average charge on the iodine, compared to the XMOLECULE calculations with fixed molecular geometry.

Please keep in mind here that we know from Table 4.2 that XMDYN tends to overestimate the carbon charges in comparison with experimental values. It could be that the over-the-barrier model with initially constant exchange of electrons between the atoms [132] (here on average ∼60000 electron transfer events per $I^+ + N^+$ trajectory) overestimates the electron rearrangement from the ring to the iodine, leading to too high carbon charges and too low iodine charges. A lower average iodine charge in the XMDYN than in the XMOLECULE calculations at low fluences was also found in Ref. [132]. However, also the corresponding average total molecular charge was found to be lower with XMDYN than with XMOLECULE (see Fig. 4.7). There are three main differences in the calculations in Ref. [132]: electron transfer was allowed into all iodine shells (including the ensuing sudden kinetic energy transfer to the ion cores), the photon energy was 8.3 keV, and the XMOLECULE calculations included nuclear dynamics. At this point it is not clear why the average total charge is higher with XMDYN than with XMOLECULE. The reason is not that the ionization stops earlier in the molecular calculation with fixed nuclei due to the increased binding energies caused by the charged molecular environment, as in Chapter 3. At 2 keV photon energy, the iodine photoioionization channels close for iodine charges above +30 (see Chapter 3, both for isolated atomic iodine and iodine in a fixed molecular geometry), and the iodine charges in Table 4.2 are well below this value. Future work could aim at comparing the molecular ionization enhancement obtained with XMDYN and with XMOLECULE for more pulse parameter combinations and try to elucidate discrepancies.

TABLE 4.4: **Comparison of average charges obtained with XATOM, XMOLECULE and XMDYN.** Values are given with the standard error of the mean. In all calculations 2 keV photon energy, 10 fs FWHM pulse duration and 7.5 × $10^{10}$ photons/µm$^2$ fluence were assumed. Average over 200 XATOM (for iodine, 600) and 15000 XMDYN Monte Carlo trajectories. XMOLECULE average over Mulliken final partial charges of 50 Monte Carlo trajectories with fixed molecular geometry. For obtaining the XMDYN results electron transfer into the iodine *M*- and *N*-shells was excluded.

| | XATOM | XMOLECULE | XMDYN |
|---|---|---|---|
| $C_5H_4IN$ | +10.5 ± 0.4 | +12.2 ± 0.7 | +13.7 ± 0.1 |
| I | +9.7 ± 0.2 | +6.6 ± 0.5 | +2.5 ± 0.0 |
| N | +0.2 ± 0.0 | +0.6 ± 0.1 | +1.2 ± 0.0 |
| C | +0.1 ± 0.0 | | |
| H | +0.0 ± 0.0 | | |
| C2 | | +0.4 ± 0.1 | +1.5 ± 0.0 |
| C3 | | +0.3 ± 0.1 | +1.5 ± 0.0 |
| C4 | | +0.4 ± 0.1 | +1.5 ± 0.0 |
| C5 | | +0.5 ± 0.1 | +1.4 ± 0.0 |
| C6 | | +0.5 ± 0.1 | +1.4 ± 0.0 |
| H3 | | +0.7 ± 0.0 | +0.6 ± 0.0 |
| H4 | | +0.8 ± 0.0 | +0.7 ± 0.0 |
| H5 | | +0.8 ± 0.0 | +0.6 ± 0.0 |
| H6 | | +0.8 ± 0.0 | +0.7 ± 0.0 |

### 4.5.9 Pulse duration dependence: 10 fs vs. 20 fs

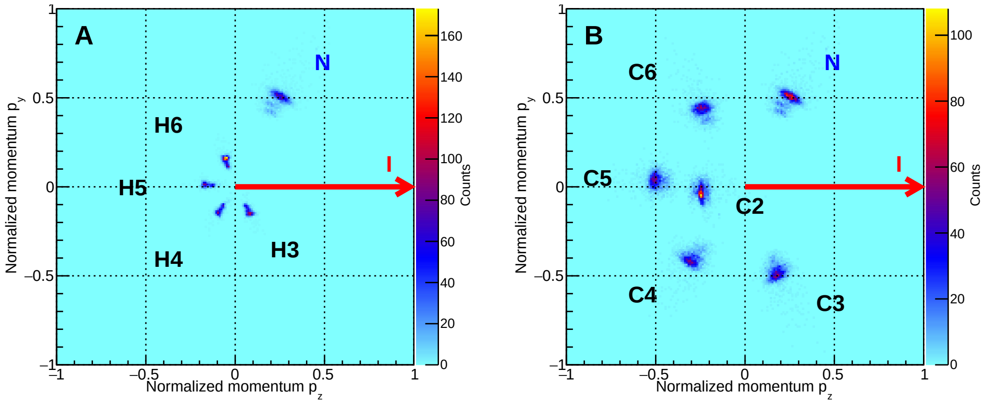

FIGURE 4.19: **Pulse duration dependence.** Newton plots from XMDYN for a pulse duration of 20 fs FWHM and a fluence of $7.5 \times 10^{10}$ photons/µm$^2$. Results are shown for a coincident detection of $I^+$+$N^+$ and all occurring $H^+$ ions (A), as well as $I^+$+$N^+$ and all occurring $C^+$ ions (B). The magnitudes of all ion momenta are normalized such that the $I^+$ momentum equals 1 ($p_{I_z} = 1$).

Based on the electron bunch charge of 250 pC in the accelerator, an upper limit for the experimental X-ray pulse duration of 25 fs was estimated. Up to the present, no direct measurement of the X-ray pulse duration has been performed at European XFEL.

From experiments at the XFEL LCLS it is known that X-ray pulse shapes need not necessarily match the electron bunch shapes, and that the X-ray pulse duration can well be as much as 50 % shorter than the electron bunch duration. [54, 94, 147] Apart from that, also during the described beam time at European XFEL different indirect measurements provided indications that the pulse duration could be shorter than 25 fs. Thus, almost all computational results presented in this thesis were generated assuming a pulse duration of 10 fs FWHM. Except for Fig. 4.19, where I assumed a 20 fs pulse in order to investigate the pulse duration dependence and try to make a statement about the actual pulse length in the experiment.

When comparing Fig. 4.19 with the analog for 10 fs in Fig. 4.16, it becomes clear that the pulse duration does not alter the normalized $I^+$+$N^+$ Newton plots significantly. Also the absolute ion momenta are very similar for both pulse durations (see Table 4.5). However, the absolute proton momenta are slightly less overestimated in the calculations for 20 fs pulse duration. This suggests that for a 20 fs pulse the protons leave the molecule even earlier than in the 10 fs case, earlier with respect to the full charge-up of the molecule. In order to verify this, it would be interesting to generate time-dependent geometry and charge evolution curves also for a 20 fs pulse, by analogy with Fig. 4.10 for the 10 fs pulse.

TABLE 4.5: **Comparison of absolute asymptotic fragment momenta in theory and experiment, given as ratio $\frac{p_{\text{Theory}}}{p_{\text{Experiment}}}$,** for the $I^+$+$N^+$ coincidence channel and two assumed pulse durations. Theory values are calculated for $7.5 \times 10^{10}$ photons/µm$^2$ fluence, and averaged over all hydrogen atoms, and over the C3, C4 and C5 atoms, respectively. Experimental values are averaged over all hydrogen and carbon atoms, respectively.

| ion species | 20 fs | 10 fs |
|---:|---|---|
| $I^+$ | 1.63 | 1.64 |
| av. $C^+$ | 1.41 | 1.41 |
| $N^+$ | 1.33 | 1.34 |
| av. $H^+$ | 1.15 | 1.22 |

On grounds of these computational results, it is not possible to assess the actual pulse duration in the experiment. Also the calculated average total molecular charge is very similar: +9.2 for 10 fs in comparison with +9.1 for 20 fs. However, the fraction of $I^+$+$N^+$ trajectories reduces from 30 % (10 fs) to 24 % (20 fs), at a given fluence of $7.5 \times 10^{10}$ photons/µm$^2$.

# Chapter 5

# Charge Transfer Scheme for XMDYN Based on Quantum Mechanical Principles

Both XMDYN [58] and XMOLECULE [23] do not model charge transfer on a microscopic level. In particular, they lack a proper timescale for it. In the XMOLECULE framework, after each ionization step the orbitals are instantaneously optimized for the new electronic configuration. Electron transfer happens through a gradual shift of the molecular orbitals in the course of the X-ray induced ionization dynamics. In contrast, in the XMDYN framework, electron transfer is modeled by immediate electron jumps between atoms in the next time step (e.g., 1 attosecond in Chapter 4), whenever the over-the-barrier condition is fulfilled (Eq. (2.24) in Section 2.4.1). As long as there is no potential barrier exceeding the involved energy levels, a constant electron transfer among atoms takes place in every time step. Besides, the classical over-the-barrier model for charge transfer between atoms or atomic ions cannot accurately describe neither molecular nor quantum mechanical properties. For instance, no quantum tunneling through the potential barrier is taken into account.

In order to fill this gap, a charge transfer scheme for XMDYN is derived in this chapter which is based on quantum mechanical principles.

## 5.1 Solution of the generalized eigenvalue problem

The charge transfer scheme presented in this chapter involves a minimal model, in which molecular orbitals are constructed by linear combinations of two atomic orbitals located on two different atoms. Within the framework of the model, the molecular orbitals can be evaluated analytically, thus rendering the model promising in terms of numerical efficiency.

When two atomic orbitals combine, they form two molecular orbitals. I approximate the molecular orbitals $|\psi_1\rangle$ and $|\psi_2\rangle$ as linear combinations of the atomic orbitals of the atoms $A$ and $B$, which are represented by the basis functions $|\phi_a\rangle$ and $|\phi_b\rangle$ (MO-LCAO),

$$|\psi_1\rangle = c_{1a}\,|\phi_a\rangle + c_{1b}\,|\phi_b\rangle \;, \tag{5.1}$$

and

$$|\psi_2\rangle = c_{2a}\,|\phi_a\rangle + c_{2b}\,|\phi_b\rangle \;. \tag{5.2}$$

The coefficients $c_{1a}$, $c_{1b}$, $c_{2a}$ and $c_{2b}$ give the contributions of the atomic orbitals to the molecular orbitals.

Since atomic orbitals at different atomic sites may overlap, the atomic orbital basis is non-orthogonal. Hence, a generalized eigenvalue problem in the type of Roothaan-Hall equations [69] has to be solved, namely

$$\underline{\underline{H}}\,\underline{c} = E\,\underline{\underline{S}}\,\underline{c}\,, \tag{5.3}$$

where $\underline{\underline{H}}$ denotes the Hamiltonian matrix, $\underline{c}$ is the generalized eigenvector and $E$ is the associated generalized energy eigenvalue. The assumption of normalized basis functions leads to the overlap matrix

$$\underline{\underline{S}} = \begin{pmatrix} 1 & S \\ S & 1 \end{pmatrix} \,, \tag{5.4}$$

where $S$ is given as

$$S = S_{ab} = \langle\phi_a|\phi_b\rangle \;. \tag{5.5}$$

The off-diagonal elements of the overlap matrix are not zero because the basis functions $|\phi_a\rangle$ and $|\phi_b\rangle$ at two different atomic sites form a non-orthogonal basis. The Hamiltonian matrix $\underline{\underline{H}}$ is given as

$$\underline{\underline{H}} = \begin{pmatrix} H_{aa} & H_{ab} \\ H_{ab} & H_{bb} \end{pmatrix} \,, \tag{5.6}$$

with

$$H_{aa} = \langle\phi_a|\,\hat{H}\,|\phi_a\rangle, \quad H_{ab} = \langle\phi_a|\,\hat{H}\,|\phi_b\rangle, \;\text{ and }\; H_{bb} = \langle\phi_b|\,\hat{H}\,|\phi_b\rangle\,.$$

The assumption of real basis functions and the hermiticity of the Hamiltonian $\hat{H}$ lead to $S = S_{ba} = S_{ab}$ in Eq. (5.4) and to $H_{ba} = H_{ab}$ in Eq. (5.6).

The present problem is reminiscent of the simplest model of a chemical bonding in the $H_2^+$ ion, with a basis of two atomic orbitals at two different atoms, and can be solved approximatively analytically analogously (see Section 5.1.4 of Ref. [71] for a good explanation for $H_2^+$). Here, however, the two atoms can be of different element types, such that in general

$$H_{bb} \neq H_{aa}\,, \tag{5.7}$$

which renders the expressions more complicated than in the $H_2^+$ case.

Inserting all approximations into Eq. (5.3), we obtain

$$\begin{pmatrix} H_{aa} & H_{ab} \\ H_{ab} & H_{bb} \end{pmatrix} \begin{pmatrix} c_a \\ c_b \end{pmatrix} = E \begin{pmatrix} 1 & S \\ S & 1 \end{pmatrix} \begin{pmatrix} c_a \\ c_b \end{pmatrix} \tag{5.8}$$

and the equations

$$H_{aa} \cdot c_a + H_{ab} \cdot c_b = E \cdot c_a + E \cdot S \cdot c_b \tag{5.9}$$

$$(H_{aa} - E) \cdot c_a + (H_{ab} - E \cdot S) \cdot c_b = 0 \tag{5.10}$$

$$H_{ab} \cdot c_a + H_{bb} \cdot c_b = E \cdot S \cdot c_a + E \cdot c_b \tag{5.11}$$

$$(H_{ab} - E \cdot S) \cdot c_a + (H_{bb} - E) \cdot c_b = 0 \tag{5.12}$$

Equations (5.10) and (5.12) form a homogeneous system of linear equations (secular equations) for the evaluation of the coefficients $c_a$ and $c_b$. Such a system of equations only has solutions other than the zero vector, if the secular determinant vanishes,

$$\begin{vmatrix} H_{aa} - E & H_{ab} - ES \\ H_{ab} - ES & H_{bb} - E \end{vmatrix} = 0\,. \tag{5.13}$$

Equation (5.13) is a quadratic equation in $E$,

$$(H_{aa} - E)(H_{bb} - E) - (H_{ab} - ES)^2 = 0\,, \tag{5.14}$$

$$E^2(1 - S^2) + E(2SH_{ab} - H_{aa} - H_{bb}) + H_{aa}H_{bb} - H_{ab}^2 = 0\,, \tag{5.15}$$

that can be used to evaluate two values for $E$, for which Eq. (5.13) is fulfilled. [71, 148] Such a quadratic equation can be solved using the quadratic formula.

### 5.1.1 Generalized energy eigenvalues

Equation (5.13) is solved for the molecular orbital energies

$$E_{1,2} = \frac{-(2SH_{ab} - H_{aa} - H_{bb}) \pm \sqrt{(2SH_{ab} - H_{aa} - H_{bb})^2 - 4(1 - S^2)(-H_{ab}^2 + H_{aa}H_{bb})}}{2(1 - S^2)}\,. \tag{5.16}$$

In order to render Expression (5.16) shorter and clearer, I will now introduce parameters. The parameter $V = H_{ab}$ serves as indicator of the coupling strength between the considered atomic orbitals of the atoms $A$ and $B$, which are represented by the basis functions $|\phi_a\rangle$ and $|\phi_b\rangle$. Moreover, the parameter $\Delta\epsilon = H_{aa} - H_{bb}$ denotes the difference between the matrix elements $H_{aa}$ and

$H_{bb}$, and $\bar{\epsilon} = \frac{H_{aa}+H_{bb}}{2}$ is introduced as the average value of $H_{aa}$ and $H_{bb}$.

Using these parameters, $H_{aa}$ and $H_{bb}$ can be rewritten as

$$H_{aa} = \frac{1}{2}\Delta\epsilon + \bar{\epsilon} \tag{5.17}$$

$$H_{bb} = -\frac{1}{2}\Delta\epsilon + \bar{\epsilon} \tag{5.18}$$

Thus, as generalized energy eigenvalues $E_1$ and $E_2$ of the molecular orbitals $|\psi_1\rangle$ and $|\psi_2\rangle$ I obtain

$$E_{1,2} = \frac{\bar{\epsilon} - V \cdot S}{1 - S^2} \pm \sqrt{\left(\frac{\bar{\epsilon} - V \cdot S}{1 - S^2}\right)^2 - \frac{\bar{\epsilon}^2 - \left(\frac{\Delta\epsilon}{2}\right)^2 - V^2}{1 - S^2}}\,. \tag{5.19}$$

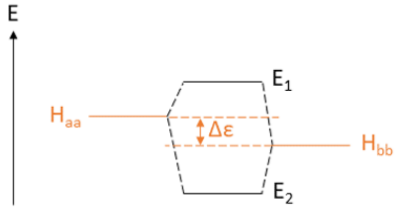

FIGURE 5.1: **Illustration of the different energy terms.** The fraction $\frac{E_1 - E_2}{\Delta\epsilon}$ describes the relative energy splitting of the molecular orbitals with respect to the difference $\Delta\epsilon$ between the matrix elements $H_{aa}$ and $H_{bb}$.

Figure 5.1 illustrates that the fraction $\frac{E_1 - E_2}{\Delta\epsilon}$ describes the relative energy splitting of the molecular orbitals with respect to the difference $\Delta\epsilon$ between the matrix elements $H_{aa}$ and $H_{bb}$. $H_{aa}$ and $H_{bb}$ become equal to the atomic orbital energies for infinite distance between the atoms $A$ and $B$.

For a vanishing overlap matrix element S=0, Equation (5.19) becomes

$$\frac{E_1 - E_2}{\Delta\epsilon} = \sqrt{1 + \left(\frac{V}{\frac{\Delta\epsilon}{2}}\right)^2}. \tag{5.20}$$

Figure 5.2 shows that this molecular energy splitting increases monotonically as a function of the ratio $\frac{V}{\Delta\epsilon}$.

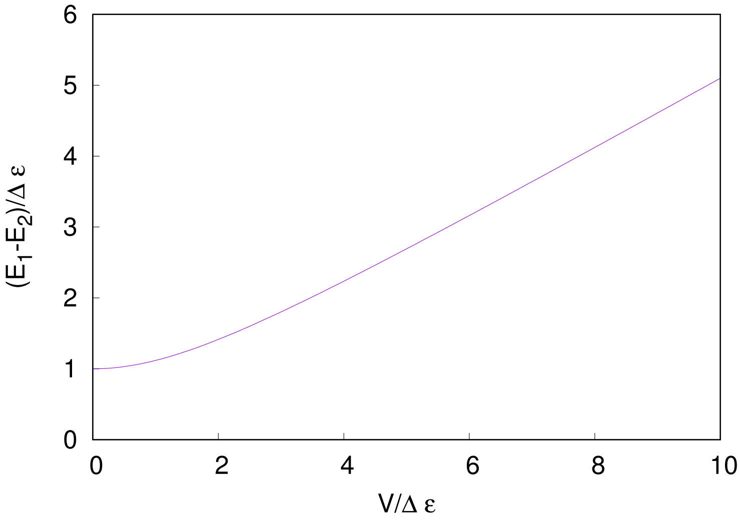

FIGURE 5.2: **The ratio $\frac{E_1 - E_2}{\Delta\epsilon}$ as a function of the ratio $\frac{V}{\Delta\epsilon}$ for $S = 0$.**

For $\frac{V}{\Delta\epsilon} = 0$, $\frac{E_1 - E_2}{\Delta\epsilon}$ equals 1, which means that the system **cannot achieve a relative energy gain by combining atomic orbitals to molecular orbitals** and occupying them partially[1]. $\frac{V}{\Delta\epsilon} = 0$ means that either the coupling matrix element $H_{ab}$ is equal to 0 or the difference between the matrix elements $H_{aa}$ and $H_{bb}$, $\Delta\epsilon$, is infinitely large. The monotonic increase in Fig. 5.2 means that for a given coupling strength $V$, **the energy splitting and molecular effects become more and more important**, the smaller the difference $\Delta\epsilon = H_{aa} - H_{bb}$ is, i. e., **the more similar the atomic orbitals are in energy**. On the other hand, the increase means also that for a given $\Delta\epsilon$ the relative molecular energy splitting increases as a function of the coupling matrix element $V$.

$$\frac{E_1 - E_2}{\Delta\epsilon} = \sqrt{\left(\frac{\left(\frac{\bar{\epsilon}}{\Delta\epsilon} - \frac{V \cdot S}{\Delta\epsilon}\right) \cdot 2}{1 - S^2}\right)^2 - \frac{\left(\frac{\bar{\epsilon}}{\Delta\epsilon}\right)^2 \cdot 4 - 1 - \left(\frac{V}{\Delta\epsilon}\right)^2 \cdot 4}{1 - S^2}} \tag{5.21}$$

As Equation (5.21) indicates, for a nonzero overlap matrix element $S$ the ratio $\frac{E_1 - E_2}{\Delta\epsilon}$ depends not only on $\frac{V}{\Delta\epsilon}$ and $S$, but also on $\frac{\bar{\epsilon}}{\Delta\epsilon}$. The fraction $\frac{\bar{\epsilon}}{\Delta\epsilon}$ denotes the ratio of the average value of $H_{aa}$ and $H_{bb}$ and the difference between $H_{aa}$ and $H_{bb}$. In the following, I will illustrate the dependencies by inserting values for the parameters in Eq. (5.21).

Figure 5.3 shows that for $S = 0.1$ and $\frac{\bar{\epsilon}}{\Delta\epsilon} = 10$, $\frac{E_1 - E_2}{\Delta\epsilon}$ has a minimum at $\frac{V}{\Delta\epsilon} = 1$ and $\frac{E_1 - E_2}{\Delta\epsilon} = 1$. As mentioned, $\frac{E_1 - E_2}{\Delta\epsilon} = 1$ implies that a system cannot gain energy by combining atomic orbitals to molecular orbitals and occupying them partially.

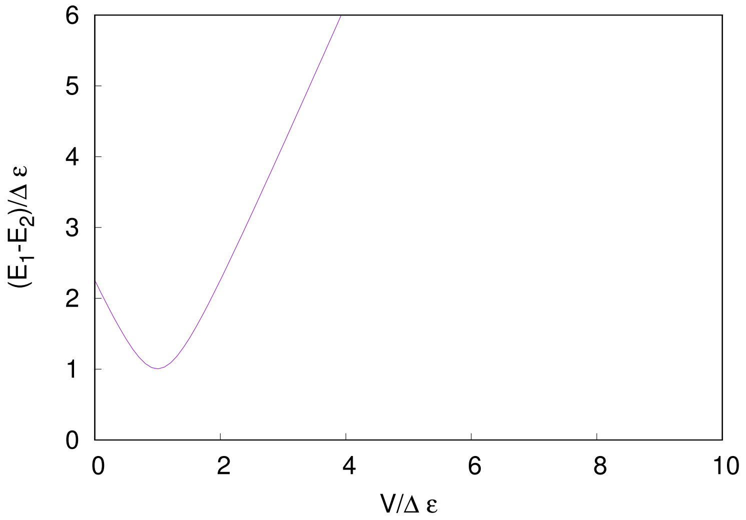

FIGURE 5.3: **The ratio $\frac{E_1 - E_2}{\Delta\epsilon}$ as a function of the ratio $\frac{V}{\Delta\epsilon}$ for $S = 0.1$ and $\frac{\bar{\epsilon}}{\Delta\epsilon} = 10$ .**

Increasing $S$ to 0.2, while maintaining $\frac{\bar{\epsilon}}{\Delta\epsilon} = 10$, shifts the minimum to $\frac{V}{\Delta\epsilon} = 2$ and $\frac{E_1 - E_2}{\Delta\epsilon} = 1$ (see Fig. 5.4).

---

[1] This refers to the ground state, in which electrons occupy orbitals in order from lowest to highest energy (Aufbau principle).

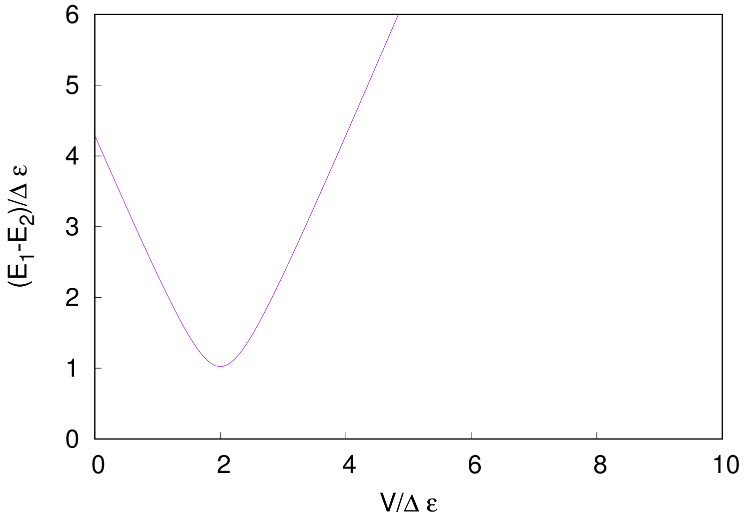

FIGURE 5.4: **The ratio $\frac{E_1-E_2}{\Delta\epsilon}$ as a function of the ratio $\frac{V}{\Delta\epsilon}$ for $S = 0.2$ and $\frac{\bar{\epsilon}}{\Delta\epsilon} = 10$.**

Figure 5.5 shows that, if $\frac{\bar{\epsilon}}{\Delta\epsilon}$ is then increased tenfold to 100, while maintaining $S = 0.2$, the minimum is shifted to $\frac{V}{\Delta\epsilon} = 20$ and $\frac{E_1-E_2}{\Delta\epsilon} = 1$.

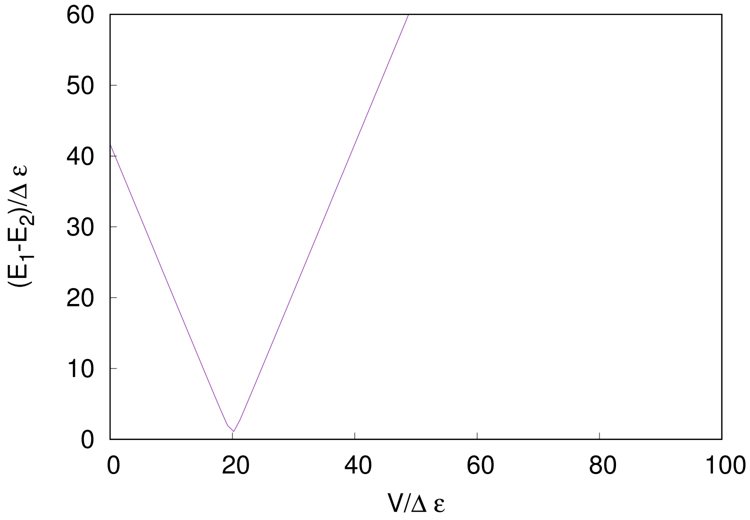

FIGURE 5.5: **The ratio $\frac{E_1-E_2}{\Delta\epsilon}$ as a function of the ratio $\frac{V}{\Delta\epsilon}$ for $S = 0.2$ and $\frac{\bar{\epsilon}}{\Delta\epsilon} = 100$.**

Halving $S$ to 0.1 when going from Fig. 5.5 to Fig. 5.6, shifts the minimum to $\frac{V}{\Delta\epsilon} = 10$ and $\frac{E_1-E_2}{\Delta\epsilon} = 1$.

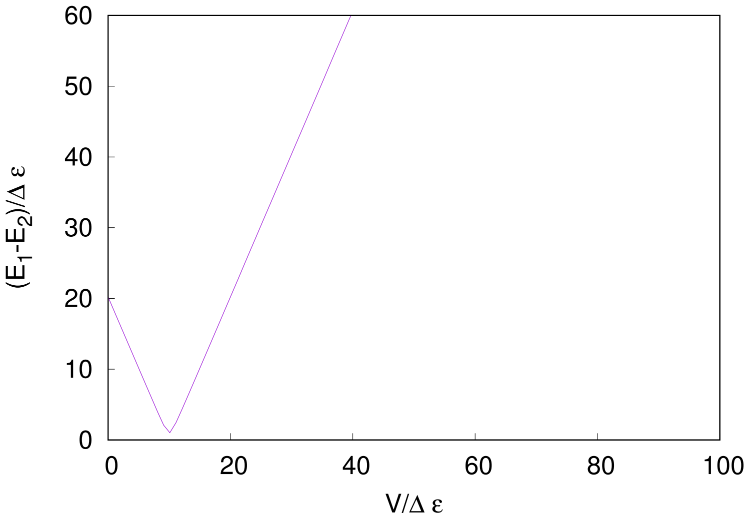

FIGURE 5.6: **The ratio $\frac{E_1-E_2}{\Delta\epsilon}$ as a function of the ratio $\frac{V}{\Delta\epsilon}$ for $S = 0.1$ and $\frac{\bar{\epsilon}}{\Delta\epsilon} = 100$.**

We learn that the $\frac{V}{\Delta\epsilon}$-value of the minimum is proportional to the overlap integral $S$ as well as to $\frac{\bar{\epsilon}}{\Delta\epsilon}$, the ratio of the average value of $\mathrm{H}_{aa}$ and $H_{bb}$ and the difference between $H_{aa}$ and $H_{bb}$.

### 5.1.2 Generalized eigenvectors

The next step is to determine the molecular orbitals $|\psi_1\rangle$ and $|\psi_2\rangle$ that belong to the two energy values $E_1$ and $E_2$ in Eq. (5.19). More precisely, in the MO-LCAO approach this means that we have to determine the respective coefficients of the linear combinations in Eqs. (5.1) and (5.2) by solving the secular equations given in Eqs. (5.10) and (5.12) for each of the two energy values. [71] In addition, the normalization condition that the molecular orbitals have to fulfill,

$$\langle\psi_1|\psi_1\rangle = |c_{1a}|^2 + 2\cdot|c_{1a}|\cdot|c_{1b}|\cdot|S| + |c_{1b}|^2 \overset{!}{=} 1\,, \tag{5.22}$$

$$\langle\psi_2|\psi_2\rangle = |c_{2a}|^2 + 2\cdot|c_{2a}|\cdot|c_{2b}|\cdot|S| + |c_{2b}|^2 \overset{!}{=} 1\,, \tag{5.23}$$

is used to determine the generalized eigenvectors.

The coefficients $c_{1a}$ and $c_{1b}$ for molecular orbital $|\psi_1\rangle$ are determined using Eq. (5.12), and the coefficients $c_{2a}$ and $c_{2b}$ for molecular orbital $|\psi_2\rangle$ are determined using Eq. (5.10) because otherwise one would divide by 0 for $V = S = 0$.

$$(H_{ab} - E_1 S)c_{1a} + (H_{bb} - E_1)c_{1b} = 0 \tag{5.24}$$

$$(H_{ab} - E_1 S)c_{1a} = -(H_{bb} - E_1)c_{1b} \tag{5.25}$$

$$c_{1b} = -\frac{H_{ab} - E_1 S}{H_{bb} - E_1}c_{1a} = -\frac{V - E_1 S}{H_{bb} - E_1}c_{1a} \tag{5.26}$$

$$(H_{aa} - E_2)c_{2a} + (H_{ab} - E_2 S)c_{2b} = 0 \tag{5.27}$$

$$(H_{aa} - E_2)c_{2a} = -(H_{ab} - E_2 S)c_{2b} \tag{5.28}$$

$$c_{2a} = -\frac{H_{ab} - E_2 S}{H_{aa} - E_2}c_{2b} = -\frac{V - E_2 S}{H_{aa} - E_2}c_{2b} \tag{5.29}$$

Inserting Eq. (5.26) into Eq. (5.1), and Eq. (5.29) into Eq. (5.2) yields

$$|\psi_1\rangle = c_{1a}\,|\phi_a\rangle - \frac{V - E_1 S}{H_{bb} - E_1}c_{1a}\,|\phi_b\rangle \tag{5.30}$$

$$|\psi_2\rangle = -\frac{V - E_2}{H_{aa} - E_2}c_{2b}\,|\phi_a\rangle + c_{2b}\,|\phi_b\rangle \tag{5.31}$$

By substituting $E_1$ and $E_2$ into Eqs. (5.30) and (5.31), and using the normalization conditions in Eqs. (5.22) and (5.23), I obtain results for the expansion coefficients $c_{1a}$, $c_{1b}$, $c_{2a}$ and $c_{2b}$ of the molecular orbitals, which are given below.

$$c_{1a} = \frac{1}{\sqrt{1 + 2S \cdot \left(-\frac{V - E_1 \cdot S}{H_{bb} - E_1}\right) + \left(-\frac{V - E_1 \cdot S}{H_{bb} - E_1}\right)^2}} \tag{5.32}$$

$$= \frac{1}{\sqrt{1 + 2S \cdot \underbrace{\left(-\frac{V - E_1 \cdot S}{-\frac{1}{2}\Delta\epsilon + \bar{\epsilon} - E_1}\right)}_{X_1} + \underbrace{\left(-\frac{V - E_1 \cdot S}{-\frac{1}{2}\Delta\epsilon + \bar{\epsilon} - E_1}\right)^2}_{X_1^2}}} = \frac{1}{\sqrt{1 + 2S \cdot X_1 + X_1^2}} \tag{5.33}$$

$$c_{1b} = -\frac{V - E_1 \cdot S}{H_{bb} - E_1} \cdot \frac{1}{\sqrt{1 + 2S \cdot \left(-\frac{V - E_1 \cdot S}{H_{bb} - E_1}\right) + \left(-\frac{V - E_1 \cdot S}{H_{bb} - E_1}\right)^2}} \tag{5.34}$$

$$= -\frac{V - E_1 \cdot S}{-\frac{1}{2}\Delta\epsilon + \bar{\epsilon} - E_1} \cdot \frac{1}{\sqrt{1 + 2S \cdot \left(-\frac{V - E_1 \cdot S}{-\frac{1}{2}\Delta\epsilon + \bar{\epsilon} - E_1}\right) + \left(-\frac{V - E_1 \cdot S}{-\frac{1}{2}\Delta\epsilon + \bar{\epsilon} - E_1}\right)^2}} \tag{5.35}$$

$$= \frac{X_1}{\sqrt{1 + 2S \cdot X_1 + X_1^2}} = X_1 \cdot c_{1a} \tag{5.36}$$

$$c_{2a} = -\frac{V - E_2 \cdot S}{H_{aa} - E_2} \cdot \frac{1}{\sqrt{1 + 2S \cdot \left(-\frac{V-E_2 \cdot S}{H_{aa}-E_2}\right) + \left(-\frac{V-E_2 \cdot S}{H_{aa}-E_2}\right)^2}} \tag{5.37}$$

$$= -\underbrace{\frac{V - E_2 \cdot S}{\frac{1}{2}\Delta\epsilon + \bar{\epsilon} - E_2}}_{X_2} \cdot \frac{1}{\sqrt{1 + 2S \cdot \underbrace{\left(-\frac{V - E_2 \cdot S}{\frac{1}{2}\Delta\epsilon + \bar{\epsilon} - E_2}\right)}_{X_2} + \underbrace{\left(-\frac{V - E_2 \cdot S}{\frac{1}{2}\Delta\epsilon + \bar{\epsilon} - E_2}\right)^2}_{X_2^2}}} \tag{5.38}$$

$$= \frac{X_2}{\sqrt{1 + 2S \cdot X_2 + X_2^2}} = X_2 \cdot c_{2b} \tag{5.39}$$

$$c_{2b} = \frac{1}{\sqrt{1 + 2S \cdot \left(-\frac{V-E_2 \cdot S}{H_{aa}-E_2}\right) + \left(-\frac{V-E_2 \cdot S}{H_{aa}-E_2}\right)^2}} \tag{5.40}$$

$$= \frac{1}{\sqrt{1 + 2S \cdot \underbrace{\left(-\frac{V - E_2 \cdot S}{\frac{1}{2}\Delta\epsilon + \bar{\epsilon} - E_2}\right)}_{X_2} + \underbrace{\left(-\frac{V - E_2 \cdot S}{\frac{1}{2}\Delta\epsilon + \bar{\epsilon} - E_2}\right)^2}_{X_2^2}}} = \frac{1}{\sqrt{1 + 2S \cdot X_2 + X_2^2}} \tag{5.41}$$

For indefinite distance $R \to \infty$ between the atoms $A$ and $B$, the atomic basis functions do not overlap ($S \to 0$). The off-diagonal element of the Hamiltonian matrix $H_{ab}$ vanishes as well if there is no overlap between the functions. Below, I will verify that for $S = H_{ab} = 0$ the molecular orbital $|\psi_1\rangle$ becomes identical to $|\phi_a\rangle$, and the molecular orbital $|\psi_2\rangle$ becomes identical to $|\phi_b\rangle$. In this case, Equation (5.8) turns into

$$\begin{pmatrix} H_{aa} & 0 \\ 0 & H_{bb} \end{pmatrix} \begin{pmatrix} c_a \\ c_b \end{pmatrix} = E \begin{pmatrix} c_a \\ c_b \end{pmatrix} . \tag{5.42}$$

For $R \to \infty$, $E_{1,2} \to H_{aa}, H_{bb}$:

$$\begin{pmatrix} H_{aa} & 0 \\ 0 & H_{bb} \end{pmatrix} \begin{pmatrix} c_{1a} \\ c_{1b} \end{pmatrix} = H_{aa} \begin{pmatrix} c_{1a} \\ c_{1b} \end{pmatrix} \tag{5.43}$$

$$H_{aa} \cdot c_{1a} = H_{aa} \cdot c_{1a} \tag{5.44}$$

$$H_{bb} \cdot c_{1b} = H_{aa} \cdot c_{1b} \tag{5.45}$$

$$\begin{pmatrix} H_{aa} & 0 \\ 0 & H_{bb} \end{pmatrix} \begin{pmatrix} c_{2a} \\ c_{2b} \end{pmatrix} = H_{bb} \begin{pmatrix} c_{2a} \\ c_{2b} \end{pmatrix} \tag{5.46}$$

$$H_{aa} \cdot c_{2a} = H_{bb} \cdot c_{2a} \tag{5.47}$$

$$H_{bb} \cdot c_{2b} = H_{bb} \cdot c_{2b} \tag{5.48}$$

We consider the general case of atoms $A$ and $B$ belonging to different element types, i.e., $H_{aa} \neq H_{bb}$. Therefore, Equations (5.45) and (5.47) only hold for $c_{1b} = 0$ and $c_{2a} = 0$. From the normalization conditions in Eqs. (5.22) and (5.23), it follows for the eigenvectors

$$\vec{c_1} = \begin{pmatrix} 1 \\ 0 \end{pmatrix} \tag{5.49}$$

and

$$\vec{c_2} = \begin{pmatrix} 0 \\ 1 \end{pmatrix} . \tag{5.50}$$

It could thus be shown that for $S = H_{ab} = 0$

$$|\psi_1\rangle = |\phi_a\rangle \tag{5.51}$$

and

$$|\psi_2\rangle = |\phi_b\rangle . \tag{5.52}$$

Furthermore, I verified that my results for the coefficients $c_{1a}$ , $c_{1b}$, $c_{2a}$ and $c_{2b}$ lead to molecular orbitals that satisfy the orthogonality condition

$$\langle\psi_1|\psi_2\rangle = 0 , \tag{5.53}$$

i.e.,

$$c_{1a}{}^* \cdot c_{2a} + c_{1a}{}^* \cdot c_{2b} \cdot S + c_{1b}{}^* \cdot c_{2a} \cdot S + c_{1b}{}^* \cdot c_{2b} \overset{!}{=} 0 \tag{5.54}$$

or

$$c_{1a} \cdot c_{2a} + c_{1a} \cdot c_{2b} \cdot S + c_{1b} \cdot c_{2a} \cdot S + c_{1b} \cdot c_{2b} \overset{!}{=} 0 \tag{5.55}$$

under the assumption of real basis functions that is made here. If the calculated molecular orbitals are eigenfunctions of the Hamiltonian $\hat{H}$, they must satisfy the orthogonality condition as they have different energy eigenvalues and I assumed $\hat{H}$ to be Hermitian.

## 5.2 Charge transfer dynamics

### 5.2.1 Construction of the wave packet

In Section 5.1 the molecular orbitals $|\psi_1\rangle$ and $|\psi_2\rangle$ were written in the atomic orbital basis as

$$|\psi_1\rangle = c_{1a}\,|\phi_a\rangle + c_{1b}\,|\phi_b\rangle \tag{5.56}$$

and

$$|\psi_2\rangle = c_{2a}\,|\phi_a\rangle + c_{2b}\,|\phi_b\rangle\ . \tag{5.57}$$

The results that were obtained for the expansion coefficients can now be used in order to describe charge transfer dynamics between atomic orbitals $|\phi_a\rangle$ and $|\phi_b\rangle$ by propagating a wave packet $|\Psi(t)\rangle$,

$$|\Psi(t)\rangle = e^{-\frac{i}{\hbar}\hat{H}t}\,|\Psi(0)\rangle = e^{-\frac{i}{\hbar}\hat{H}t}\,|\mu_1\psi_1 + \mu_2\psi_2\rangle = \mu_1\cdot e^{-\frac{i}{\hbar}E_1 t}\,|\psi_1\rangle + \mu_2\cdot e^{-\frac{i}{\hbar}E_2 t}\,|\psi_2\rangle\ , \tag{5.58}$$

where $\mu_1$ and $\mu_2$ are the expansion coefficients of the molecular orbitals in the expression for the wave packet at time $t = 0$. Under the assumption that the Hamiltonian $\hat{H}$ is time-independent, the time evolution operator is the exponential operator $e^{-\frac{i}{\hbar}\hat{H}t}$.

At time $t = 0$, the electron is assumed to be in a non-stationary state that is localized on atomic orbital $|\phi_a\rangle$, i.e., the wave packet at time $t = 0$ is

$$|\Psi(0)\rangle = \mu_1\,|\psi_1\rangle + \mu_2\,|\psi_2\rangle \overset{!}{=} |\phi_a\rangle\ . \tag{5.59}$$

By multiplying from the left side with $\langle\psi_1|$ and $\langle\psi_2|$, respectively, $\mu_1$ as well as $\mu_2$ can be determined.

$$\langle\psi_1|\Psi(0)\rangle = \mu_1\,\langle\psi_1|\psi_1\rangle + \mu_2\,\langle\psi_1|\psi_2\rangle = \langle\psi_1|\phi_a\rangle \tag{5.60}$$

$$\langle\psi_2|\Psi(0)\rangle = \mu_1\,\langle\psi_2|\psi_1\rangle + \mu_2\,\langle\psi_2|\psi_2\rangle = \langle\psi_2|\phi_a\rangle \tag{5.61}$$

Since $|\psi_1\rangle$ and $|\psi_2\rangle$ are normalized eigenstates of the Hermitian Hamiltonian $\hat{H}$ with different eigenvalues, they are orthogonal to each other, and thus $\langle\psi_1|\psi_2\rangle = 0$ and $\langle\psi_1|\psi_1\rangle = \langle\psi_2|\psi_2\rangle = 1$ can be used to simplify Eqs. (5.60) and (5.61).

$$\Rightarrow \mu_1 = \langle\psi_1|\phi_a\rangle = \langle c_{1a}\cdot\phi_a + c_{1b}\cdot\phi_b|\phi_a\rangle = {c_{1a}}^*\,\langle\phi_a|\phi_a\rangle + {c_{1b}}^*\,\langle\phi_b|\phi_a\rangle = {c_{1a}}^* + S\cdot{c_{1b}}^* \tag{5.62}$$

$$\Rightarrow \mu_2 = \langle\psi_2|\phi_a\rangle = \langle c_{2a}\cdot\phi_a + c_{2b}\cdot\phi_b|\phi_a\rangle = {c_{2a}}^*\,\langle\phi_a|\phi_a\rangle + {c_{2b}}^*\,\langle\phi_b|\phi_a\rangle = {c_{2a}}^* + S\cdot{c_{2b}}^* \tag{5.63}$$

I verified that my results for the coefficients $c_{1a}$, $c_{1b}$, $c_{2a}$ and $c_{2b}$ eventuate in coefficients $\mu_1$ and $\mu_2$, such that the wave packet $|\Psi(t)\rangle$ satisfies the normalization condition,

$$\langle \Psi(t)|\Psi(t)\rangle \overset{!}{=} 1\,. \tag{5.64}$$

It is sufficient to verify that the wave packet is normalized for $t = 0$ because in this case it stays normalized for all times as the time evolution operator is unitary. For $t = 0$ the normalization condition reads

$$\langle \Psi(0)|\Psi(0)\rangle \overset{!}{=} 1 \tag{5.65}$$

$$\Rightarrow \langle \mu_1\psi_1 + \mu_2\psi_2|\mu_1\psi_1 + \mu_2\psi_2\rangle \overset{!}{=} 1 \tag{5.66}$$

$$\Rightarrow |\mu_1|^2 \langle \psi_1|\psi_1\rangle + {\mu_1}^* \cdot \mu_2 \langle \psi_1|\psi_2\rangle + {\mu_2}^* \cdot \mu_1 \langle \psi_2|\psi_1\rangle + |\mu_2|^2 \langle \psi_2|\psi_2\rangle \overset{!}{=} 1 \tag{5.67}$$

Since $\langle \psi_1|\psi_1\rangle = \langle \psi_2|\psi_2\rangle = 1$ and $\langle \psi_1|\psi_2\rangle = \langle \psi_2|\psi_1\rangle = 0$:

$$\Rightarrow |\mu_1|^2 + |\mu_2|^2 \overset{!}{=} 1 \tag{5.68}$$

$$\Rightarrow |{c_{1a}}^* + S \cdot {c_{1b}}^*|^2 + |{c_{2a}}^* + S \cdot {c_{2b}}^*|^2 \overset{!}{=} 1 \tag{5.69}$$

$$\Rightarrow |{c_{1a}}^*|^2 + 2 \cdot |S| \cdot |{c_{1a}}^*| \cdot |{c_{1b}}^*| + |S|^2 \cdot |{c_{1b}}^*|^2 + |{c_{2a}}^*|^2 + 2 \cdot |S| \cdot |{c_{2a}}^*| \cdot |{c_{2b}}^*| + |S|^2 \cdot |{c_{2b}}^*|^2 \overset{!}{=} 1 \tag{5.70}$$

### 5.2.2 Charge transfer probability

By construction, the probability $P_a$ to find an electron in atomic orbital $|\phi_a\rangle$ is at time $t = 0$

$$P_a(t = 0) = |\, \langle \phi_a|\Psi(t = 0)\rangle \,|^2 = 1\,. \tag{5.71}$$

Accordingly, the complementary event $1 - P_a$ is the probability for an electron to leave atomic orbital $|\phi_a\rangle$. The probability to find an electron in atomic orbital $|\phi_b\rangle$ is denoted with $P_b$. Since $|\phi_a\rangle$ and $|\phi_b\rangle$ are non-orthogonal to each other,

$$P_a + P_b \neq 1 \tag{5.72}$$

and

$$1 - P_a \neq P_b\,. \tag{5.73}$$

We want to inspect the probability of charge transfer as a function of time. At time $t = 0$, the charge transfer probability $P_{CT}$ shall vanish,

$$P_{CT}(t = 0) \overset{!}{=} 0\,. \tag{5.74}$$

Due to

$$|\Psi(t = 0)\rangle \overset{!}{=} |\phi_a\rangle\ , \tag{5.75}$$

$$1 - P_a(t = 0) = 0\,. \tag{5.76}$$

Notably, this does not mean that $P_b(t = 0) = 0$, due to the non-orthogonality.

Hence, I choose in the following to express the charge transfer probability as the probability for an electron to leave atomic orbital $|\phi_a\rangle$, i.e., as $1 - P_a(t)$. The term $\langle\phi_a|\Psi(t)\rangle$ denotes the projection of the wave packet $|\Psi(t)\rangle$ onto the basis function $|\phi_a\rangle$. The assumption of real basis functions leads to $S = \langle\phi_a|\phi_b\rangle = \langle\phi_b|\phi_a\rangle$ in Eq. (5.82).

$$\begin{aligned}
P_{CT}(t) := 1 - P_a(t) &= 1 - |\,\langle\phi_a|\Psi(t)\rangle\,|^2 = 1 - |\,\langle\phi_a|\, e^{-\frac{i}{\hbar}\hat{H}t}\,|\Psi(0)\rangle\,|^2 && (5.77)\\
&= 1 - |\,\langle\phi_a|\, e^{-\frac{i}{\hbar}\hat{H}t}\,|\mu_1\psi_1 + \mu_2\psi_2\rangle\,|^2 && (5.78)\\
&= 1 - |\,\langle\phi_a|\, e^{-\frac{i}{\hbar}E_1 t}\,|\mu_1\psi_1\rangle + \langle\phi_a|\, e^{-\frac{i}{\hbar}E_2 t}\,|\mu_2\psi_2\rangle\,|^2 && (5.79)\\
&= 1 - |\mu_1 \cdot e^{-\frac{i}{\hbar}E_1 t}\,\langle\phi_a|\psi_1\rangle + \mu_2 \cdot e^{-\frac{i}{\hbar}E_2 t}\,\langle\phi_a|\psi_2\rangle\,|^2 && (5.80)\\
&= 1 - |\,\langle\psi_1|\phi_a\rangle \cdot e^{-\frac{i}{\hbar}E_1 t}\,\langle\phi_a|\psi_1\rangle + \langle\psi_2|\phi_a\rangle \cdot e^{-\frac{i}{\hbar}E_2 t}\,\langle\phi_a|\psi_2\rangle\,|^2 && (5.81)\\
&= 1 - |({c_{1a}}^* + S \cdot {c_{1b}}^*) \cdot e^{-\frac{i}{\hbar}E_1 t} \cdot (c_{1a} + S \cdot c_{1b}) && (5.82)\\
&\qquad + ({c_{2a}}^* + S \cdot {c_{2b}}^*) \cdot e^{-\frac{i}{\hbar}E_2 t}(c_{2a} + S \cdot c_{2b})|^2 \\
&= 1 - \left||c_{1a} + S \cdot c_{1b}|^2 \cdot e^{-\frac{i}{\hbar}E_1 t} + |c_{2a} + S \cdot c_{2b}|^2 \cdot e^{-\frac{i}{\hbar}E_2 t}\right|^2 && (5.83)\\
&= 1 - \Bigg\{\left|(|c_{1a}|^2 + 2 \cdot |S| \cdot |c_{1a}| \cdot |c_{1b}| + |S|^2 \cdot |c_{1b}|^2)\right|^2 && (5.84)\\
&\qquad + \left|(|c_{2a}|^2 + 2 \cdot |S| \cdot |c_{2a}| \cdot |c_{2b}| + |S|^2 \cdot |c_{2b}|^2)\right|^2 \\
&\qquad + 2 \cdot \left(|c_{1a}|^2 + 2 \cdot |S| \cdot |c_{1a}| \cdot |c_{1b}| + |S|^2 \cdot |c_{1b}|^2\right) \\
&\qquad \cdot \left(|c_{2a}|^2 + 2 \cdot |S| \cdot |c_{2a}| \cdot |c_{2b}| + |S|^2 \cdot |c_{2b}|^2\right) \cdot \cos\left[\left(\frac{E_1 - E_2}{\hbar}\right) t\right]\Bigg\}
\end{aligned}$$

In the last step I used that the absolute square of the sum of two complex numbers $z_1 = r_1 e^{i\phi_1}$ and $z_2 = r_2 e^{i\phi_2}$ is given as

$$|z_1 + z_2|^2 = (r_1 e^{-i\phi_1} + r_2 e^{-i\phi_2})((r_1 e^{i\phi_1} + r_2 e^{i\phi_2}) = r_1^2 + r_2^2 + 2 r_1 r_2 \cos(\phi_2 - \phi_1)\,. \tag{5.85}$$

### 5.2.3 Simplification of the expression for the charge transfer probability

In order to simplify the first and third bracket in Eq. (5.84), the normalization condition in Eq. (5.22) can be rearranged as

$$|c_{1a}|^2 + 2 \cdot |c_{1a}| \cdot |c_{1b}| \cdot |S| = 1 - |c_{1b}|^2 . \tag{5.86}$$

Adding $+|S|^2 \cdot |c_{1b}|^2$ on both sides yields

$$\begin{aligned} |c_{1a}|^2 + 2 \cdot |S| \cdot |c_{1a}| \cdot |c_{1b}| + |S|^2 \cdot |c_{1b}|^2 &= 1 - |c_{1b}|^2 + |S|^2 \cdot |c_{1b}|^2 && (5.87) \\ &= \underline{1 - (1 - |S|^2) \cdot |c_{1b}|^2} && (5.88) \end{aligned}$$

Analogously, the second and fourth bracket in Eq. (5.84) can be simplified as follows, using the normalization condition in Eq. (5.23).

$$|c_{2a}|^2 + 2 \cdot |c_{2a}| \cdot |c_{2b}| \cdot |S| = 1 - |c_{2b}|^2 \tag{5.89}$$

$$\begin{aligned} |c_{2a}|^2 + 2 \cdot |S| \cdot |c_{2a}| \cdot |c_{2b}| + |S|^2 \cdot |c_{2b}|^2 &= 1 - |c_{2b}|^2 + |S|^2 \cdot |c_{2b}|^2 && (5.90) \\ &= \underline{1 - (1 - |S|^2) \cdot |c_{2b}|^2} && (5.91) \end{aligned}$$

Substituting Eqs. (5.88) and (5.91) into Eq. (5.84), we obtain for the charge transfer probability $P_{CT}(t)$ the simplified expression

$$\begin{aligned} P_{CT}(t) := 1 - P_a(t) = 1 - \Bigg\{ \left|1 - (1 - |S|^2) \cdot |c_{1b}|^2\right|^2 + \left|1 - (1 - |S|^2) \cdot |c_{2b}|^2\right|^2 \\ +2 \cdot \left[1 - (1 - |S|^2) \cdot |c_{1b}|^2\right] \cdot \left[1 - (1 - |S|^2) \cdot |c_{2b}|^2\right] \cdot \cos\left[\left(\frac{E_1 - E_2}{\hbar}\right) t\right] \Bigg\} . \end{aligned} \tag{5.92}$$

Introducing parameter g as

$$g = 1 - |S|^2 , \tag{5.93}$$

shortens the expression further,

$$\begin{aligned} P_{CT}(t) := 1 - P_a(t) = 1 - \Bigg\{ \left|1 - g \cdot |c_{1b}|^2\right|^2 + \left|1 - g \cdot |c_{2b}|^2\right|^2 \\ +2 \cdot \left[1 - g \cdot |c_{1b}|^2\right] \cdot \left[1 - g \cdot |c_{2b}|^2\right] \cdot \cos\left[\left(\frac{E_1 - E_2}{\hbar}\right) t\right] \Bigg\} . \end{aligned} \tag{5.94}$$

Expanding the squares yields

$$\begin{aligned} P_{CT}(t) := 1 - P_a(t) = 1 - \Big\{ 2 - 2g \cdot \left( |c_{1b}|^2 + |c_{2b}|^2 \right) + g^2 \cdot \left( |c_{1b}|^4 + |c_{2b}|^4 \right) \\ +2 \cdot (1 - g \cdot |c_{1b}|^2) \cdot (1 - g \cdot |c_{2b}|^2) \cdot \cos\left[ \left( \frac{E_1 - E_2}{\hbar} \right) t \right] \Big\} \,. \end{aligned} \tag{5.95}$$

The normalization conditions in Eqs. (5.22) and (5.23) can be rearranged as

$$2 \cdot |S| \cdot |c_{1a}| \cdot |c_{1b}| = 1 - |c_{1a}|^2 - |c_{1b}|^2 \tag{5.96}$$

and

$$2 \cdot |S| \cdot |c_{2a}| \cdot |c_{2b}| = 1 - |c_{2a}|^2 - |c_{2b}|^2 \,. \tag{5.97}$$

Now I assume that the coefficients $c_{1a}$, $c_{1b}$, $c_{2a}$ and $c_{2b}$ are real. Consequently, Equation (5.70) turns into

$${c_{1a}}^2 + 2 \cdot |S| \cdot |c_{1a}| \cdot |c_{1b}| + S^2 \cdot {c_{1b}}^2 + {c_{2a}}^2 + 2 \cdot |S| \cdot |c_{2a}| \cdot |c_{2b}| + S^2 \cdot {c_{2b}}^2 \overset{!}{=} 1 \,. \tag{5.98}$$

Substituting in Eq. (5.98) the terms $2 \cdot |S| \cdot |c_{1a}| \cdot |c_{1b}|$ and $2 \cdot |S| \cdot |c_{2a}| \cdot |c_{2b}|$ with Eqs. (5.96) and (5.97) facilitates further simplifications.

$$\cancel{c_{1a}^2} + 1 - \cancel{c_{1a}^2} - c_{1b}^2 + S^2 \cdot c_{1b}^2 + \cancel{c_{2a}^2} + \cancel{1} - \cancel{c_{2a}^2} - c_{2b}^2 + S^2 \cdot c_{2b}^2 = \cancel{1} \tag{5.99}$$

$$1 - c_{1b}^2 - c_{2b}^2 + S^2 \cdot c_{1b}^2 + S^2 \cdot c_{2b}^2 = 0 \tag{5.100}$$

$$1 = (1 - S^2)(c_{1b}^2 + c_{2b}^2) \tag{5.101}$$

Transposing Eq. (5.101) yields

$$c_{1b}^2 + c_{2b}^2 = \frac{1}{1 - S^2} = \frac{1}{g} \tag{5.102}$$

and

$$c_{2b}^2 = \frac{1}{g} - c_{1b}^2 \,. \tag{5.103}$$

Inserting Eq. (5.102) into Eq. (5.95) leads to

$$\begin{aligned} P_{CT}(t) := 1 - P_a(t) = 1 - \Big\{ \cancel{2} - \cancel{2g} \cdot \frac{\cancel{1}}{\cancel{g}} + g^2 \cdot \left( {c_{1b}}^4 + {c_{2b}}^4 \right) \\ +2 \cdot (1 - g \cdot {c_{1b}}^2) \cdot (1 - g \cdot {c_{2b}}^2) \cdot \cos\left[ \left( \frac{E_1 - E_2}{\hbar} \right) t \right] \Big\} \,. \end{aligned} \tag{5.104}$$

Inserting also Eq. (5.103) and further simplification steps result in the final expression for the charge transfer probability given in Eq. (5.110).

$$P_{CT}(t) = 1 - \left\{ g^2 \cdot \left[ {c_{1b}}^4 + \left( \frac{1}{g} - {c_{1b}}^2 \right)^2 \right] + 2 \cdot (1 - g \cdot {c_{1b}}^2) \cdot \left[ 1 - g \cdot \left( \frac{1}{g} - {c_{1b}}^2 \right) \right] \cdot \cos \left[ \left( \frac{E_1 - E_2}{\hbar} \right) t \right] \right\} \tag{5.105}$$

$$= 1 - \left\{ g^2 \cdot \left( {c_{1b}}^4 + \frac{1}{g^2} - 2 \cdot \frac{1}{g} \cdot {c_{1b}}^2 + {c_{1b}}^4 \right) + 2 \cdot (1 - g \cdot {c_{1b}}^2) \cdot \left( \cancel{1} - \cancel{g} \cdot \frac{\cancel{1}}{\cancel{g}} + g \cdot {c_{1b}}^2 \right) \cdot \cos \left[ \left( \frac{E_1 - E_2}{\hbar} \right) t \right] \right\} \tag{5.106}$$

$$= 1 - \left\{ g^2 \cdot {c_{1b}}^4 + \cancel{g^2} \cdot \frac{1}{\cancel{g^2}} - g^{\cancel{2}} \cdot 2 \cdot \frac{1}{\cancel{g}} \cdot {c_{1b}}^2 + g^2 {c_{1b}}^4 + 2 \cdot (1 - g \cdot {c_{1b}}^2) \cdot g \cdot {c_{1b}}^2 \cdot \cos \left[ \left( \frac{E_1 - E_2}{\hbar} \right) t \right] \right\} \tag{5.107}$$

$$= 1 - \left\{ g^2 \cdot {c_{1b}}^4 + 1 - 2 \cdot g \cdot {c_{1b}}^2 + g^2 \cdot {c_{1b}}^4 + 2 \cdot g \cdot {c_{1b}}^2 (1 - g \cdot {c_{1b}}^2) \cdot \cos \left[ \left( \frac{E_1 - E_2}{\hbar} \right) t \right] \right\} \tag{5.108}$$

$$= \cancel{1} - 2 g^2 \cdot {c_{1b}}^4 - \cancel{1} + 2 \cdot g \cdot {c_{1b}}^2 - 2 \cdot g \cdot {c_{1b}}^2 \cdot \left( 1 - g \cdot {c_{1b}}^2 \right) \cdot \cos \left[ \left( \frac{E_1 - E_2}{\hbar} \right) t \right] \tag{5.109}$$

$$\underline{\underline{P_{CT}(t) = 1 - P_a(t) = 2 \cdot g \cdot {c_{1b}}^2 \cdot \left( 1 - g \cdot {c_{1b}}^2 \right) \left\{ 1 - \cos \left[ \left( \frac{E_1 - E_2}{\hbar} \right) t \right] \right\}}} \tag{5.110}$$

### 5.2.4 Charge transfer timescale

The timescale for charge transfer is given by the argument of the cosine function in Eq. (5.110). Since the curly bracket in Eq. (5.110) exhibits the structure $1 - \cos$, the minimum transfer probability is zero for $\cos(0) = 1$, i.e., for $t = 0$, as required in Eq. (5.74). Also for degenerate molecular orbitals with $E_1 = E_2$ the charge transfer probability vanishes. The charge oscillates between the two atoms with a frequency given by $\frac{E_1 - E_2}{\hbar}$. [149] Interestingly, for an energy splitting of the molecular orbitals, which is greater in magnitude ($|E_1 - E_2|$), the charge transfer thus occurs with higher frequency. The amplitude of the charge transfer dynamics is determined by the prefactor $A$ in front of the cosine,

$$A = -2gc_{1b}^2 + 2g^2c_{1b}^4 \tag{5.111}$$

$$= -2(1-S^2)c_{1b}^2 + 2(1-2S^2+S^4)c_{1b}^4\,. \tag{5.112}$$

The second term in Eq. (5.112) with the greater exponents results in an amplitude of the charge transfer probability that is increasing with larger overlap. The maximum transfer probability is determined by $\cos(\pi) = -1$. The timescale for the charge transfer is given by the time between minimum and maximum transfer probability,

$$\left(\frac{E_1 - E_2}{\hbar}\right) t_{CT} = \pi \tag{5.113}$$

$$t_{CT} = \pi \cdot \frac{\hbar}{E_1 - E_2} = \frac{h}{2(E_1 - E_2)}\,. \tag{5.114}$$

Thus, the goal of this chapter is reached and a charge transfer timescale $t_{CT}$ is derived that corresponds to half the period of the cosine function in Eq. (5.110). Inserting exemplary HOMO-LUMO gaps of CO and $N_2$ from Ref. [150] into Eq. (5.114), I calculate values for the charge transfer timescale $t_{CT}$ in the attosecond domain (see Table 5.1), which is known to be the timescale of electron dynamics. [151, 152]

TABLE 5.1: **Charge transfer timescale $t_{CT}$ for CO and $N_2$.** HOMO-LUMO gaps are taken from Ref. [150]

| | gap [eV] | $t_{CT}$ [as] |
|---|---|---|
| CO | 7 | 295 |
| $N_2$ | 8 | 259 |

For further illustration of Eq. (5.110), I will now insert values for the analytically solvable problem of $H_2^+$. [71] The needed Coulomb, exchange and overlap integrals for 1*s* orbitals are given in Ref. [153] as a function of the internuclear distance $R$. I assume the equilibrium bond length of $R = 2\,a_0$ [154] and obtain the time-dependent electron transfer probability as

$$P_{CT,H_2^+}(t) = 0.328\left[1 - \cos\left(1.625 \times 10^{16} t\right)\right]\,, \tag{5.115}$$

which is plotted in Fig. 5.7.

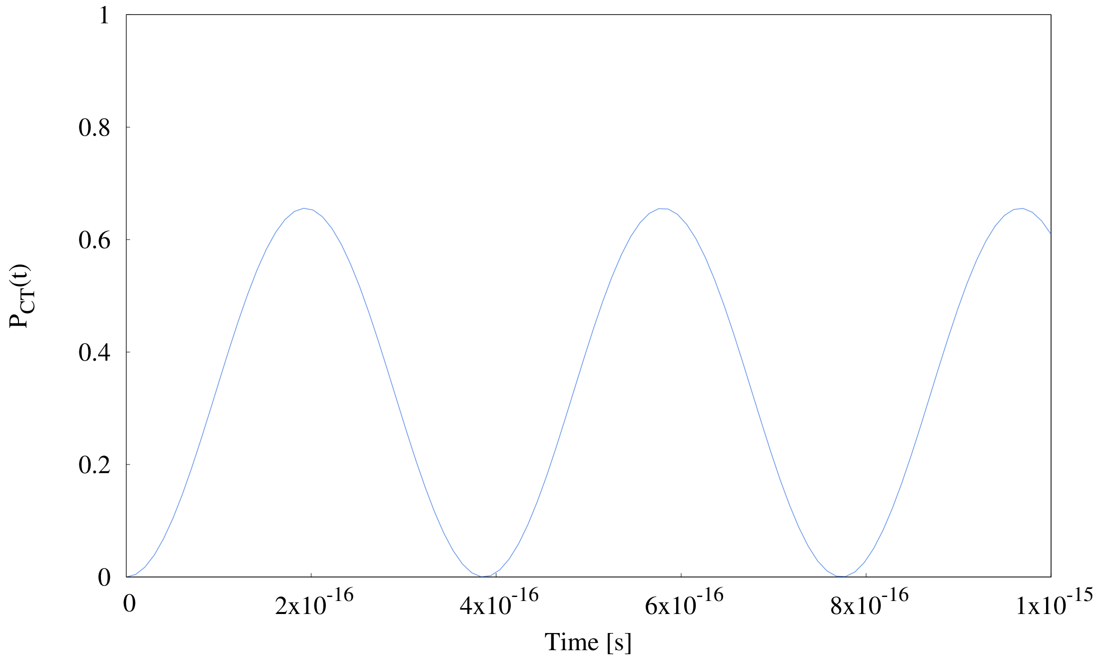

FIGURE 5.7: **Time-dependent electron transfer probability for $H_2^+$.** Depicted is Eq. (5.110) for 1*s* orbitals of $H_2^+$ in equilibrium bond distance. Overlap, Coulomb and exchange integrals are taken from Ref. [153].

It becomes clear that the maximum electron transfer probability is ∼66 %. Averaged over time the transfer probability is ∼33 %. The energy splitting between the molecular orbitals of the $H_2^+$ ion is 10.7 eV. According to Eq. (5.114), this corresponds to a charge transfer timescale of 193 as, which is half the period of the cosine function in Fig. 5.7.

### 5.2.5 Discussion

According to Molecular Orbital Theory, only atomic orbitals which are similar in energy and of the same symmetry combine to form molecular orbitals. Therefore also in the presented model, electron transfer should only be considered between atomic orbitals that fulfill these criteria.

Here, a coherent electronic wave packet is used to describe the electron dynamics between two atomic orbitals at two atomic sites, and nuclear motion is neglected. The consequence is the prediction of a long-lived oscillatory motion of the electron density. However, on timescales longer than a few femtoseconds decoherence effects may come into play, due to the coupling between electronic and nuclear motions, which would interrupt the oscillation and eventually lead to charge localization. [149, 155–157] In the XMDYN framework this effect could be mitigated and nuclear motion could be somewhat included by constructing a new charge transfer probability function $P_{CT}(t)$, e.g., every femtosecond, using the momentary atomic positions.

A possible implementation of the presented model into the XMDYN framework could be to evaluate the charge transfer probability function $P_{CT}(t)$ in every time step (e.g., 1 as) and perform electron transfer with the respective likelihood in the next time step (wavefunction collapse), such that both the oscillatory behavior and the transfer probability averaged over time are accurately reflected.

# Chapter 6

# Conclusions and Outlook

Simulating the X-ray multiphoton ionization of molecules at X-ray free-electron lasers (XFELs) is complex and requires computational tools specially developed for this purpose. In this Ph.D. thesis I presented different modeling strategies in this field and their results.

Optimizing the molecular electronic structure of every occurring multiple-hole electronic configuration, constitutes a large computational effort. This challenge is addressed by employing the Hartree-Fock-Slater [25] electronic structure model and the fixed-geometry assumption in my calculations on the 11-atom iodopyridine isomers. My results obtained with the *ab initio* toolkit XMOLECULE [23] reveal distinct differences between the molecular ionization induced by soft and hard XFEL pulses. In the soft X-ray regime, the light atoms are not only ionized via electron rearrangement towards the heavy absorber, but also notably through direct photoionization of the light atoms, as a consequence of higher photoionization cross sections. Another difference is that in the soft X-ray regime a large relative molecular ionization enhancement is observed already for low fluences, whereas in the previous studies with hard X-rays [21, 22], a molecular ionization enhancement was found only for higher fluences. These insights into the electronic radiation damage need to be taken into account in diffractive imaging experiments that utilize soft XFEL pulses.

For the parameter combination of 2 keV photon energy and $2 \times 10^{13}$ photons/$\mu$m$^2$ fluence I computed a peculiar, higher total charge for the sum of independent atoms than in the full molecular calculation. I ascribe this effect to three specific features in the calculations. Firstly, the ionization edge shifts above the photon energy of 2 keV by two charges earlier in a charged molecular environment as compared to the isolated-atom case. Secondly, the occupation numbers of the C 1*s* and N 1*s* orbitals suggest that the one-center approximation [108–113] overestimates the Auger lifetimes here, and that multi-center effects should be incorporated when calculating Auger decay rates of extremely highly charged molecules with delocalized valence orbitals. Thirdly, an insufficient basis set on iodine impedes effective valence electron transfer from the pyridyl ring to the iodine, where the electrons would have a higher probability of being ionized.

The maximum overlap method (MOM) [70] can be used to find higher-energy SCF solutions and is employed in the XMOLECULE framework to model the electronic structure of excited states. However, especially for high ionization degrees I encountered many cases, where this strategy did not yield a converged solution with molecular orbitals optimized for the respective occupation pattern. Instead, the molecular orbitals optimized for the previous configuration were then occupied according to the new electronic configuration. Hence, new strategies should be developed for finding higher-energy SCF solutions, that are not based on the orbital overlap. In a follow-up study my trajectories from Chapter 3 could be rerun, applying the recently developed fallback strategy [125, 126], that partially lifts the restrictions imposed by the MOM, to inspect if it can mitigate the SCF convergence problems. In addition, future work could include calculations on iodocyclohexane under the exact same conditions as in the iodobenzene study [22], to investigate to what extent the very efficient electron transfer across the ring is facilitated by the delocalized nature of the aromatic ring.

An alternative to full molecular electronic structure calculations is to approximate a molecule as a sum of atoms, that can exchange electrons based on a classical-over-the barrier model [61], and whose interaction with the X-rays is described with atomic *ab initio* X-ray physics. This computationally less costly approach is realized in the XMDYN [58] toolkit, and renders it possible to propagate the atom positions of an 11-atom molecule using classical molecular dynamics. My results show that this model can simulate the XFEL-induced Coulomb explosion of 2-iodopyridine and iodopyrazine surprisingly well. A clear improvement is achieved over a simple point-charge model that instantaneously assigns the final charge to all atoms at their equilibrium positions. The good agreement allowed me to add time-resolved information to the study, which was experimentally not accessible. I ascribe the remaining discrepancies between experimental and theoretical momenta to residual chemical bonding. Once the generic reactive force field is readily implemented into the XMDYN framework also for heavy atoms, it could be studied if the discrepancies can thus be overcome. In the long term, future work should then aim at establishing an iterative optimization scheme for geometry reconstructions of complex molecules [36, 40], using Coulomb explosion data from XFELs.

I started all trajectories with the molecular equilibrium geometries. However, the ion trajectories are expected to be significantly affected by the initial ground-state vibrations [56], which should be mapped to the final momentum patterns. Future simulations should include these initial structural fluctuations, and it would be interesting to see if these results reproduce better the large widths in the experimental momentum distributions. The other conceivable explanation for the widths of the experimental CEI peaks is the fluctuating nature of SASE pulses, which is currently not accurately represented in the calculations, where a simple Gaussian is assumed for the temporal profile.

The comparison with the experiment helped to improve the implementation of the over-the-barrier model in XMDYN. I could achieve much better agreement with the experimental Newton plots after refraining from performing sudden kinetic energy transfer to the ion cores. In a further model refinement, direct electron transfer into inner-shells was excluded, which can otherwise only be replenished via Auger or fluorescence decay. Moreover, the model was supplemented with quantum mechanical principles, such that electron transfer occurs between atomic orbitals which are most similar in energy.

Nevertheless, even after these improvements the electron transfer model in XMDYN exhibits deficiencies. For example, no quantum tunneling through the potential barrier is taken into account, and the time-dependence of electron transfer is not modeled on a microscopic level. Thus, I developed a charge transfer scheme based on quantum mechanical principles. It is being implemented as XOVERLAP into the XMDYN framework by Dr. Rui Jin, and gives electron transfer in XMDYN a solid foundation.

# Bibliography

[1] B. W. J. McNeil, N. R. Thompson, *Nature Photonics* **2010**, *4*, 814–821.

[2] C. Pellegrini, *Nature Reviews Physics* **2020**, *2*, 330–331.

[3] N. Rohringer, D. Ryan, R. A. London, M. Purvis, F. Albert, J. Dunn, J. D. Bozek, C. Bostedt, A. Graf, R. Hill, S. P. Hau-Riege, J. J. Rocca, *Nature* **2012**, *481*, 488–491.

[4] S. Huang, Y. Ding, Y. Feng, E. Hemsing, Z. Huang, J. Krzywinski, A. A. Lutman, A. Marinelli, T. J. Maxwell, D. Zhu, *Physical Review Letters* **2017**, *119*, 154801.

[5] J. Duris, S. Li, T. Driver, E. G. Champenois, J. P. MacArthur, A. A. Lutman, Z. Zhang, P. Rosenberger, J. W. Aldrich, R. Coffee, G. Coslovich, F.-J. Decker, J. M. Glownia, G. Hartmann, W. Helml, A. Kamalov, J. Knurr, J. Krzywinski, M.-F. Lin, J. P. Marangos, M. Nantel, A. Natan, J. T. O'Neal, N. Shivaram, P. Walter, A. L. Wang, J. J. Welch, T. J. A. Wolf, J. Z. Xu, M. F. Kling, P. H. Bucksbaum, A. Zholents, Z. Huang, J. P. Cryan, A. Marinelli, *Nature Photonics* **2020**, *14*, 30–36.

[6] H.-S. Kang, I. S. Ko, *Nature Photonics* **2020**, *14*, 7–8.

[7] P. Emma, R. Akre, J. Arthur, R. Bionta, C. Bostedt, J. Bozek, A. Brachmann, P. Bucksbaum, R. Coffee, F.-J. Decker, Y. Ding, D. Dowell, S. Edstrom, A. Fisher, J. Frisch, S. Gilevich, J. Hastings, G. Hays, P. Hering, Z. Huang, R. Iverson, H. Loos, M. Messerschmidt, A. Miahnahri, S. Moeller, H.-D. Nuhn, G. Pile, D. Ratner, J. Rzepiela, D. Schultz, T. Smith, P. Stefan, H. Tompkins, J. Turner, J. Welch, W. White, J. Wu, G. Yocky, J. Galayda, *Nature Photonics* **2010**, *4*, 641–647.

[8] T. Ishikawa, H. Aoyagi, T. Asaka, Y. Asano, N. Azumi, T. Bizen, H. Ego, K. Fukami, T. Fukui, Y. Furukawa, S. Goto, H. Hanaki, T. Hara, T. Hasegawa, T. Hatsui, A. Higashiya, T. Hirono, N. Hosoda, M. Ishii, T. Inagaki, Y. Inubushi, T. Itoga, Y. Joti, M. Kago, T. Kameshima, H. Kimura, Y. Kirihara, A. Kiyomichi, T. Kobayashi, C. Kondo, T. Kudo, H. Maesaka, X. M. Maréchal, T. Masuda, S. Matsubara, T. Matsumoto, T. Matsushita, S. Matsui, M. Nagasono, N. Nariyama, H. Ohashi, T. Ohata, T. Ohshima, S. Ono, Y. Otake, C. Saji, T. Sakurai, T. Sato, K. Sawada, T. Seike, K. Shirasawa, T. Sugimoto, S. Suzuki, S. Takahashi, H. Takebe, K. Takeshita, K. Tamasaku, H. Tanaka, R. Tanaka, T. Tanaka, T. Togashi, K. Togawa, A. Tokuhisa, H. Tomizawa, K. Tono, S. Wu, M. Yabashi, M. Yamaga, A. Yamashita, K. Yanagida, C. Zhang, T. Shintake, H. Kitamura, N. Kumagai, *Nature Photonics* **2012**, *6*, 540–544.

[9] I. Ko, H.-S. Kang, H. Heo, C. Kim, G. Kim, C.-K. Min, H. Yang, S. Baek, H.-J. Choi, G. Mun, B. Park, Y. Suh, D. Shin, J. Hu, J. Hong, S. Jung, S.-H. Kim, K. Kim, D. Na, S. Park, Y. Park, Y. Jung, S. Jeong, H. Lee, S. Lee, S. Lee, B. Oh, H. Suh, J.-H. Han, M. Kim, N.-S. Jung, Y.-C. Kim, M.-S. Lee, B.-H. Lee, C.-W. Sung, I.-S. Mok, J.-M. Yang, Y. Parc, W.-W. Lee, C.-S. Lee, H. Shin, J. Kim, Y. Kim, J. Lee, S.-Y. Park, J. Kim, J. Park, I. Eom, S. Rah, S. Kim, K. H. Nam, J. Park, J. Park, S. Kim, S. Kwon, R. An, S. Park, K. Kim, H. Hyun, S. Kim, S. Kim, C.-J. Yu, B.-S. Kim, T.-H. Kang, K.-W. Kim, S.-H. Kim, H.-S. Lee, H.-S. Lee, K.-H. Park, T.-Y. Koo, D.-E. Kim, K. Lee, *Applied Sciences* **2017**, *7*, 479.

[10] C. Milne, T. Schietinger, M. Aiba, A. Alarcon, J. Alex, A. Anghel, V. Arsov, C. Beard, P. Beaud, S. Bettoni, M. Bopp, H. Brands, M. Brönnimann, I. Brunnenkant, M. Calvi, A. Citterio, P. Craievich, M. Csatari Divall, M. Dällenbach, M. D'Amico, A. Dax, Y. Deng, A. Dietrich, R. Dinapoli, E. Divall, S. Dordevic, S. Ebner, C. Erny, H. Fitze, U. Flechsig, R. Follath, F. Frei, F. Gärtner, R. Ganter, T. Garvey, Z. Geng, I. Gorgisyan, C. Gough, A. Hauff, C. Hauri, N. Hiller, T. Humar, S. Hunziker, G. Ingold, R. Ischebeck, M. Janousch, P. Juranić, M. Jurcevic, M. Kaiser, B. Kalantari, R. Kalt, B. Keil, C. Kittel, G. Knopp, W. Koprek, H. Lemke, T. Lippuner, D. Llorente Sancho, F. Löhl, C. Lopez-Cuenca, F. Märki, F. Marcellini, G. Marinkovic, I. Martiel, R. Menzel, A. Mozzanica, K. Nass, G. Orlandi, C. Ozkan Loch, E. Panepucci, M. Paraliev, B. Patterson, B. Pedrini, M. Pedrozzi, P. Pollet, C. Pradervand, E. Prat, P. Radi, J.-Y. Raguin, S. Redford, J. Rehanek, J. Réhault, S. Reiche, M. Ringele, J. Rittmann, L. Rivkin, A. Romann, M. Ruat, C. Ruder, L. Sala, L. Schebacher, T. Schilcher, V. Schlott, T. Schmidt, B. Schmitt, X. Shi, M. Stadler, L. Stingelin, W. Sturzenegger, J. Szlachetko, D. Thattil, D. Treyer, A. Trisorio, W. Tron, S. Vetter, C. Vicario, D. Voulot, M. Wang, T. Zamofing, C. Zellweger, R. Zennaro, E. Zimoch, R. Abela, L. Patthey, H.-H. Braun, *Applied Sciences* **2017**, *7*, 720.

[11] W. Decking, S. Abeghyan, P. Abramian, A. Abramsky, A. Aguirre, C. Albrecht, P. Alou, M. Altarelli, P. Altmann, K. Amyan, V. Anashin, E. Apostolov, K. Appel, D. Auguste, V. Ayvazyan, S. Baark, F. Babies, N. Baboi, P. Bak, V. Balandin, R. Baldinger, B. Baranasic, S. Barbanotti, O. Belikov, V. Belokurov, L. Belova, V. Belyakov, S. Berry, M. Bertucci, B. Beutner, A. Block, M. Blöcher, T. Böckmann, C. Bohm, M. Böhnert, V. Bondar, E. Bondarchuk, M. Bonezzi, P. Borowiec, C. Bösch, U. Bösenberg, A. Bosotti, R. Böspflug, M. Bousonville, E. Boyd, Y. Bozhko, A. Brand, J. Branlard, S. Briechle, F. Brinker, S. Brinker, R. Brinkmann, S. Brockhauser, O. Brovko, H. Brück, A. Brüdgam, L. Butkowski, T. Büttner, J. Calero, E. Castro-Carballo, G. Cattalanotto, J. Charrier, J. Chen, A. Cherepenko, V. Cheskidov, M. Chiodini, A. Chong, S. Choroba, M. Chorowski, D. Churanov, W. Cichalewski, M. Clausen, W. Clement, C. Cloué, J. A. Cobos, N. Coppola, S. Cunis, K. Czuba, M. Czwalinna, B. D'Almagne, J. Dammann, H. Danared, A. de Zubiaurre Wagner, A. Delfs, T. Delfs, F. Dietrich, T. Dietrich, M. Dohlus, M. Dommach, A.

Donat, X. Dong, N. Doynikov, M. Dressel, M. Duda, P. Duda, H. Eckoldt, W. Ehsan, J. Eidam, F. Eints, C. Engling, U. Englisch, A. Ermakov, K. Escherich, J. Eschke, E. Saldin, M. Faesing, A. Fallou, M. Felber, M. Fenner, B. Fernandes, J. M. Fernández, S. Feuker, K. Filippakopoulos, K. Floettmann, V. Fogel, M. Fontaine, A. Francés, I. F. Martin, W. Freund, T. Freyermuth, M. Friedland, L. Fröhlich, M. Fusetti, J. Fydrych, A. Gallas, O. García, L. Garcia-Tabares, G. Geloni, N. Gerasimova, C. Gerth, P. Geßler, V. Gharibyan, M. Gloor, J. Głowinkowski, A. Goessel, Z. Gołębiewski, N. Golubeva, W. Grabowski, W. Graeff, A. Grebentsov, M. Grecki, T. Grevsmuehl, M. Gross, U. Grosse-Wortmann, J. Grünert, S. Grunewald, P. Grzegory, G. Feng, H. Guler, G. Gusev, J. L. Gutierrez, L. Hagge, M. Hamberg, R. Hanneken, E. Harms, I. Hartl, A. Hauberg, S. Hauf, J. Hauschildt, J. Hauser, J. Havlicek, A. Hedqvist, N. Heidbrook, F. Hellberg, D. Henning, O. Hensler, T. Hermann, A. Hidvégi, M. Hierholzer, H. Hintz, F. Hoffmann, M. Hoffmann, M. Hoffmann, Y. Holler, M. Hüning, A. Ignatenko, M. Ilchen, A. Iluk, J. Iversen, J. Iversen, M. Izquierdo, L. Jachmann, N. Jardon, U. Jastrow, K. Jensch, J. Jensen, M. Jeżabek, M. Jidda, H. Jin, N. Johansson, R. Jonas, W. Kaabi, D. Kaefer, R. Kammering, H. Kapitza, S. Karabekyan, S. Karstensen, K. Kasprzak, V. Katalev, D. Keese, B. Keil, M. Kholopov, M. Killenberger, B. Kitaev, Y. Klimchenko, R. Klos, L. Knebel, A. Koch, M. Koepke, S. Köhler, W. Köhler, N. Kohlstrunk, Z. Konopkova, A. Konstantinov, W. Kook, W. Koprek, M. Körfer, O. Korth, A. Kosarev, K. Kosiński, D. Kostin, Y. Kot, A. Kotarba, T. Kozak, V. Kozak, R. Kramert, M. Krasilnikov, A. Krasnov, B. Krause, L. Kravchuk, O. Krebs, R. Kretschmer, J. Kreutzkamp, O. Kröplin, K. Krzysik, G. Kube, H. Kuehn, N. Kujala, V. Kulikov, V. Kuzminych, D. La Civita, M. Lacroix, T. Lamb, A. Lancetov, M. Larsson, D. Le Pinvidic, S. Lederer, T. Lensch, D. Lenz, A. Leuschner, F. Levenhagen, Y. Li, J. Liebing, L. Lilje, T. Limberg, D. Lipka, B. List, J. Liu, S. Liu, B. Lorbeer, J. Lorkiewicz, H. H. Lu, F. Ludwig, K. Machau, W. Maciocha, C. Madec, C. Magueur, C. Maiano, I. Maksimova, K. Malcher, T. Maltezopoulos, E. Mamoshkina, B. Manschwetus, F. Marcellini, G. Marinkovic, T. Martinez, H. Martirosyan, W. Maschmann, M. Maslov, A. Matheisen, U. Mavric, J. Meißner, K. Meissner, M. Messerschmidt, N. Meyners, G. Michalski, P. Michelato, N. Mildner, M. Moe, F. Moglia, C. Mohr, S. Mohr, W. Möller, M. Mommerz, L. Monaco, C. Montiel, M. Moretti, I. Morozov, P. Morozov, D. Mross, J. Mueller, C. Müller, J. Müller, K. Müller, J. Munilla, A. Münnich, V. Muratov, O. Napoly, B. Näser, N. Nefedov, R. Neumann, R. Neumann, N. Ngada, D. Noelle, F. Obier, I. Okunev, J. A. Oliver, M. Omet, A. Oppelt, A. Ottmar, M. Oublaid, C. Pagani, R. Paparella, V. Paramonov, C. Peitzmann, J. Penning, A. Perus, F. Peters, B. Petersen, A. Petrov, I. Petrov, S. Pfeiffer, J. Pflüger, S. Philipp, Y. Pienaud, P. Pierini, S. Pivovarov, M. Planas, E. Pławski, M. Pohl, J. Polinski, V. Popov, S. Prat, J. Prenting, G. Priebe, H. Pryschelski, K.

Przygoda, E. Pyata, B. Racky, A. Rathjen, W. Ratuschni, S. Regnaud-Campderros, K. Rehlich, D. Reschke, C. Robson, J. Roever, M. Roggli, J. Rothenburg, E. Rusiński, R. Rybaniec, H. Sahling, M. Salmani, L. Samoylova, D. Sanzone, F. Saretzki, O. Sawlanski, J. Schaffran, H. Schlarb, M. Schlösser, V. Schlott, C. Schmidt, F. Schmidt-Foehre, M. Schmitz, M. Schmökel, T. Schnautz, E. Schneidmiller, M. Scholz, B. Schöneburg, J. Schultze, C. Schulz, A. Schwarz, J. Sekutowicz, D. Sellmann, E. Semenov, S. Serkez, D. Sertore, N. Shehzad, P. Shemarykin, L. Shi, M. Sienkiewicz, D. Sikora, M. Sikorski, A. Silenzi, C. Simon, W. Singer, X. Singer, H. Sinn, K. Sinram, N. Skvorodnev, P. Smirnow, T. Sommer, A. Sorokin, M. Stadler, M. Steckel, B. Steffen, N. Steinhau-Kühl, F. Stephan, M. Stodulski, M. Stolper, A. Sulimov, R. Susen, J. Świerblewski, C. Sydlo, E. Syresin, V. Sytchev, J. Szuba, N. Tesch, J. Thie, A. Thiebault, K. Tiedtke, D. Tischhauser, J. Tolkiehn, S. Tomin, F. Tonisch, F. Toral, I. Torbin, A. Trapp, D. Treyer, G. Trowitzsch, T. Trublet, T. Tschentscher, F. Ullrich, M. Vannoni, P. Varela, G. Varghese, G. Vashchenko, M. Vasic, C. Vazquez-Velez, A. Verguet, S. Vilcins-Czvitkovits, R. Villanueva, B. Visentin, M. Viti, E. Vogel, E. Volobuev, R. Wagner, N. Walker, T. Wamsat, H. Weddig, G. Weichert, H. Weise, R. Wenndorf, M. Werner, R. Wichmann, C. Wiebers, M. Wiencek, T. Wilksen, I. Will, L. Winkelmann, M. Winkowski, K. Wittenburg, A. Witzig, P. Wlk, T. Wohlenberg, M. Wojciechowski, F. Wolff-Fabris, G. Wrochna, K. Wrona, M. Yakopov, B. Yang, F. Yang, M. Yurkov, I. Zagorodnov, P. Zalden, A. Zavadtsev, D. Zavadtsev, A. Zhirnov, A. Zhukov, V. Ziemann, A. Zolotov, N. Zolotukhina, F. Zummack, D. Zybin, *Nature Photonics* **2020**, *14*, 391–397.

[12] E. Allaria, R. Appio, L. Badano, W. Barletta, S. Bassanese, S. Biedron, A. Borga, E. Busetto, D. Castronovo, P. Cinquegrana, S. Cleva, D. Cocco, M. Cornacchia, P. Craievich, I. Cudin, G. D'Auria, M. Dal Forno, M. Danailov, R. De Monte, G. De Ninno, P. Delgiusto, A. Demidovich, S. Di Mitri, B. Diviacco, A. Fabris, R. Fabris, W. Fawley, M. Ferianis, E. Ferrari, S. Ferry, L. Froehlich, P. Furlan, G. Gaio, F. Gelmetti, L. Giannessi, M. Giannini, R. Gobessi, R. Ivanov, E. Karantzoulis, M. Lonza, A. Lutman, B. Mahieu, M. Milloch, S. Milton, M. Musardo, I. Nikolov, S. Noe, F. Parmigiani, G. Penco, M. Petronio, L. Pivetta, M. Predonzani, F. Rossi, L. Rumiz, A. Salom, C. Scafuri, C. Serpico, P. Sigalotti, S. Spampinati, C. Spezzani, M. Svandrlik, C. Svetina, S. Tazzari, M. Trovo, R. Umer, A. Vascotto, M. Veronese, R. Visintini, M. Zaccaria, D. Zangrando, M. Zangrando, *Nature Photonics* **2012**, *6*, 699–704.

[13] W. Ackermann, G. Asova, V. Ayvazyan, A. Azima, N. Baboi, J. Bähr, V. Balandin, B. Beutner, A. Brandt, A. Bolzmann, R. Brinkmann, O. I. Brovko, M. Castellano, P. Castro, L. Catani, E. Chiadroni, S. Choroba, A. Cianchi, J. T. Costello, D. Cubaynes, J. Dardis, W. Decking, H. Delsim-Hashemi, A. Delserieys, G. Di Pirro, M. Dohlus, S. Düsterer, A. Eckhardt, H. T. Edwards, B. Faatz, J. Feldhaus, K. Flöttmann, J. Frisch, L. Fröhlich, T. Garvey, U. Gensch, C. Gerth, M. Görler, N. Golubeva, H.-J. Grabosch, M. Grecki, O. Grimm, K. Hacker, U. Hahn, J. H. Han,

K. Honkavaara, T. Hott, M. Hüning, Y. Ivanisenko, E. Jaeschke, W. Jalmuzna, T. Jezynski, R. Kammering, V. Katalev, K. Kavanagh, E. T. Kennedy, S. Khodyachykh, K. Klose, V. Kocharyan, M. Körfer, M. Kollewe, W. Koprek, S. Korepanov, D. Kostin, M. Krassilnikov, G. Kube, M. Kuhlmann, C. L. S. Lewis, L. Lilje, T. Limberg, D. Lipka, F. Löhl, H. Luna, M. Luong, M. Martins, M. Meyer, P. Michelato, V. Miltchev, W. D. Möller, L. Monaco, W. F. O. Müller, O. Napieralski, O. Napoly, P. Nicolosi, D. Nölle, T. Nuñez, A. Oppelt, C. Pagani, R. Paparella, N. Pchalek, J. Pedregosa-Gutierrez, B. Petersen, B. Petrosyan, G. Petrosyan, L. Petrosyan, J. Pflüger, E. Plönjes, L. Poletto, K. Pozniak, E. Prat, D. Proch, P. Pucyk, P. Radcliffe, H. Redlin, K. Rehlich, M. Richter, M. Roehrs, J. Roensch, R. Romaniuk, M. Ross, J. Rossbach, V. Rybnikov, M. Sachwitz, E. L. Saldin, W. Sandner, H. Schlarb, B. Schmidt, M. Schmitz, P. Schmüser, J. R. Schneider, E. A. Schneidmiller, S. Schnepp, S. Schreiber, M. Seidel, D. Sertore, A. V. Shabunov, C. Simon, S. Simrock, E. Sombrowski, A. A. Sorokin, P. Spanknebel, R. Spesyvtsev, L. Staykov, B. Steffen, F. Stephan, F. Stulle, H. Thom, K. Tiedtke, M. Tischer, S. Toleikis, R. Treusch, D. Trines, I. Tsakov, E. Vogel, T. Weiland, H. Weise, M. Wellhöfer, M. Wendt, I. Will, A. Winter, K. Wittenburg, W. Wurth, P. Yeates, M. V. Yurkov, I. Zagorodnov, K. Zapfe, *Nature Photonics* **2007**, *1*, 336–342.

[14] Z. Zhao, D. Wang, Q. Gu, L. Yin, M. Gu, Y. Leng, B. Liu, *Applied Sciences* **2017**, *7*, 607.

[15] S. Boutet, L. Lomb, G. J. Williams, T. R. M. Barends, A. Aquila, R. B. Doak, U. Weierstall, D. P. DePonte, J. Steinbrener, R. L. Shoeman, M. Messerschmidt, A. Barty, T. A. White, S. Kassemeyer, R. A. Kirian, M. M. Seibert, P. A. Montanez, C. Kenney, R. Herbst, P. Hart, J. Pines, G. Haller, S. M. Gruner, H. T. Philipp, M. W. Tate, M. Hromalik, L. J. Koerner, N. van Bakel, J. Morse, W. Ghonsalves, D. Arnlund, M. J. Bogan, C. Caleman, R. Fromme, C. Y. Hampton, M. S. Hunter, L. C. Johansson, G. Katona, C. Kupitz, M. Liang, A. V. Martin, K. Nass, L. Redecke, F. Stellato, N. Timneanu, D. Wang, N. A. Zatsepin, D. Schafer, J. Defever, R. Neutze, P. Fromme, J. C. H. Spence, H. N. Chapman, I. Schlichting, *Science* **2012**, *337*, 362–364.

[16] I. Schlichting, J. Miao, *Current Opinion in Structural Biology* **2012**, *22*, 613–626.

[17] H. N. Chapman, P. Fromme, A. Barty, T. A. White, R. A. Kirian, A. Aquila, M. S. Hunter, J. Schulz, D. P. DePonte, U. Weierstall, R. B. Doak, N. Coppola, R. L. Shoeman, S. W. Epp, R. Hartmann, A. Rudenko, L. Foucar, N. Kimmel, G. Weidenspointner, P. Holl, M. Liang, M. Barthelmess, C. Caleman, S. Boutet, M. J. Bogan, J. Krzywinski, C. Bostedt, S. Bajt, B. Rudek, B. Erk, C. Schmidt, A. Hömke, C. Reich, D. Pietschner, L. Strüder, G. Hauser, H. Gorke, J. Ullrich, S. Herrmann, G. Schaller, F. Schopper, K.-U. Kühnel, M. Messerschmidt, J. D. Bozek, S. P. Hau-Riege, M. Frank, C. Y. Hampton, R. G. Sierra, D. Starodub, J. Williams, J. Hajdu, N. Timneanu, M. M. Seibert, J. Andreasson, A. Rocker, O.

Jönsson, M. Svenda, S. Stern, K. Nass, C.-D. Schröter, F. Krasniqi, M. Bott, K. E. Schmidt, X. Wang, I. Grotjohann, J. M. Holton, T. R. M. Barends, S. Marchesini, R. Fromme, S. Schorb, D. Rupp, M. Adolph, T. Gorkhover, I. Andersson, H. Hirsemann, H. Graafsma, B. Nilsson, J. C. H. Spence, *Nature* **2011**, 13.

[18] R. Neutze, R. Wouts, D. van der Spoel, E. Weckert, J. Hajdu, **2000**, *406*, 752–757.

[19] T. Nakane, S. Hanashima, M. Suzuki, H. Saiki, T. Hayashi, K. Kakinouchi, S. Sugiyama, S. Kawatake, S. Matsuoka, N. Matsumori, E. Nango, J. Kobayashi, T. Shimamura, K. Kimura, C. Mori, N. Kunishima, M. Sugahara, Y. Takakyu, S. Inoue, T. Masuda, T. Hosaka, K. Tono, Y. Joti, T. Kameshima, T. Hatsui, M. Yabashi, T. Inoue, O. Nureki, S. Iwata, M. Murata, E. Mizohata, *Proc. Natl. Acad. Sci. USA* **2016**, *113*, 13039–13044.

[20] Z. Dauter, *Nat. Biotechnol.* **2004**, *22*, 1239–1240.

[21] A. Rudenko, L. Inhester, K. Hanasaki, X. Li, S. J. Robatjazi, B. Erk, R. Boll, K. Toyota, Y. Hao, O. Vendrell, C. Bomme, E. Savelyev, B. Rudek, L. Foucar, S. H. Southworth, C. S. Lehmann, B. Kraessig, T. Marchenko, M. Simon, K. Ueda, K. R. Ferguson, M. Bucher, T. Gorkhover, S. Carron, R. Alonso-Mori, J. E. Koglin, J. Correa, G. J. Williams, S. Boutet, L. Young, C. Bostedt, S.-K. Son, R. Santra, D. Rolles, *Nature* **2017**, *546*, 129–132.

[22] Y. Hao, L. Inhester, S.-K. Son, R. Santra, *Physical Review A* **2019**, *100*, 013402.

[23] Y. Hao, L. Inhester, K. Hanasaki, S.-K. Son, R. Santra, *Structural Dynamics* **2015**, *2*, 041707.

[24] S.-K. Son, L. Young, R. Santra, *Physical Review A* **2011**, *83*, 033402.

[25] J. C. Slater, *Physical Review* **1951**, *81*, 385–390.

[26] J. M. Schäfer, L. Inhester, S.-K. Son, R. F. Fink, R. Santra, *Physical Review A* **2018**, *97*, 053415.

[27] L. Inhester, K. Hanasaki, Y. Hao, S.-K. Son, R. Santra, *Physical Review A* **2016**, *94*, 023422.

[28] W. J. Veigele, *Atomic Data* **1973**, *5*, 51–111.

[29] J. H. Hubbell, W. J. Veigele, E. A. Briggs, R. T. Brown, D. T. Cromer, R. J. Howerton, *Journal of Physical and Chemical Reference Data* **1975**, *4*, 471–538.

[30] H. N. Chapman, A. Barty, M. J. Bogan, S. Boutet, M. Frank, S. P. Hau-Riege, S. Marchesini, B. W. Woods, S. Bajt, W. H. Benner, R. A. London, E. Plönjes, M. Kuhlmann, R. Treusch, S. Düsterer, T. Tschentscher, J. R. Schneider, E. Spiller, T. Möller, C. Bostedt, M. Hoener, D. A. Shapiro, K. O. Hodgson, D. van der Spoel, F. Burmeister, M. Bergh, C. Caleman, G. Huldt, M. M. Seibert, F. R. N. C. Maia, R. W. Lee, A. Szöke, N. Timneanu, J. Hajdu, *Nature Physics* **2006**, *2*, 839–843.

[31] A. Barty, C. Caleman, A. Aquila, N. Timneanu, L. Lomb, T. A. White, J. Andreasson, D. Arnlund, S. Bajt, T. R. M. Barends, M. Barthelmess, M. J. Bogan, C. Bostedt, J. D. Bozek, R. Coffee, N. Coppola, J. Davidsson, D. P. DePonte, R. B. Doak, T. Ekeberg, V. Elser, S. W. Epp, B. Erk, H. Fleckenstein, L. Foucar, P. Fromme, H. Graafsma, L. Gumprecht, J. Hajdu, C. Y. Hampton, R. Hartmann, A. Hartmann, G. Hauser, H. Hirsemann, P. Holl, M. S. Hunter, L. Johansson, S. Kassemeyer, N. Kimmel, R. A. Kirian, M. Liang, F. R. N. C. Maia, E. Malmerberg, S. Marchesini, A. V. Martin, K. Nass, R. Neutze, C. Reich, D. Rolles, B. Rudek, A. Rudenko, H. Scott, I. Schlichting, J. Schulz, M. M. Seibert, R. L. Shoeman, R. G. Sierra, H. Soltau, J. C. H. Spence, F. Stellato, S. Stern, L. Strüder, J. Ullrich, X. Wang, G. Weidenspointner, U. Weierstall, C. B. Wunderer, H. N. Chapman, *Nature Photonics* **2012**, *6*, 35–40.

[32] B. Erk, D. Rolles, L. Foucar, B. Rudek, S. W. Epp, M. Cryle, C. Bostedt, S. Schorb, J. Bozek, A. Rouzee, A. Hundertmark, T. Marchenko, M. Simon, F. Filsinger, L. Christensen, S. De, S. Trippel, J. Küpper, H. Stapelfeldt, S. Wada, K. Ueda, M. Swiggers, M. Messerschmidt, C. D. Schröter, R. Moshammer, I. Schlichting, J. Ullrich, A. Rudenko, *Physical Review Letters* **2013**, *110*, 053003.

[33] B. Erk, D. Rolles, L. Foucar, B. Rudek, S. W. Epp, M. Cryle, C. Bostedt, S. Schorb, J. Bozek, A. Rouzee, A. Hundertmark, T. Marchenko, M. Simon, F. Filsinger, L. Christensen, S. De, S. Trippel, J. Küpper, H. Stapelfeldt, S. Wada, K. Ueda, M. Swiggers, M. Messerschmidt, C. D. Schröter, R. Moshammer, I. Schlichting, J. Ullrich, A. Rudenko, *Journal of Physics B: Atomic Molecular and Optical Physics* **2013**, *46*, 164031.

[34] B. Erk, R. Boll, S. Trippel, D. Anielski, L. Foucar, B. Rudek, S. W. Epp, R. Coffee, S. Carron, S. Schorb, K. R. Ferguson, M. Swiggers, J. D. Bozek, M. Simon, T. Marchenko, J. Kupper, I. Schlichting, J. Ullrich, C. Bostedt, D. Rolles, A. Rudenko, *Science* **2014**, *345*, 288–291.

[35] R. Boll, B. Erk, R. Coffee, S. Trippel, T. Kierspel, C. Bomme, J. D. Bozek, M. Burkett, S. Carron, K. R. Ferguson, L. Foucar, J. Küpper, T. Marchenko, C. Miron, M. Patanen, T. Osipov, S. Schorb, M. Simon, M. Swiggers, S. Techert, K. Ueda, C. Bostedt, D. Rolles, A. Rudenko, *Structural Dynamics* **2016**, *3*, 043207.

[36] A. Ramadhan, Master's thesis, University of Waterloo, Waterloo, Canada, **2017**.

[37] J. Gagnon, K. F. Lee, D. M. Rayner, P. B. Corkum, V. R. Bhardwaj, *Journal of Physics B: Atomic Molecular and Optical Physics* **2008**, *41*, 215104.

[38] M. J. Gaillard, D. S. Gemmell, G. Goldring, I. Levine, W. J. Pietsch, J. C. Poizat, A. J. Ratkowski, J. Remillieux, Z. Vager, B. J. Zabransky, *Physical Review A* **1978**, *17*, 1797–1803.

[39] M. Kunitski, S. Zeller, J. Voigtsberger, A. Kalinin, L. P. H. Schmidt, M. Schöffler, A. Czasch, W. Schöllkopf, R. E. Grisenti, T. Jahnke, D. Blume, R. Dörner, *Science* **2015**, *348*, 551–555.

[40] F. Légaré, K. F. Lee, I. V. Litvinyuk, P. W. Dooley, S. S. Wesolowski, P. R. Bunker, P. Dombi, F. Krausz, A. D. Bandrauk, D. M. Villeneuve, P. B. Corkum, *Physical Review A* **2005**, *71*, 013415.

[41] W. Zhou, L. Ge, G. A. Cooper, S. W. Crane, M. H. Evans, M. N. R. Ashfold, C. Vallance, *The Journal of Chemical Physics* **2020**, *153*, 184201.

[42] I. Last, I. Schek, J. Jortner, *The Journal of Chemical Physics* **1997**, *107*, 6685–6692.

[43] L. Poth, A. W. Castleman, *The Journal of Physical Chemistry A* **1998**, *102*, 4075–4081.

[44] E. Bringa, *Nuclear Instruments and Methods in Physics Research Section B: Beam Interactions with Materials and Atoms* **2003**, *209*, 1–8.

[45] K. Nagaya, K. Motomura, E. Kukk, H. Fukuzawa, S. Wada, T. Tachibana, Y. Ito, S. Mondal, T. Sakai, K. Matsunami, R. Koga, S. Ohmura, Y. Takahashi, M. Kanno, A. Rudenko, C. Nicolas, X.-J. Liu, Y. Zhang, J. Chen, M. Anand, Y. H. Jiang, D.-E. Kim, K. Tono, M. Yabashi, H. Kono, C. Miron, M. Yao, K. Ueda, *Physical Review X* **2016**, *6*, 021035.

[46] Z. Vager, R. Naaman, E. P. Kanter, *Science* **1989**, *244*, 426–431.

[47] J. H. Sanderson, T. Nishide, H. Shiromaru, Y. Achiba, N. Kobayashi, *Physical Review A* **1999**, *59*, 4817–4820.

[48] M. Tarisien, L. Adoui, F. Frémont, D. Lelièvre, L. Guillaume, J.-Y. Chesnel, H. Zhang, A. Dubois, D. Mathur, S. Kumar, M. Krishnamurthy, A. Cassimi, *Journal of Physics B: Atomic Molecular and Optical Physics* **2000**, *33*, L11–L20.

[49] T. Kitamura, T. Nishide, H. Shiromaru, Y. Achiba, N. Kobayashi, *The Journal of Chemical Physics* **2001**, *115*, 5–6.

[50] H. Stapelfeldt, E. Constant, H. Sakai, P. B. Corkum, *Physical Review A* **1998**, *58*, 426–433.

[51] T. Yatsuhashi, N. Nakashima, *Journal of Photochemistry and Photobiology C: Photochemistry Reviews* **2018**, *34*, 52–84.

[52] M. Pitzer, M. Kunitski, A. S. Johnson, T. Jahnke, H. Sann, F. Sturm, L. P. H. Schmidt, H. Schmidt-Böcking, R. Dörner, J. Stohner, J. Kiedrowski, M. Reggelin, S. Marquardt, A. Schießer, R. Berger, M. S. Schöffler, *Science* **2013**, *341*, 1096–1100.

[53] M. Pitzer, G. Kastirke, M. Kunitski, T. Jahnke, T. Bauer, C. Goihl, F. Trinter, C. Schober, K. Henrichs, J. Becht, S. Zeller, H. Gassert, M. Waitz, A. Kuhlins, H. Sann, F. Sturm, F. Wiegandt, R. Wallauer, L. P. H. Schmidt, A. S. Johnson, M. Mazenauer, B. Spenger, S. Marquardt, S. Marquardt, H. Schmidt-Böcking, J. Stohner, R. Dörner, M. Schöffler, R. Berger, *ChemPhysChem* **2016**, *17*, 2465–2472.

[54] L. Young, E. P. Kanter, B. Krässig, Y. Li, A. M. March, S. T. Pratt, R. Santra, S. H. Southworth, N. Rohringer, L. F. DiMauro, G. Doumy, C. A. Roedig, N. Berrah, L. Fang, M. Hoener, P. H. Bucksbaum, J. P. Cryan, S. Ghimire, J. M. Glownia, D. A. Reis, J. D. Bozek, C. Bostedt, M. Messerschmidt, *Nature* **2010**, *466*, 56–61.

[55] C. A. Schouder, A. S. Chatterley, L. B. Madsen, F. Jensen, H. Stapelfeldt, *Physical Review A* **2020**, *102*, 063125.

[56] E. Kukk, K. Motomura, H. Fukuzawa, K. Nagaya, K. Ueda, *Applied Sciences* **2017**, *7*, 531.

[57] J. Ullrich, R. Moshammer, A. Dorn, R. Dörner, L. P. H. Schmidt, H. Schmidt-Böcking, *Reports on Progress in Physics* **2003**, *66*, 1463–1545.

[58] Z. Jurek, S.-K. Son, B. Ziaja, R. Santra, *Journal of Applied Crystallography* **2016**, *49*, 1048–1056.

[59] Y. Kumagai, Z. Jurek, W. Xu, H. Fukuzawa, K. Motomura, D. Iablonskyi, K. Nagaya, S.-i. Wada, S. Mondal, T. Tachibana, Y. Ito, T. Sakai, K. Matsunami, T. Nishiyama, T. Umemoto, C. Nicolas, C. Miron, T. Togashi, K. Ogawa, S. Owada, K. Tono, M. Yabashi, S.-K. Son, B. Ziaja, R. Santra, K. Ueda, *Physical Review Letters* **2018**, *120*, 223201.

[60] N. Berrah, A. Sanchez-Gonzalez, Z. Jurek, R. Obaid, H. Xiong, R. J. Squibb, T. Osipov, A. Lutman, L. Fang, T. Barillot, J. D. Bozek, J. Cryan, T. J. A. Wolf, D. Rolles, R. Coffee, K. Schnorr, S. Augustin, H. Fukuzawa, K. Motomura, N. Niebuhr, L. J. Frasinski, R. Feifel, C. P. Schulz, K. Toyota, S.-K. Son, K. Ueda, T. Pfeifer, J. P. Marangos, R. Santra, *Nature Physics* **2019**, *15*, 1279–1283.

[61] H. Ryufuku, K. Sasaki, T. Watanabe, *Physical Review A* **1980**, *21*, 745–750.

[62] R. R. Zope, B. I. Dunlap, *Journal of Chemical Theory and Computation* **2005**, *1*, 1195–1200.

[63] W. Heijser, A. T. van Kessel, E. J. Baerends, *Chemical Physics* **1976**, *16*, 371–379.

[64] B. Santra, Doctoral Thesis, Technische Universität Berlin, Fakultät II - Mathematik und Naturwissenschaften, Berlin, Germany, **2010**.

[65] I. N. Yakovkin, P. A. Dowben, *Surface Review and Letters* **2007**, *14*, 481–487.

[66] J. C. Slater, T. M. Wilson, J. H. Wood, *Physical Review* **1969**, *179*, 28–38.

[67] G. J. M. Velders, D. Feil, *Theoretica Chimica Acta* **1993**, *86*, 391–416.

[68] A. D. Becke, *The Journal of Chemical Physics* **2014**, *140*, 18A301.

[69] C. C. J. Roothaan, *Rev. Mod. Phys.* **1951**, *23*, 69–89.

[70] A. T. B. Gilbert, N. A. Besley, P. M. W. Gill, *The Journal of Physical Chemistry A* **2008**, *112*, 13164–13171.

[71] J. Reinhold, *Quantentheorie der Moleküle: Eine Einführung*, Springer Fachmedien Wiesbaden, **2015**.

[72] E. Cancès in *Mathematical Models and Methods for Ab Initio Quantum Chemistry*, Springer Berlin Heidelberg, Berlin, Heidelberg, **2000**, pp. 17–43.

[73] A. Rauk in *Orbital Interaction Theory of Organic Chemistry*, John Wiley & Sons, Ltd., **2000**, pp. 218–246.

[74] G. M. J. Barca, A. T. B. Gilbert, P. M. W. Gill, *The Journal of Chemical Physics* **2014**, *141*, 111104.

[75] T. Koopmans, *Physica* **1934**, *1*, 104–113.

[76] R. Santra, *Journal of Physics B: Atomic Molecular and Optical Physics* **2008**, *42*, 023001; Corrected in R. Santra, *Journal of Physics B: Atomic Molecular and Optical Physics* **2009**, *42*, 169801.

[77] K. Takahashi, Lecture notes in Computational Materials Science, Part II, `https://www.phys.sinica.edu.tw/TIGP-NANO/Course/2013_Spring/ClassNote/CMS_20130509.pdf`, Accessed: 2020-12-27, **2013**.

[78] A. Szabo, N. S. Ostlund, *Modern Quantum Chemistry: Introduction to Advanced Electronic Structure Theory*, First Edition, Dover Publications, Inc., Mineola, New York, **1996**, pp. 67–68.

[79] M. Piris, J. M. Matxain, X. Lopez, J. M. Ugalde, *The Journal of Chemical Physics* **2012**, *136*, 174116.

[80] V. Lee, *Organosilicon Compounds: Experiment (Physico-Chemical Studies) and Applications*, Academic Press, Elsevier Science, Cambridge, MA, **2017**.

[81] A. Rosén, D. E. Ellis, H. Adachi, F. W. Averill, **1976**, *65*, 7.

[82] F. Herman, S. Skillman, *Atomic Structure Calculations*, Englewood Cliffs, NJ: Prentice-Hall, **1963**.

[83] A. C. Thompson, D. Vaughan, *X-ray Data Booklet*, Center for X-ray Optics and Advanced Light Source, Lawrence Berkeley National Laboratory, Berkeley, CA, **2001**.

[84] G. Doumy, C. Roedig, S.-K. Son, C. I. Blaga, A. D. DiChiara, R. Santra, N. Berrah, C. Bostedt, J. D. Bozek, P. H. Bucksbaum, J. P. Cryan, L. Fang, S. Ghimire, J. M. Glownia, M. Hoener, E. P. Kanter, B. Krässig, M. Kuebel, M. Messerschmidt, G. G. Paulus, D. A. Reis, N. Rohringer, L. Young, P. Agostini, L. F. DiMauro, *Physical Review Letters* **2011**, *106*, 083002.

[85] K. Tamasaku, E. Shigemasa, Y. Inubushi, T. Katayama, K. Sawada, H. Yumoto, H. Ohashi, H. Mimura, M. Yabashi, K. Yamauchi, T. Ishikawa, *Nature Photonics* **2014**, *8*, 313–316.

[86] R. Santra, L. Young in *Synchrotron Light Sources and Free-Electron Lasers*, (Eds.: E. Jaeschke, S. Khan, J. R. Schneider, J. B. Hastings), Springer International Publishing, Switzerland, **2016**, pp. 1233–1260.

[87] N. Rohringer, R. Santra, *Physical Review A* **2007**, *76*, 033416.

[88] M. G. Makris, P. Lambropoulos, A. Mihelič, *Physical Review Letters* **2009**, *102*, 033002.

[89] M. Quack, *The Journal of Chemical Physics* **1978**, *69*, 1282–1307.

[90] S. Mukamel, *The Journal of Chemical Physics* **1979**, *71*, 2012–2020.

[91] H. Breuer, P. Breuer, F. Petruccione, S. Petruccione, *The Theory of Open Quantum Systems*, Oxford University Press, Oxford, **2002**.

[92] R. N. Coffee, J. P. Cryan, J. Duris, W. Helml, S. Li, A. Marinelli, *Philosophical Transactions of the Royal Society A: Mathematical Physical and Engineering Sciences* **2019**, *377*, 20180386.

[93] Y. Inubushi, I. Inoue, J. Kim, A. Nishihara, S. Matsuyama, H. Yumoto, T. Koyama, K. Tono, H. Ohashi, K. Yamauchi, M. Yabashi, *Applied Sciences* **2017**, *7*, 584.

[94] C. Behrens, F.-J. Decker, Y. Ding, V. A. Dolgashev, J. Frisch, Z. Huang, P. Krejcik, H. Loos, A. Lutman, T. J. Maxwell, J. Turner, J. Wang, M.-H. Wang, J. Welch, J. Wu, *Nature Communications* **2014**, *5*, 3762.

[95] K. Toyota, Z. Jurek, S.-K. Son, H. Fukuzawa, K. Ueda, N. Berrah, B. Rudek, D. Rolles, A. Rudenko, R. Santra, *Journal of Synchrotron Radiation* **2019**, *26*, 1017–1030.

[96] S.-K. Son, H. N. Chapman, R. Santra, *Physical Review Letters* **2011**, *107*, 218102.

[97] J. M. Slowik, S.-K. Son, G. Dixit, Z. Jurek, R. Santra, *New Journal of Physics* **2014**, *16*, 073042.

[98] B. Rudek, S.-K. Son, L. Foucar, S. W. Epp, B. Erk, R. Hartmann, M. Adolph, R. Andritschke, A. Aquila, N. Berrah, C. Bostedt, J. Bozek, N. Coppola, F. Filsinger, H. Gorke, T. Gorkhover, H. Graafsma, L. Gumprecht, A. Hartmann, G. Hauser, S. Herrmann, H. Hirsemann, P. Holl, A. Hömke, L. Journel, C. Kaiser, N. Kimmel, F. Krasniqi, K.-U. Kühnel, M. Matysek, M. Messerschmidt, D. Miesner, T. Möller, R. Moshammer, K. Nagaya, B. Nilsson, G. Potdevin, D. Pietschner, C. Reich, D. Rupp, G. Schaller, I. Schlichting, C. Schmidt, F. Schopper, S. Schorb, C.-D. Schröter, J. Schulz, M. Simon, H. Soltau, L. Strüder, K. Ueda, G. Weidenspointner, R. Santra, J. Ullrich, A. Rudenko, D. Rolles, *Nature Photonics* **2012**, *6*, 858–865.

[99] B. Rudek, D. Rolles, S.-K. Son, L. Foucar, B. Erk, S. Epp, R. Boll, D. Anielski, C. Bostedt, S. Schorb, R. Coffee, J. Bozek, S. Trippel, T. Marchenko, M. Simon, L. Christensen, S. De, S.-i. Wada, K. Ueda, I. Schlichting, R. Santra, J. Ullrich, A. Rudenko, *Physical Review A* **2013**, *87*, 023413.

[100] H. Fukuzawa, S.-K. Son, K. Motomura, S. Mondal, K. Nagaya, S. Wada, X.-J. Liu, R. Feifel, T. Tachibana, Y. Ito, M. Kimura, T. Sakai, K. Matsunami, H. Hayashita, J. Kajikawa, P. Johnsson, M. Siano, E. Kukk, B. Rudek, B. Erk, L. Foucar, E. Robert, C. Miron, K. Tono, Y. Inubushi, T. Hatsui, M. Yabashi, M. Yao, R. Santra, K. Ueda, *Physical Review Letters* **2013**, *110*, 173005.

[101] K. Motomura, H. Fukuzawa, S.-K. Son, S. Mondal, T. Tachibana, Y. Ito, M. Kimura, K. Nagaya, T. Sakai, K. Matsunami, S. Wada, H. Hayashita, J. Kajikawa, X.-J. Liu, R. Feifel, P. Johnsson, M. Siano, E. Kukk, B. Rudek, B. Erk, L. Foucar, E. Robert, C. Miron, K. Tono, Y. Inubushi, T. Hatsui, M. Yabashi, M. Yao, R. Santra, K. Ueda, *Journal of Physics B: Atomic Molecular and Optical Physics* **2013**, *46*, 164024.

[102] S.-K. Son, R. Santra, *Physical Review A* **2012**, *85*, 063415.

[103] Z. Jurek, R. Santra, S.-K. Son, B. Ziaja, *XRAYPAC - a Software Package for Modeling X-ray-Induced Dynamics of Matter*, `http://www.desy.de/~xraypac/`, version 1.0, Hamburg, Germany: CFEL, DESY, **2016**.

[104] X. Li, L. Inhester, S. J. Robatjazi, B. Erk, R. Boll, K. Hanasaki, K. Toyota, Y. Hao, C. Bomme, B. Rudek, L. Foucar, S. H. Southworth, C. S. Lehmann, B. Kraessig, T. Marchenko, M. Simon, K. Ueda, K. R. Ferguson, M. Bucher, T. Gorkhover, S. Carron, R. Alonso-Mori, J. E. Koglin, J. Correa, G. J. Williams, S. Boutet, L. Young, C. Bostedt, S.-K. Son, R. Santra, D. Rolles, A. Rudenko, *Physical Review Letters* **2021**, *127*, 093202.

[105] X. Li, L. Inhester, T. Osipov, R. Boll, R. Coffee, J. Cryan, A. Gatton, T. Gorkhover, G. Hartman, M. Ilchen, A. Knie, M.-F. Lin, M. P. Minitti, C. Weninger, T. J. A. Wolf, S.-K. Son, R. Santra, D. Rolles, A. Rudenko, P. Walter, *Scientific Reports* **2021**, *11*, 505.

[106] M. Brosolo, P. Decleva, *Chemical Physics* **1992**, *159*, 185–196.

[107] P. V. Demekhin, A. Ehresmann, V. L. Sukhorukov, *The Journal of Chemical Physics* **2011**, *134*, 024113.

[108] H. Siegbahn, L. Asplund, P. Kelfve, *Chemical Physics Letters* **1975**, *35*, 330–335.

[109] E. Z. Chelkowska, F. P. Larkins, *Atomic Data and Nuclear Data Tables* **1991**, *49*, 121–206.

[110] M. Coville, T. D. Thomas, *Physical Review A* **1991**, *43*, 6053–6056.

[111] M. H. Chen, F. P. Larkins, B. Crasemann, *Atomic Data and Nuclear Data Tables* **1990**, *45*, 1–205.

[112] D. L. Walters, C. P. Bhalla, *Physical Review A* **1971**, *3*, 1919–1927.

[113] R. F. Fink, *Journal of Electron Spectroscopy and Related Phenomena* **1995**, *76*, 295–300.

[114] B. F. Murphy, T. Osipov, Z. Jurek, L. Fang, S.-K. Son, M. Mucke, J. Eland, V. Zhaunerchyk, R. Feifel, L. Avaldi, P. Bolognesi, C. Bostedt, J. D. Bozek, J. Grilj, M. Guehr, L. J. Frasinski, J. Glownia, D. T. Ha, K. Hoffmann, E. Kukk, B. K. McFarland, C. Miron, E. Sistrunk, R. J. Squibb, K. Ueda, R. Santra, N. Berrah, *Nature Communications* **2014**, *5*, 4281.

[115] N. Berrah, L. Fang, T. Osipov, Z. Jurek, B. F. Murphy, R. Santra, *Faraday Discuss.* **2014**, *171*, 471–485.

[116] L. Fang, Z. Jurek, T. Osipov, B. F. Murphy, R. Santra, N. Berrah, *Journal of Physics: Conference Series* **2015**, *601*, 012006.

[117] T. Tachibana, Z. Jurek, H. Fukuzawa, K. Motomura, K. Nagaya, S. Wada, P. Johnsson, M. Siano, S. Mondal, Y. Ito, M. Kimura, T. Sakai, K. Matsunami, H. Hayashita, J. Kajikawa, X.-J. Liu, E. Robert, C. Miron, R. Feifel, J. P. Marangos, K. Tono, Y. Inubushi, M. Yabashi, S.-K. Son, B. Ziaja, M. Yao, R. Santra, K. Ueda, *Scientific Reports* **2015**, *5*, 10977.

[118] R. Jin, Limitations of the present electron transfer model, Internal report, CFEL-DESY Theory Division, **2020**.

[119] M. W. Schmidt, K. K. Baldridge, J. A. Boatz, S. T. Elbert, M. S. Gordon, J. H. Jensen, S. Koseki, N. Matsunaga, K. A. Nguyen, S. Su, T. L. Windus, M. Dupuis, J. A. Montgomery, *Journal of Computational Chemistry* **1993**, *14*, 1347–1363.

[120] V. Sortur, J. Yenagi, J. Tonannavar, *Spectrochimica Acta Part A: Molecular and Biomolecular Spectroscopy* **2008**, *69*, 604–611.

[121] R. S. Mulliken, *The Journal of Chemical Physics* **1955**, *23*, 1833–1840.

[122] H. Offermanns, *Nachrichten aus der Chemie* **2011**, *59*, 1152–1153.

[123] M. Hoener, L. Fang, O. Kornilov, O. Gessner, S. T. Pratt, M. Gühr, E. P. Kanter, C. Blaga, C. Bostedt, J. D. Bozek, P. H. Bucksbaum, C. Buth, M. Chen, R. Coffee, J. Cryan, L. DiMauro, M. Glownia, E. Hosler, E. Kukk, S. R. Leone, B. McFarland, M. Messerschmidt, B. Murphy, V. Petrovic, D. Rolles, N. Berrah, *Physical Review Letters* **2010**, *104*, 253002.

[124] J. W. Verhoeven, *Pure and Applied Chemistry* **1996**, *68*, 2223–2286.

[125] M. Obermeyer, Master's thesis, Universität Hamburg, Germany, **2020**.

[126] M. Obermeyer, L. Inhester, R. Santra, *Physical Review A* **2021**, *104*, 023115.

[127] R. Boll, J. M. Schäfer, B. Richard, K. Fehre, G. Kastirke, Z. Jurek, M. S. Schöffler, M. M. Abdullah, N. Anders, T. M. Baumann, S. Eckart, B. Erk, A. De Fanis, R. Dörner, S. Grundmann, P. Grychtol, A. Hartung, M. Hofmann, M. Ilchen, L. Inhester, C. Janke, R. Jin, M. Kircher, K. Kubicek, M. Kunitski, X. Li, T. Mazza, S. Meister, N. Melzer, J. Montano, V. Music, G. Nalin, Y. Ovcharenko, C. Passow, A. Pier, N. Rennhack, J. Rist, D. E. Rivas, D. Rolles, I. Schlichting, L. P. H. Schmidt, P. Schmidt, J. Siebert, N. Strenger, D. Trabert, F. Trinter, I. Vela-Perez, R. Wagner, P. Walter, M. Weller, P. Ziolkowski, S.-K. Son, A. Rudenko, M. Meyer, R. Santra, T. Jahnke, *Nature Physics* **2022**, *18*, DOI `10.1038/s41567-022-01507-0`.

[128] M. L. Grünbein, J. Bielecki, A. Gorel, M. Stricker, R. Bean, M. Cammarata, K. Dörner, L. Fröhlich, E. Hartmann, S. Hauf, M. Hilpert, Y. Kim, M. Kloos, R. Letrun, M. Messerschmidt, G. Mills, G. Nass Kovacs, M. Ramilli, C. M. Roome, T. Sato, M. Scholz, M. Sliwa, J. Sztuk-Dambietz, M. Weik, B. Weinhausen, N. Al-Qudami, D. Boukhelef, S. Brockhauser, W. Ehsan, M. Emons, S. Esenov, H. Fangohr, A. Kaukher, T. Kluyver, M. Lederer, L. Maia, M. Manetti, T. Michelat, A. Münnich, F. Pallas, G. Palmer, G. Previtali, N. Raab, A. Silenzi, J. Szuba,

S. Venkatesan, K. Wrona, J. Zhu, R. B. Doak, R. L. Shoeman, L. Foucar, J.-P. Colletier, A. P. Mancuso, T. R. M. Barends, C. A. Stan, I. Schlichting, *Nature Communications* **2018**, *9*, 3487.

[129] J. P. Valleau, J. M. Deckers, *Canadian Journal of Chemistry* **1965**, *43*, 6–17.

[130] R. Boll, Mutliple ionization of rare gases and photo-induced dynamics of ring-type molecules, Slideshow presented at Science@FELs 2020, online conference, **2020**.

[131] K. Amini, R. Boll, A. Lauer, M. Burt, J. W. L. Lee, L. Christensen, F. Brauβe, T. Mullins, E. Savelyev, U. Ablikim, N. Berrah, C. Bomme, S. Düsterer, B. Erk, H. Höppner, P. Johnsson, T. Kierspel, F. Krecinic, J. Küpper, M. Müller, E. Müller, H. Redlin, A. Rouzée, N. Schirmel, J. Thøgersen, S. Techert, S. Toleikis, R. Treusch, S. Trippel, A. Ulmer, J. Wiese, C. Vallance, A. Rudenko, H. Stapelfeldt, M. Brouard, D. Rolles, *The Journal of Chemical Physics* **2017**, *147*, 013933.

[132] N. Feinstein, Efficient and Quantitative Simulation of Charge-Rearrangement-Enhanced X-ray Ionization of Molecules, Durham University, CFEL-DESY Theory Division, **2017**.

[133] M. E. Corrales, G. Gitzinger, J. González-Vázquez, V. Loriot, R. de Nalda, L. Bañares, *The Journal of Physical Chemistry A* **2012**, *116*, 2669–2677.

[134] Y. Hahn in *Atomic and Molecular Processes in Fusion Edge Plasmas*, (Ed.: R. K. Janev), Springer US, Boston, MA, **1995**, pp. 91–117.

[135] M. C. Böhm, *Zeitschrift für Naturforschung A* **1981**, *36*, 1205–1212.

[136] H.-J. Werner, P. J. Knowles, MOLPRO Users Manual Version 2015.1, `https://www.molpro.net/info/2015.1/doc/manual/node178.html`, Accessed: 2021-06-07, **2015**.

[137] K. Nass, A. Gorel, M. M. Abdullah, A. V. Martin, M. Kloos, A. Marinelli, A. Aquila, T. R. M. Barends, F.-J. Decker, R. Bruce Doak, L. Foucar, E. Hartmann, M. Hilpert, M. S. Hunter, Z. Jurek, J. E. Koglin, A. Kozlov, A. A. Lutman, G. N. Kovacs, C. M. Roome, R. L. Shoeman, R. Santra, H. M. Quiney, B. Ziaja, S. Boutet, I. Schlichting, *Nature Communications* **2020**, *11*, 1814.

[138] J. Adler, O. Öktem, *Inverse Problems* **2017**, *33*, 124007.

[139] P. Di Cintio, U. Saalmann, J.-M. Rost, *Physical Review Letters* **2013**, *111*, 123401.

[140] J. C. Slater, *The Journal of Chemical Physics* **1964**, *41*, 3199–3204.

[141] G. Cowan, Recommendations for presentation of error bars, Presentation at ATLAS Statistics Forum, `http://www.pp.rhul.ac.uk/~cowan/atlas/ErrorBars.pdf`, Accessed: 2021-06-18, **2011**.

[142] J. E. Subotnik, A. Jain, B. Landry, A. Petit, W. Ouyang, N. Bellonzi, *Annual Review of Physical Chemistry* **2016**, *67*, 387–417.

[143] H. H. Jaffe, A. L. Miller, *Journal of Chemical Education* **1966**, *43*, 469.

[144] P. Yoo, M. Sakano, S. Desai, M. M. Islam, P. Liao, A. Strachan, *npj Computational Materials* **2021**, *7*, 9.

[145] T. P. Senftle, S. Hong, M. M. Islam, S. B. Kylasa, Y. Zheng, Y. K. Shin, C. Junkermeier, R. Engel-Herbert, M. J. Janik, H. M. Aktulga, T. Verstraelen, A. Grama, A. C. T. van Duin, *npj Computational Materials* **2016**, *2*, 15011.

[146] D. Furman, D. J. Wales, *The Journal of Chemical Physics* **2020**, *153*, 021102.

[147] S. Düsterer, P. Radcliffe, C. Bostedt, J. Bozek, A. L. Cavalieri, R. Coffee, J. T. Costello, D. Cubaynes, L. F. DiMauro, Y. Ding, G. Doumy, F. Grüner, W. Helml, W. Schweinberger, R. Kienberger, A. R. Maier, M. Messerschmidt, V. Richardson, C. Roedig, T. Tschentscher, M. Meyer, *New Journal of Physics* **2011**, *13*, 093024.

[148] C. Vallance, Solving the Secular Equations, `https://chem.libretexts.org/@go/page/9344`, Accessed: 2021-09-13, **2020**.

[149] C. Arnold, O. Vendrell, R. Santra, *Physical Review A* **2017**, *95*, 033425.

[150] F. Matthias Bickelhaupt, U. Radius, A. W. Ehlers, R. Hoffmann, E. Jan Baerends, *New J. Chem.* **1998**, *22*, 1–3.

[151] A. Föhlisch, P. Feulner, F. Hennies, A. Fink, D. Menzel, D. Sanchez-Portal, P. M. Echenique, W. Wurth, *Nature* **2005**, *436*, 373–376.

[152] C. Zhou, Y. Bai, L. Song, Y. Zeng, Y. Xu, D. Zhang, X. Lu, Y. Leng, J. Liu, Y. Tian, R. Li, Z. Xu, *Nature Photonics* **2021**, *15*, 216–221.

[153] K.-H. Gericke, Das Wasserstoffmolekül-Ion $H_2^+$, `http://www.pci.tu-bs.de/aggericke/PC4/Kap_II/H2-Ion.htm`, Accessed: 2021-10-11, **2015**.

[154] L. J. Schaad, W. V. Hicks, *The Journal of Chemical Physics* **1970**, *53*, 851–852.

[155] G. Sansone, F. Kelkensberg, J. F. Pérez-Torres, F. Morales, M. F. Kling, W. Siu, O. Ghafur, P. Johnsson, M. Swoboda, E. Benedetti, F. Ferrari, F. Lépine, J. L. Sanz-Vicario, S. Zherebtsov, I. Znakovskaya, A. L'Huillier, M. Y. Ivanov, M. Nisoli, F. Martín, M. J. J. Vrakking, *Nature* **2010**, *465*, 763–766.

[156] F. Calegari, D. Ayuso, A. Trabattoni, L. Belshaw, S. De Camillis, S. Anumula, F. Frassetto, L. Poletto, A. Palacios, P. Decleva, J. B. Greenwood, F. Martin, M. Nisoli, *Science* **2014**, *346*, 336–339.

[157] C. Arnold, C. Larivière-Loiselle, K. Khalili, L. Inhester, R. Welsch, R. Santra, *Journal of Physics B: Atomic Molecular and Optical Physics* **2020**, *53*, 164006.

# *Acknowledgements*

First of all, I am grateful to my supervisor Robin Santra, for guidance and for the many things he taught me. In particular, I thank you for the long, inspiring discussions with connected minds we sometimes had.

Next, I would like to thank Ludger Inhester for also teaching me a lot, for coming back, and for always being ready for a sophisticated discussion, be it on the way to the canteen or after some beers. Thank you for always caring about me, for careful proofreading and for being so reliable.

My special gratitude goes to my mentor Simone Techert for her appreciative openness, for encouragement and for sharing her enthusiasm for science. You are as cool as Tara Brabazon.

I would like to thank Till Jahnke for explanations on the experiment, which were always motivating. Also for sometimes writing the right email at the right time. It has been great to work with you, as you are a good team player.

My thanks go to Zoltan Jurek for tremendous help with technical issues. For helpful discussions and guidance I thank Sang-Kil Son. Thanks are also due to Benoît Richard, Malik M. Abdullah and Rui Jin for assistance with the CEI project. I thank Rebecca Boll for the collaboration and the chance to take part in an XFEL beam time.

I would like to thank Daria Kolbasova, Caroline Arnold, Yashoj Shakya, Rajwant Kaur, Otfried Geffert and all other members of the CFEL-DESY Theory Division for the good times we had. I am grateful for getting to know so many nice and gifted people from all over the world.

Essential were also Hildir, carrying me through the Ph.D., and the community in HafengeBEAT. Finally, my thanks go to my family and friends for their support, fun and the necessary distraction.

Diese Arbeit wurde im Zeitraum von Oktober 2017 bis Oktober 2021 in der CFEL-DESY Theory Division unter Leitung von Prof. Dr. Robin Santra in Hamburg angefertigt.

# Eidesstattliche Erklärung

Hiermit versichere ich an Eides statt, die vorliegende Dissertation selbst verfasst und keine anderen als die angegebenen Hilfsmittel benutzt zu haben. Die eingereichte schriftliche Fassung entspricht der auf dem elektronischen Speichermedium. Ich versichere, dass diese Dissertation nicht in einem früheren Promotionsverfahren eingereicht wurde.

Ort, Datum Unterschrift

# List of hazardous substances

I herewith declare that I did not use any hazardous chemical substances during my Ph.D. work.